UNIVERSITY OF CALIFORNIA,
IRVINE

Vibrationally Sensitive Nonlinear Optical Microscopy with Infrared Light

DISSERTATION

submitted in partial satisfaction of the requirements
for the degree of

DOCTOR OF PHILOSOPHY

in Physics and Astronomy

by

Adam M. Hanninen

Dissertation Committee:
Professor Eric O. Potma, Chair
Professor Enrico Gratton
Associate Professor Franklin Dollar

2018

DEDICATION

This thesis is proudly dedicated with heartfelt fondness to the family and friends who made my UCI grad school experience an absolute joy. Special gratitude goes to my mom and grandma, Linda and Verllien, and Bill, for supporting me to the core and always happy to talk, you are the best. I'm appreciative of my many friends: Alexey, Adam, Ethan, Hannah, Alex S., David, Trenton, Alex F., Alex H., Derek, Kyle, *et alia* for making my time here enjoyable and rememberable. To my friends in the Potma labs: Alba, Brian, Faezeh, Alex F., Bongsu, Ryan, John K., John H., Evan, Alex H., and of course the Prince-Richard, thank you for being excellent friends and reliable lab mates. An especially warm and gracious dedication to Olivia Humphrey, for going above and beyond in so many ways, you are truly special. Finally, to my advisor Eric, thank you for your patience, guidance, expertise, and sincere dedication to your students. You are a role model for us all.

TABLE OF CONTENTS

LIST OF FIGURES

LIST OF TABLES

ACKNOWLEDGMENTS

I would like to acknowledge the funding agencies particularly the NSF, the local optics communities including the OSA/ SPIE student group at UCI, and the professional optics organization OSSC. I'd like to acknowledge Curt Deckert for assisting business development of Trestle Optics, Dima Fishman for help with the 2PA project, Richard Prince, Alex Fast, and John Kennison for lending a hand in lab, and Olivia Humphrey for proof reading this thesis. Finally, I'd like to acknowledge Eric Potma as an outstanding researcher and advisor.

CURRICULUM VITAE

Adam M. Hanninen

EDUCATION

Doctor of Philosophy in Physics **2018**
University of California, Irvine *Irvine, CA*

Masters of Science in Physics **2016**
University of California, Irvine *Irvine, CA*

Bachelor of Science in Physics **2013**
University of Minnesota, Twin Cities *Minneapolis, MN*

RESEARCH EXPERIENCE

Graduate Research Assistant **2013–2018**
University of California, Irvine *Irvine, California*

TEACHING EXPERIENCE

Teaching Assistant **2013–2015**
University of California, Irvine *Irvine, CA*

REFEREED JOURNAL PUBLICATIONS

High Resolution infrared imaging of biological samples with third-order sum frequency generation microscopy **2019**
Biomedical Optics Express

Triple modal coherent nonlinear imaging with vibrational contrast **2018**
Biomedical Optics Express

Hyperspctral imaging with laser scanning sum-frequency generation microscopy **2017**
Biomedical Optics Express

REFEREED CONFERENCE PUBLICATIONS

Vibrational imaging with third-order sum-frequency generation microscopy **Feb 2018**
SPIE Photonics West

Molecular Imaging with Sum-frequency Generation Microscopy **Apr 2015**
Novel techniques in microscopy

ABSTRACT OF THE DISSERTATION

Vibrationally Sensitive Nonlinear Optical Microscopy with Infrared Light

By

Adam M. Hanninen

Doctor of Philosophy in Physics and Astronomy

University of California, Irvine, 2018

Professor Eric O. Potma, Chair

Sum frequency generation microscopy (SFG) is a nonlinear optical technique used to visualize interfaces and noncentrosymmetric structures that lack inversion symmetry. The advantage of SFG, which uses two collinear lasers, over its degenerate counterpart second harmonic generation (SHG), is that it enables chemical contrast through molecular vibrational absorptions in the infrared known as the fingerprint region. IR-active molecular modes are energized into a vibrationally excited state through a direct dipole excitation, and then probed with higher energy photon(s) before parametrically radiating a photon at the sum of the incident frequencies. Incorporating this technique into a multi-modal microscope is an important development as it allows high resolution imaging with spectroscopic information without exogenous labels. Following the development of the SFG microscope came the discovery of vibrationally resonant third-order sum frequency generation (TSFG), a four-wave mixing process that probes resonant contributions of the $\chi^{(3)}$ tensor. This technique, comparable in sensitivity to the coherent anti-Stokes Raman scattering (CARS) modality, was applied to label-free imaging of cells rich in lipid droplet content. This work contributes to the study of high resolution IR-microscopy by merging it with the field of nonlinear optical microscopy.

Chapter 1

Introduction to nonlinear optics

1.1 Development of nonlinear imaging in the mid-infrared

Nonlinear contributions to the constitutive relations set forth by Maxwell in the early 1860's have been known since the theoretical foundation of light-matter interactions. A materials response to an applied electric field is described by its polarization $\mathbf{P}$, which, in the dipolar approximation, quantifies the net dipole moment per unit volume

$$\mathbf{P} = \epsilon_o \left[\chi^{(1)}\mathbf{E} + \chi^{(2)}\mathbf{E}^2 + \chi^{(3)}\mathbf{E}^3 + ...\right] \tag{1.1}$$

where $\mathbf{P}$ is written as a power series expansion of the electric field. In general, the susceptibility $\chi^{(n)}$ is a (n+1) rank tensor, and the $\mathbf{E}$-field and polarization are both vectorial quantities. The lowest order term corresponds to a linear dielectric response and relates to the degree of polarization a material undergoes in response to an applied electric field. Unveiling higher-order terms, however, requires rather strong field strengths. Yet when

the required field strength is achieved, nonlinear frequency conversion begins and exposes a colorful realm of physics. The first application of electromagnetic wave-mixing was used to explain a phenomenon of radio waves in 1933, known as the Luxembourg Effect. Here, an amplitude modulated radio wave imposed its modulation onto another carrier frequency due to temperature induced changes in the reflective properties of the ionosphere. The following decade saw the first frequency doubling and subsequent higher harmonic generation experiments that occurred in high temperature plasmas using coherent microwave frequency sources known as masers, (microwave amplification by stimulated emission of radiation.) Then, in 1961, Franken et al. focused coherent light from a commercially available ruby optical maser onto a sample of crystalline quartz. At focus the electric field reached an intensity of approximately 105 V/cm, and a radiation line appeared with a wavelength at 347.2nm, half the wavelength of the incident light [32]. The result was so surprising that the editor famously misinterpreted the new radiation line as a blemish on the image and removed it from the publication. For the first time frequency doubling had occurred in the optical region of the electromagnetic spectrum, and thus the door to nonlinear optics was opened.

Shortly thereafter, new nonlinear optical effects were discovered at a tremendously rapid rate. These included sum- and difference-frequency generation, third-harmonic and higher harmonic generation, parametric amplification and oscillation, stimulated scattering, the optical Kerr effect, self-phase modulation, and many more. This renaissance in the high field limit drove new applications in the late 60s, including nonlinear spectroscopy, multi-photon absorption, coherent optical transiences, and so forth. Many experimentalists contributed to the burgeoning field of laser research in the 1960s, most notably the Dutch physicist Nicholaas Bloembergen. While a professor at Harvard, Bloembergen developed an effective method of creating a population inversion via pumping a three-level energy system, a prerequisite for stimulated emission. He also expanded the theoretical framework of equation 1.1 by analyzing how photons at high intensity interact with matter. For example, a change in the

refractive index as a function of light intensity. [8] In the early 60's his group published three extensive papers exploring the phenomenology and fundamentals of nonlinear optics. Many original concepts were presented, including the first appearance of quasi-phase matching, a method by which nonlinear conversion efficiencies are enhanced. This enabled technologies that are now ubiquitous, including green laser pointers and high definition blu-ray DVDs. In 1965 he published the first monograph in the field titled Nonlinear Optics, and 26 years later won the 1981 Nobel Prize for his study of atoms using laser spectroscopy. Bloembergen's remarkable research set the stage for nonlinear technologies using mid-infrared light, despite not having actually investigated the regime himself.

By the 1970s applications of nonlinear optics (NLO) started to spur the field of astronomy to search for a method to efficiently detect cosmic MIR photons by photon upconversion. In 1977, Robert Boyd was working at the worlds largest solar telescope, the McMath-Pierce Telescope in Arizona, when he developed a nonlinear up-conversion device that he installed at the focus of the telescope to image IR radiation. He mixed 10μm cosmic radiation with 250mW of a krypton-ion laser, centered at 730nm, onto a proustite crystal (Ag_3AsS_3) to form images of astronomical sources from upconverted light.[10] Though efficient phase-matching conditions limited signal generation, they were able to use a highly sensitive Si detector to record their images. Modern investigations in astronomy are still heavily focused on MIR detection, markedly the upcoming James Webb Space Telescope whose primary study is to spectroscopically observe the youngest of the massive galaxies (z-shift of 5).[94] However, detection schemes today use cryogenically cooled pixel arrays instead of photon up-conversion. While there has been a recent insurgence in photon up-conversion in microscopy, the technique is still stifled by technical challenges, just as it was for Boyd, resulting in low contrast images compared to competing upconverting strategies. Like a hurricane, Boyd went on to make a splash in a wide range of optical sub-fields including: entanglement generation, quantum imaging, turbid media studies, optical solitons, nonlinear optics, and much more. He too authored a textbook titled Nonlinear Optics, in which he describes the physics of

the SFG upconversion process a second-order interaction where two different wavelength photons converge.

Infrared light is remarkable. Besides its longer wavelength, the infrared is fundamentally no different than the visible light we use to observe our surroundings. Infrared radiation is also comforting, it provides the warming glow of a campfire and the blissful joy of a cup of coffee on a cold winters morning. And yet, it wields a peculiar utility that is subtler than its thermal effects. It is in this wavelength regime of the EM-spectrum that molecules vibrate. Here, molecules experience orders of magnitude difference in absorption over a narrow spectral range. These absorption features are unique to individual molecules and characteristic of the chemical composition. The features are, in fact, so unique this region of the MIR is commonly known as the finger-print region, and spans from 3-10um. IR absorption spectra have been used by analytical chemists since the 1930s.[121] During WWII there were major developments in commercial devices as it was the best technique to analyze the production of synthetic rubber. Today, Fourier-transform infrared (FT-IR) spectrometers are commonly used to study linear IR absorptions and have been implemented in a spatial scanning platform for FT-IR microscopy of biological samples including cells, tissue, and whole systems. These devices use globars, incoherent thermal emitters, but when coherent light sources are used MIR spectroscopy can be readily realized in a nonlinear fashion through sum-frequency generation. The field of vibrationally sensitive SFG spectroscopy has been integral to the study of surface chemistry and was pioneered by Y.R. Chen in 1987.[100] SFG uses tunable ultra-fast laser sources to monitor surface dynamics and reactions with sub-picosecond time resolution. The physical origin of the surface nonlinearity arises from two sources, structural discontinuity and field discontinuity at the surface, the latter being more sensitive to liquid/ gaseous interfaces. SFG's main advantage is its sensitivity to chemical vibrations in the fingerprint, while the signal is detectable with highly sensitive photomultipliers which operate in the visible/NIR. Most SFG spectroscopic studies use an excitation geometry shown in fig1.1, which is conducive to efficient phase matching. The

illumination system shown in figure 1.1 has also been implemented in a microscope [19]. Other groups have placed a prism on top of the sample to improve field confinement. [1]

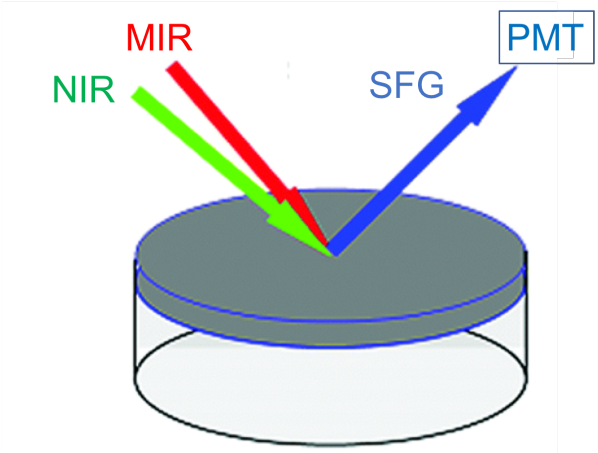

Figure 1.1: Angled excitation geometry, SFG signal detected in reflection. This implementation of a SFG microscope benefits from better phase matching, however it is not compatible with high NA objectives.

In 2011, the Potma lab implemented SFG microscopy in a collinear excitation geometry as shown in figure 1.2, though not in conjunction with beam-scanning mirrors.[90] The difference between figure 1 and 2 may seam minimal, but the former is used exclusively for SFG spectroscopy measurements of interfaces, while the latter is applied in virtually all nonlinear optical microscopes. The reason for the difference is found in the capabilities and limitations of optical components, which are addressed in depth in chapter 2. Let us first take a look at the NLO modalities that SFG joined in the collinear excitation geometry.

1.2 Complimentary imaging techniques

Enabled by fluorescent labels and advances in ultrafast laser technology, [107] [3] the first nonlinear optical microscope using two-photon absorption (2PA) fluorescence was in 1990.[26] The benefits of 2PA, and all NLO techniques for that matter, over linear fluorescence and confocal is the inherent 3D resolution. Intrinsic to the nonlinear process resulting from

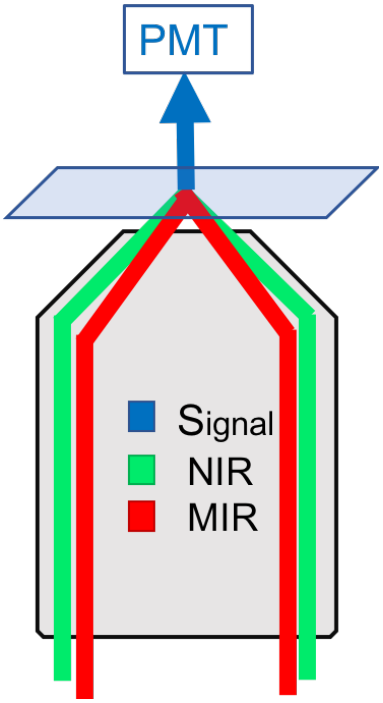

Figure 1.2: Collinear excitation inside the objective lens of a traditional inverted microscope.

tightly focused light is volumetric optical sectioning on the micron scale. Excitation beams, typically in the NIR, and signals produced in the visible scatter much less than their linear fluorescence counterparts that excite in the UV. Chromatic aberration in high NA objectives is also reduced when visible signals are paired with NIR, as opposed to UV. Additionally, NIR excitations avoid the usual photodynamic perturbations and facilitates fluorescence observations of living cells over longer times. By 2003 multi-photon microscopes (MPM) capable of generating images using two- and three-photon fluorescence along with coherent signals from second- and third-harmonic generation were becoming standard microscope tools.[11] A key factor to the utility of a MPM is the use of endogenous structural markers, signifiers inherent to the sample that could generate contrast, in addition to fluorescent labels. However, while these microscopes had excellent resolution of structures within the field of view they lacked molecular information.

To include molecular information requires either probing the IR absorption spectrum as identified above, or through the complimentary Raman spectrum, an inelastic scattering process.

Photon scattering is predominantly elastic, where the scattered photon has the same energy as the incident photon. This is not the case in Raman scattering. Here, an incident photon starts the process by exciting an electron to a virtual state, which then either spontaneously relaxes non-parametrically to a vibrational state, or it is driven there by a tunable laser (Stokes) beam known as a stimulated process. Raman signals are enhanced when the stimulating Stokes beam is tuned to an energy difference corresponding to a real vibrational state, which means that the signal can be used to probe molecular vibrations inside a focal volume. In 2005 Potma *et al.* realized the first *in vivo* video-rate MPM that incorporated homodyne detection of Raman sensitive radiation known as coherent anti-Stokes Raman scattering (CARS) microscopy.[31] Shortly thereafter a second technique reliant on the Raman process for contrast, called Stimulated Raman Scattering (SRS) microscopy, was developed in 2007. Both imaging techniques are coherent, meaning they radiate instantaneously and in the preferred forward direction. Probing vibrational coherences is a robust way to extract chemical information beyond what can be accessed with the electronic transitions probed in fluorescence.

With all these techniques integrated into one microscope, multi-photon fluorescence, coherent harmonic generations, and now coherent Raman scattering, the table was set (pun intended) for intrinsic IR absorptions to be exploited in the multi-modal nonlinear microscope. The body of this thesis describes work that enabled vibrationally sensitive SFG to join the family of NLO modalities incorporated into a beam-scanning multi-modal microscope. SFG, and the newly realized third-order response third-order sum frequency generation (TSFG) were used to image biologically relevant samples including tendon, cornea, and lipid droplets in cells. A detailed review of the tools used in the SFG/TSFG microscope is provided in chapter 2, but to better understand the nature of the SFG and TSFG technique, we first examine the physical models that explain the phenomena.

1.3 Theory of nonlinear light matter interaction

Nonlinear optics is the study of phenomena that occurs when optical properties of a material are modified due to the presence of light. Light is a wave of electromagnetic radiation in the classical interpretation. Optical fields oscillate at frequencies in the 10^3 THz, far too fast for charged nuclei to follow adiabatically. The motion of the electrons in the material, however, are susceptible to the driving fields, and when slightly displaced from equilibrium will introduce an electric dipole moment.

$$\mu(t) = -e * r(t) \tag{1.2}$$

The macroscopic polarization, which is obtained by adding all N electric dipoles per unit volume is

$$P(t) = N * \mu(t) \tag{1.3}$$

The magnitude of the dipole depends on the extent of the displacement, which in the weak field limit is linearly proportional to the electric field, allowing the polarization to be written as

$$P(t) = \epsilon_0 \chi E(t) \tag{1.4}$$

where ϵ_0 is the electric permittivity in vacuum and χ is the linear susceptibility of the material and dictates the properties of all linear optical phenomena. For stronger fields, the electron is farther displaced from its equilibrium position leading to binding potentials that are no longer harmonic as anharmonic effects become more significant. Large electron displacements necessitate nonlinear corrections resulting in a polarization with higher order

terms expressed as a power series expansion of the electric field as in equation 1.2.

$$\begin{aligned} P(t) &= \epsilon_0 \left[\chi^{(1)}E(t) + \chi^{(2)}E^2(t) + \chi^{(3)}E^3(t) + ...\right] \\ &= P^{(1)}(t) + P^{(2)}(t) + P^{(3)}(t) + ... \end{aligned} \tag{1.5}$$

The generation of SFG signals arise from the second term $\mathbf{P}^{(2)}(t) = \epsilon_0\chi^{(2)}\mathbf{E}^2(t)$ and involves two distinct optical fields such that the input field can be written as

$$\mathbf{E}(t) = \mathbf{E}_1 e^{i\omega_1 t} + \mathbf{E}_2 e^{i\omega_2 t} \tag{1.6}$$

where $\mathbf{E}_1,\ \mathbf{E}_2$ and $\omega_1,\ \omega_2$ are the amplitude and frequencies of the two optical fields respectively. Evaluating the magnitude of the polarization component at the sum frequency we find

$$\mathbf{P}(\omega_1 + \omega_2) = 2\epsilon_0\chi^{(2)}\mathbf{E}_1\mathbf{E}_2 \tag{1.7}$$

To see how the polarization affects nonlinear signal generation in a tight focus, we begin

with Maxwells equations with no free charges or free currents.

$$\nabla \times \mathbf{E} = -\frac{\partial \mathbf{B}}{\partial t} \tag{1.8}$$

$$\nabla \times \mathbf{H} = \frac{\partial \mathbf{D}}{\partial t} \tag{1.9}$$

$$\nabla \cdot \mathbf{B} = 0 \tag{1.10}$$

$$\nabla \cdot \mathbf{D} = 0 \tag{1.11}$$

Where $\mathbf{D}$ is the electric displacement field. In a dielectric material, the presence of an electric field causes bound charges to slightly separate, inducing a local electric dipole moment. $\mathbf{D}$ is defined by the constitutive equation for electric fields

$$\mathbf{D} = \epsilon_0 \mathbf{E} + \mathbf{P} \tag{1.12}$$

And has higher order terms when equation 1.5 is inserted into 1.12. To solve the wave equation of motion we proceed in the usual manner. Take the curl of the $\nabla \times \mathbf{E}$ in equation 1.8, interchange the order of the space and time derivatives on the right-hand side of the resulting equation, and replace $\nabla \times \mathbf{B}$ with $(1/c)(\partial \mathbf{D}/\partial t)$ to obtain the equation

$$\nabla \times \nabla \times \mathbf{E} + \frac{1}{c^2}\frac{\partial^2}{\partial t^2}\mathbf{D} = 0 \tag{1.13}$$

Substituting $\mathbf{D}$ from equation 1.12, we arrive at the most general form of the wave equation for nonlinear optics.

$$\nabla \times \nabla \times \mathbf{E} + \frac{1}{c^2}\frac{\partial^2}{\partial t^2}\mathbf{E} = -\mu_0 \frac{\partial^2 \mathbf{P}}{\partial t^2} \tag{1.14}$$

By enacting the vector identity for the curl of a curl ($\nabla \times \nabla \times \mathbf{E} = \nabla(\nabla \cdot \mathbf{E}) - \nabla^2 \mathbf{E}$ where ∇^2 is the vector Laplacian operator, and asserting the assumption that the divergence of an

electric field is negligible, equation 1.12 takes the form

$$\nabla^2\mathbf{E} - \frac{n^2}{c^2}\frac{\partial^2}{\partial t^2}\mathbf{E} = \frac{1}{\epsilon_0 c^2}\frac{\partial^2}{\partial t^2}\mathbf{P} \tag{1.15}$$

This equation has the form of an inhomogeneous driven wave equation and is the starting point for most models concerned with the spatial and temporal evolution of nonlinear signals. The nonlinear source term on the right hand side of the equation considers polarization densities in the vicinity of the focal volume where field strengths are high. Outside the focal volume, the nonlinear polarization is negligible. The reason why polarization plays the key role in nonlinear optical phenomena as the source of new components is because a time-varying polarization means accelerated charges, and according to Larmor's theorem for electromagnetism accelerated charges generate electromagnetic radiation. To see how this plays out on the atomic level, let us take a look at the Lorentz model of an atom.

The Lorentz model treats the atom as a harmonic oscillator just like two masses on a spring, and is known to provide a good description of optical properties. The model can be extended by allowing nonlinearities in the restoring force exerted on the electron. The details of the analysis differ depending upon whether or not the medium possesses inversion symmetry. First, we treat the case of a noncentrosymmetric medium which gives rise to a second-order optical nonlinearity, followed by a medium with a center of inversion symmetry where third-order nonlinear susceptibility is the lowest order non-vanishing nonlinearity.

For the case of noncentrosymmetric media, the equation of motion of the electron in the presence of a one-dimensional electric field takes the form

$$\ddot{\mathbf{x}} + 2\gamma\dot{\mathbf{x}} + \omega_0^2\mathbf{x} + a\mathbf{x}^2 = -e\mathbf{E}(t)/m \tag{1.16}$$

Which includes a damping force ($-2m\gamma x$) and the restoring force ($-m\omega_0^2 x - max^2$) where we retained the linear and quadratic terms in the Taylor series expansion of the restoring force in the electron displacement $\mathbf{x}$ and a is a parameter characterizing the strength of the nonlinearity. The nature of the restoring force is better understood by noting that it corresponds to a potential energy function of the form

$$U = -\int \mathbf{F}_{restoring}(x)dx = \frac{1}{2}m\omega_0^2 x^2 + \frac{1}{3}max^3 \tag{1.17}$$

Here, the first term corresponds to a harmonic potential and the second term corresponds to an anharmonic correction that more closely aligns the theoretical model with the physical situation of electrons in the real material shown in figure 1.3. While the parabolic harmonic potential is a good description at smaller displacements, it deviates from the physical system at larger displacements in the case of strong applied fields. This is corrected for with the odd-powered anharmonic term which is non-vanishing only for asymmetric systems and depends quadratically on the applied field. In fact, governed by point-symmetry requirements of the medium, many geometries are restricted. In particular, the polarization vector vanishes in a medium which is isotropic, characterized by a center of inversion. Systems with a non-vanishing second-order response include: solid crystalline structures lacking a center of symmetry, chiral molecules and structures, and interfaces between materials with disparate index of refractions. For the crystals, of the 32 point group classes, 21 are non-centrosymmetric. Other peculiar qualities of these asymmetric crystal classes include: piezoelectric, pyroelectric, and ferroelectric properties. The presence of these effects is dependent upon the crystal class and not upon the material, although the degree of the effect is material specific. Typical $\chi^{(2)}$ values for crystals are on the order of 10^{-8} cm/statvolt.

For the case of a centrosymmetric medium, where the electron displacement potential contains a center point of symmetry, the restoring force is instead ($-m\omega_0^2 x - mbx^3$) where b is the parameter characterizing the strength of the nonlinearity. Following equation 1.17 we

find

$$U = -\int \mathbf{F}(x)_{restoring} dx = \frac{1}{2} m\omega_0^2 x^2 - \frac{1}{4} mbx^4 \tag{1.18}$$

which is symmetric under the inversion operation $x \rightarrow (-x)$ since the potentials are both even-powers as shown in figure 1.3. The lowest order nonlinear response resulting from equation 1.18 is the third-order response characterized by $\chi^{(3)}$. Examples of such materials are liquids, gases, and amorphous solids such as glass. Though the restrictions on non-centrosymmetric materials are quite strict, everything has a non-vanishing third-order nonlinear response, including, it is theorized, the vacuum of space-time. Typical values of $\chi^{(3)}$ are on the order of 10^{-14} cm^2/statvolt^2.

Now that we have seen the origin of nonlinear signals, it is important to understand how this process fits in within a microscope system. The input fields are brought to a tight focus and the signal radiation is then detected in the far-field. To describe the nonlinear signal at each point $\mathbf{R}$ in the far field, it is helpful to describe each point $\mathbf{r}$ in the excitation volume as an oscillating dipole source. In the far field, the dipole field is found to be a radiating field. The problem now converges to finding the far field solution of the electric field that results from a single radiating dipole source at $\mathbf{r}$. This can be written as

$$\mathbf{E}_d(\mathbf{R};\mathbf{r}) = \frac{e^{ik|\mathbf{R}-\mathbf{r}|}}{4\pi|\mathbf{R}-\mathbf{r}|^3} \left[((\mathbf{R}-\mathbf{r}) \times \mathbf{P}^{(n)}(\mathbf{r})\right] \times (\mathbf{R}-\mathbf{r}) \tag{1.19}$$

Where $\mathbf{P}^n$ corresponds to the nth order polarization of the dipole oscillator. Note that in the far field the electric field of a single emitter approaches a spherical wave. To find $\mathbf{E}(r)$ at the detector, we have to coherently add the dipole fields emanating from all points $\mathbf{r}$. Expressed as an integral over the region enclosed in the focal volume this is written as

$$\mathbf{E}(\mathbf{R}) = \int \mathbf{E}_d(\mathbf{R};\mathbf{r}) d^3\mathbf{r} \tag{1.20}$$

When the signal is detected in the homodyne manner (frequency different than the input frequencies) as is the case in all of the signals analyzed in this work, the signal intensity measured by the detector is written as, in spherical coordinates,

$$I \approx \int_{\theta_1}^{\theta_2} \int_{\phi_1}^{\phi_2} \mathbf{E}^2(\mathbf{R}) R^2 \sin\theta d\phi d\theta \tag{1.21}$$

The coherent addition in point $\mathbf{R}$ of the contributions of all radiative dipoles produces interferences. Far-field points that display constructive interference of the combined radiative contributions are said to represent directions in which the signal is phase matched. For example, for a process like CARS, radiating dipoles aligned in the axial direction constructively interfere in the forward-direction, along with the collinearly aligned excitation beams. Conversely, signals propagating laterally or backward, in the epi direction, destructively interfere. Thus, the strongest signals are found in the forward direction. Epi-detection is still possible to measure however, due to scattering effects from the forward generated signal.

In general for SFG, disregarding phase matching conditions,

$$I_s \propto |\chi^{(2)}|^2 I_1 I_2 \tag{1.22}$$

however, this expression does not account for polarization dependence. Additional consideration is needed to understand the polarization of the incident and radiative fields and the molecular response of the material. We define the surface based coordinate system of the lab frame in cartisian coordinates (x, y, z) and set the z-axis along the direction of the beam propogation, defined by the Poynting vector. The prescribed polarization is assigned as $\chi_{i,j,k}$ where the subscripts correspond to the fields by frequency in decending order i.e. i,j,k correspond to the signal, pump, and idler beams respectively. $\chi^{(2)}_{i,j,k}$ is a third-rank

tensor with a total of 27 macroscopic susceptibility elements, however, many of these elements are zero and therefore no signal is generated with these polarization settings. For an azimuthally isotropic interface ($C_{\infty\nu}$ symmetry) there are seven nonzero achiral tensor elements $\chi^{(2)}_{yyy}, \chi^{(2)}_{yzz} = \chi^{(2)}_{yxx}, \chi^{(2)}_{zzy} = \chi^{(2)}_{xxy}, \chi^{(2)}_{zyz} = \chi^{(2)}_{xyx}$. The dominant terms for samples aligned in the x-y plane are $\chi^{(2)}_{yyy}, \chi^{(2)}_{yxx}, \chi^{(2)}_{xyx}, \chi^{(2)}_{xxy}$. What we directly obtain from an SFG spectrum is the effective macroscopic susceptibility, and to elucidate microscopic information we need to relate this value to the molecular hyperpolarizability $\beta^{(2)}_{i',j',k'}$.

$$\chi^{(2)}_{i,j,k} = N \sum_{i',j',k'} \langle \mathbf{R}_{i,i'} \mathbf{R}_{j,j'} \mathbf{R}_{k,k'} \rangle \beta^{(2)}_{i',j',k'} \tag{1.23}$$

where N is the number density of the moiety under investigation, $\mathbf{R}_{\lambda\lambda'}$ is an element of the rotational transformation matrix from the molecular coordination λ'(a,b,c) to the labratory coordinate λ(x,y,z), and $\langle\rangle$ denotes the ensemble average over all possible molecular orientations. In vibrationally sensitive SFG, the IR frequency is near resonance to molecular vibrational transitions, and the second-order molecular polarizability is

$$\beta^{(2)}_{i,j,k} = \beta^{(2)}_{NR} + \beta^{(2)}_{R} = \beta^{(2)}_{NR} + \sum_{q} \frac{\beta^{q}_{i,j,k}}{\omega_{IR} - \omega_q + i\Gamma_q} \tag{1.24}$$

where the first term $\beta^{(2)}_{NR}$ represents non-resonant contributions; β^q, and ω_q, and Γ_q are the sum frequency strength factor tensor, vibrational mode frequency, and damping constant of the qth molecular vibrational mode, respectively. In general, β_{NR} should be small and real when the substrate is not in resonance. In the theory of SFG-VS with a single resonance with IR frequencies, the tensor elements of β^q are related to the IR ($\mu_{k'}$) and Raman ($\alpha^{(1)}_{i',j'}$)

properties of the vibrational mode

$$\beta^{q}_{i',j',k'} = \frac{-1}{2\epsilon_0 \omega_q} \frac{\partial \alpha^{(1)}_{i',j'}}{\partial Q_q} \frac{\partial \mu_{k'}}{\partial Q_q} \tag{1.25}$$

are proportional to the partial derivatives of the Raman polarizability tensor and the IR transition dipole moment of the qth vibrational mode; and Q_q is the normal coordinate of the same mode. The squares of $\mu'_{k'}$ and $\alpha'_{i',j'}$ are directly proportional to the intensities of the Raman and IR transition of the qth vibrational mode. Therefore, any non-zero sum frequency vibrational mode has to be both IR and Raman active. This is the transition selection rule for SFG-VS.

Chapter 2

Components of a SFG Microscope

2.1 Light source in the mid-infrared

The experimental setup is similar to a standard CRS microscope, with additional complexities necessitated by the mid-infrared laser source. Optical components designed for the MIR are sparse and often expensive. Many of the optical components used required custom orders, most significantly the scan lens and the tube lens which will be discussed in greater detail presently. Additionally, we used custom dichroics, a one-of-a-kind tunable frequency conversion cavity designed for MIR generation, and a single photon counting detection scheme. Limitations of off-the-shelf component availability means the microscope used for this research is certainly unique, sporting quirks and features that will be addressed in this chapter. Special attention will be given to the custom components, but first we must consider the laser. If an objective lens is the heart of a microscope, then the laser is surely the legs; it is the powerhouse that carries the weight of the experiment. A maintained and fine-tuned laser can be of great utility and a source of steadfast reliability. The achievement of maximum output has traditionally been nothing short of a dance between the laser and

its operator; it requires experience and an acute sensitivity to know which mirror to adjust, and when to do so. Thanks to developments in the telecom industry, modern fiber laser sources are often turn-key solutions. Conversely, an ill-managed laser can wreak havoc and destroy any prospect of a productive day in lab and needlessly delaying results. This became apparent when the SFG optics table I adopted included a 1064nm Nd:YAG laser which was 10 years old. The laser was wrought with inadequacies. The beam profile sported three stacked lobes characteristic of a (0,2) Hermite-Gaussian beam, far from the ideal Gaussian profile. The power fluctuated so greatly that it often drifted entirely out of phase matching after a matter of minutes. If lasers are supposed to be the legs, this one didn't just have two left feet, but was dancing on its last. Thankfully, this laser was replaced with an Yb:doped fiber laser supplied by NKT Photonics and has been a trustworthy piece of equipment. The laser oscillator generates 7ps pulses centered at 1030nm with a 76 MHz repetition rate and a maximum output at 10W totaling approximately 7nJ/pulse and 2kW of peak power. The pulse duration is ideal for spectroscopically resolved nonlinearities. In short, the benefits of integrating the new fiber laser on the table were immediately palpable. The laser output was used to seed an optical parametric oscillator (OPO), which is a light source similar to a laser, but is based on optical gain from parametric amplification in a nonlinear crystal rather than from stimulated emission. An OPO converts an input laser called the pump with frequency w_p into two output waves of lower frequencies called the signal (ω_s) and the idler (ω_i) by means of a second-order nonlinear optical interaction such that $\omega_p = \omega_s + \omega_i$. For historical reasons the output wave with lower frequency is labeled the idler. The main advantage of the OPO is the wide tunability of the down-converted signal and idler photons. Most lasers are direct bandgap diode lasers and have a narrow gain bandwidth, therefore limiting tunability to around 100nm. However, in our OPO we can achieve wavelength tunability between 1400 - 1800nm for the signal beam and 2400 - 4100nm for the idler beam. Much like a laser, for an OPO to have gain in the signal or idler beam requires a minimum intensity threshold be exceeded. For this reason, the signal beam in the OPO is synchronously

pumped in a singly resonant linear cavity. When tuned properly, the nonlinear conversion can take place at pump intensities as low as 3.3W. As stated above, the nonlinear crystal in the cavity undergoes three-wave mixing, therefore the crystal must have a non-vanishing $\chi^{(2)}$ nonlinearity. For efficient generation the crystal should be optically transparent at all three wavelengths (pump, signal, and idler), and support phase-matching conditions. The parametric amplification process must be phase-matched to ensure an appreciable output of converted light. This can be accomplished by changing the temperature or angular orientation of the crystal for critical phase matching, or the poling period for quasi-phase matching in a periodically poled crystal. Our OPO uses the latter, a fan-poled periodically poled lithium niobate (PPLN) crystal which has poles shaped in a concentric "V" formation. This design satisfies the phase-matching condition of different output wavelengths with a simple lateral translation of the crystal. The PPLN crystal is doped with five percent MgO which increases the damage threshold and improves longevity. Unfortunately, the transparency of our PPLN is truncated around 4.1μm, thereby limiting the spectral range to wavenumbers greater than 2400cm^{-1}.

Lithium niobate is a ferroelectric crystal, which means each unit cell in the crystal has a small electric dipole moment. The orientation of the electric dipole in a unit cell is dependent on the positions of the niobium and lithium ions in that unit cell. The unit cell's crystal structure can be inverted with an intense electric field (22kV/mm) and as a result flip the orientation of the electric dipole, after which the inverted sections of the crystal are permanently imprinted into the crystal structure; typical poling periods are a few microns in size. While all sorts of nonlinearities are generated in the PPLN, only the interaction that satisfies the quasi-phase matching condition will generate an appreciable output i.e. the signal and idler beams. The predominant other nonlinearities generated are the SHG of the three beams and the SFG of $\omega_{signal} + \omega_{pump}$ and $\omega_{idler} + \omega_{pump}$. These 5 colors are on the order of a few mW and need to be filtered out. The only nonlinearity of these five with any utility is the $\omega_{idler} + \omega_{pump}$ SFG because it contains information on the idler wavelength

which is revealed with a spectrometer. This weak beam could in principle also be used in the microscope for stimulated and heterodyne SFG experiments, though such experiments are beyond the scope of this thesis. While OPOs have wide tunability and high conversion efficiency, they tend to occupy a large footprint 1.5m^2 and have a complex cavity geometry which hinders their overall usability.

2.2 Optical components of the microscope

After the three beams leave the OPO they are separated with dichroics for individual beam conditioning. Optical suppliers do not retail dichroic mirrors for MIR light, so we ordered custom long-pass dichroics with > 99 % reflectivity at 1030nm and < 1 percent reflection at 3-4μm. Dichroics consist of thin layers of evaporated metal-oxide or other semiconductor material vapors deposited onto a flat glass substrate. The thin layers cause a wavelength dependent impedance phase matching, i.e. interference, which can result in an efficient reflection or transmission depending on the design. Highly efficient dichroics designed for the MIR require more layers than their visible counterpart due to the longer wavelength, which adds cost. Because glass is not transparent in the MIR we selected to use a CaF_2 substrate, though ZnSe would have worked fine as well. All three beams have similar beam conditioning optics. First is a loosely focusing lens (f=100mm) followed by a pin-hole spatial filter to eliminate the outer portion of the chief rays, totaling approximately a 10 % power reduction. This cleans up the beam and ensures a Gaussian beam profile. The diverging beam is re-collimated with a short focal length lens (f=50mm), forming a Keplerian telescope, reducing the beam diameter from 3.0 to 1.5mm. Next is a band-pass filter followed by a time-delay stage. For power control we used a half-wave plate followed by a polarizer; the residual pump beam and the signal beam used Glan-Taylor polarizers while the MIR idler used a wire grid polarizer. A second half-wave plate is then used to rotate the linearly polarized

light in order to perform polarization dependent imaging. The beams are then recombined with another long-pass dichroic and sent to the Olympus Fluoview 300 galvanometric scan head.

Galvonametric mirrors (galvos) are used to raster scan the laser over the microscope's field of view. Galvos consist of a pair of motorized mirrors that raster scan over the x-y plane. The aluminum coated mirrors supported high reflectivity for the laser beams including the MIR idler beam. These are versatile scanners with adjustable parameters such as scan speed, scan pattern, and dwell time. This is useful for custom systems like the SFG microscope. When programming your own scanning system I recommend a line-scan with a 20 % voltage reset time. While it will slow down imaging, abrupt voltage changes will degrade the motor and introduce hysteresis over time. Typical scan speeds are 1Hz for 512 x 512 pixel resolution. This can be sped up to video rate speeds of 30fps with a resonant scanner which operates at a fixed frequency, but are better suited for commercial applications as they are not programmable and adjustable. Resonant scanners therefore also reduce pixel dwell time which is not desirable for very weak signals.

Beam scanning is preferred because it is much faster than its predecessor, sample stage scanning. In stage scanning the beams are fixed in place, centered on-axis with the objective lens, and the position of the sample is controlled with a motorized stage. The cumbersome stage moves relatively slow with typical acquisition times of 1 minute per 512 x 512 resolution image. These speeds are incompatible with NLO microscopy and therefore beam scanning is preferred. This is not without difficulties. When the beams are fixed at center they are perfectly aligned on-axis with the objective lens. However, as they are scanned the beam path deviates from on-axis and leads to beam clipping at the objective. To remedy the problem of the walking beam requires the use of an optical relay that maps the surface of the second galvo to the back aperture of the objective lens. These relay systems can consist of a pair of refractive lenses or reflective off-axis parabolic mirrors (OAPM), however,

OAPMs themselves have poor performance off-axis and are incompatible with standard NLO microscopes. Therefore, refractive lenses are the preferred choice. With the relay system in place, over the defined field- of-view, photons arrive centered on the objective's back aperture and propagate through the objective lens at different angles yet at a constant illumination brightness. To this end it is necessary to over-fill the back aperture by about 10 percent in order to ensure illumination uniformity. The development of these relay lenses is what enabled beam scanning SFG microscopy and was a major accomplishment of my research. The details and design specifications will be reviewed in detail in section 2.4.

The reflective objective is a Schwarzschild-Cassegrain which has a small negative spherical primary followed by a large positive spherical secondary mirror. If the mirrors are concentric with the stop located at their common center of curvature, the system can be exactly corrected for third-order spherical, coma, and astigmatism aberrations on axis. Considering the low number of reflective surfaces used - two - this is pretty good performance. The design has been implemented to achieve numerical apertures as large as 0.8, though at the sacrifice of longer working distances. The primary advantage of a reflective objective is achromaticity as mirrors are inherently achromatic in their performance regardless of wavelength. This is ideal for broadband focusing, specifically when using MIR light in combination with visible/near-infrared. However, reflective objectives in their current implementation are overall lower performance than refractive designs, and for this reason are seldom used except in broadband applications. The first problem is that they require large magnifications to obtain high numerical apertures, drastically limiting field of view. It is not unheard of for refractive objectives to have an NA of 0.7 in air with a magnification of 20x. Our objective (Beck 5007) has a NA of 0.65 and a 72x magnification, limiting the FOV to about $(80\mu\text{m})^2$. Additionally, while the design is laterally diffraction limited on-axis, performance quickly degrades towards the peripherals. The edges of the FOV suffer from deleterious aberrations causing lower contrast and poor signal generation, though this could be corrected with aspherical surfaces. Finally, the first mirror obscures on-axis incident light

preventing these photons from coming to focus. This causes a quasi-Bessel beam profile with a null center– the result of which is an elongated focal volume shaped like a cigar or a hot-dog. On-axis, the axial resolution (10-15μm) is more than an order of magnitude worse than lateral (0.5μm). Poor confinement is severely deleterious to the generation of nonlinear optical responses in the sample. It not only limits the axial resolution, it reduces the efficiency of NLO signal generation because of the loosely confined fields.

It is my belief that by deviating from the traditional inverted/ up-right microscope geometry, where illumination beams focus in a straight line on-axis, reflective objectives have a future using a folded geometry. The advent of folded reflective surfaces used for telescopes in the astronomy community is enabled by developments in manufacturing of non-rotationally symmetric free-form surfaces and the associated metrology stitching techniques required to evaluate their performance.[94] A free-form design has potential to simplify optical designs for ultra-broadband applications using light from the UV to far-IR, for example electronically enhanced NLO microscopy with IR vibrational information. This would also be useful for linear MIR techniques which rely on computational microscopy techniques such as ptychography for high resolution and large field of view. The folded free-form design would however be limited to operation in air, and therefore a max NA of 1.0. A potential work around to boost the NA would be to incorporate a refractive element right before focus to form a hybrid Schmidt- Cassegrain. This will allow for solid or liquid immersion media to be used, but will sacrifice true achromaticity in the process.

Many of the problems associated with reflective objectives are mitigated when a lens based refractive design is imposed. High performance refractive objectives can have a dozen or more components, with some designs for the UV having as many as 30. These lenses can deliver superior optical performance over a large FOV, and with appropriate engineering include apochromaticity, a higher order of color correction. Other benefits include low distortion ($<$ 1 percent over the FOV), large NA with minimal magnification, and compatibility with

immersion liquids. Unfortunately, because the optical component market is dominated by the visible/ NIR market, there are no commercially available objective lenses designed for use in the MIR. The existing objectives are all made with glass which has strong absorptions beyond 2.5 μm. There are approximately 200 variants of glass, amorphous SiO_2 with differing amounts of dopants, none of which are compatible with the MIR. Therefore, to use visible and MIR light in a refractive objective requires thinking outside the box. While technically possible, the challenge remains in front of the optics community to develop such a lens. I hypothesize that future technology will rely on advancements in chalcogenide glasses to extend transmission into the visible beyond As_2S_3 which transmits to 620nm and appears red. Chalcogenides seem ideal for their broad transmission range and low dispersion. In addition, they sport a large index of refraction, greater than 2.3, and can achieve strong ray bending with minimal curvatures, thereby reduced aberrations. The high index of chalcogenides may play a pivotal roll in future applications demanding thin optics including AR/VR headsets and wearable optics.

As stated above, the objective lens focuses the excitation beams onto the sample. In the sample plane sits the object being imaged, a thinly sliced material no greater than 100 μm thick, ideally partially transparent and with low scattering. The sample is sandwiched between two 1.5 microscope cover slips with thickness of 170μm. Though the glass cover slides exhibit poor transmission of MIR light, experimentally we find that because its thickness is limited it is possible to pass enough light through the glass to induce nonlinearities in the sample. Aside from absorption effects, the cover slip has to be thin because the working distance of our objective is about 0.8mm; typical microscope slides are 1.0mm. In the sample, the excitation beams come to focus and the coherently generated upconverted signal photon radiates in an axially symmetric radiation profile. The v/NIR signal photons, regardless of the conversion process - SFG, CARS, SHG, or TSFG - needs to propagate through the remainder of the sample without scattering or absorption and then collected by the 1.4 NA oil-immersion condenser objective for detection. The signal photons are then separated with

a 580nm long-pass dichroic, and the SFG and CARS signals are transmitted and directed to the red-sensitive photomultiplier tube (PMT), while SHG and TSFG are reflected to the blue-sensitive PMT.

2.3 Detection and signal processing

Both detection channels have a similar setup, including a short-pass filter to reject residual 1030nm photons and a band pass filter to choose which nonlinear process will be detected. The signal is then passed through a Glan-Taylor polarizer cube, known as the analyzer for polarization resolved studies, and focused with a lens onto the active region of the PMT sensor. The entirety of the signal path is enclosed with black tubes to mitigate stray light contributing noise to the detection. An additional sheet of black cloth is draped over the detection equipment for additional shielding. The PMTs (Hamamatsu 7422-40 and 7422-50) are suitable detectors with high sensitivity and equipped with overflow circuitry to turn off in case of signal overflow (which is indicative of sample burning.) These PMTs operate in an avalanche mode, which through multiple P-N layers create a cascade of electrons resulting in an appreciable current from a single photon detection. Overall, the quantum efficiency, that is the likeliness an incident photon will result in an electron cascade, is specified at 12 percent for the red- sensitive and 40 percent for the blue-sensitive PMT. The detectors output an analog current, which needs to be conditioned for proper registration by the data acquisition (DAQ) card in the Fluoview system. This is a bit of a paradigm shift, for up until this point everything has been optics, but once the photon is detected it becomes a game of electronics. The electrical signal has its own rules for amplification and schemes for noise rejection which are not trivial, and are therefore discussed next.

2.3.1 Single photon counting circuit

An important consideration in an optics lab is what happens to the optical signal after is has been detected. As experimentalists it is imperative to maximize the SNR by increasing signal and likewise minimizing noise. A good PMT has high sensitivity, meaning high quantum efficiency and low noise. Unfortunately, electrical current is not only outputted when a photon is detected, but also by thermal excitations in the sensor. This is signal noise and a robust method of removing it, besides cryogenic cooling which is very expensive, is with a single photon counting (SPC) circuit. Implemented correctly, single photon counting can increase the signal to noise ratio (SNR) of the images by 15 %.

A SPC circuit has many processes in conditioning the electronic signal before it is ready to be sent to the computer. First in line is a transimpedance pre-amplifier (Thorlabs TIA60) used to convert the current output from the PMT to a voltage and then to amplify it. This is accomplished by running the current over a resistor and then through an inverting op-amp, resulting in a negative voltage. Regrettably both the real signal and thermal noise are indistinguishable and are amplified together. Yet, because the number of detected photons is low it is possible to isolate the signal from the noise by assigning a voltage-threshold and assigning a count on the rising edge each time the threshold is exceeded, and ignoring voltages below the threshold. The electrical device with this functionality is a discriminator as it discriminates high voltage signals, presumably generated from a detected photon, from low voltage signals characteristic of thermally produced signals. Each time it counts a photon the discriminator outputs a digital TTL pulse, +5V for 5ns, thereby assigning a discreet valued output based on the number of rising edges which exceed the voltage threshold. Occasionally there is the possibility of an electron avalanche in the PMT occurring from extreme noise build-ups, but with proper assignment of the voltage threshold it is possible to maximize signal while minimizing these noise effects as shown in figure 3.6a.

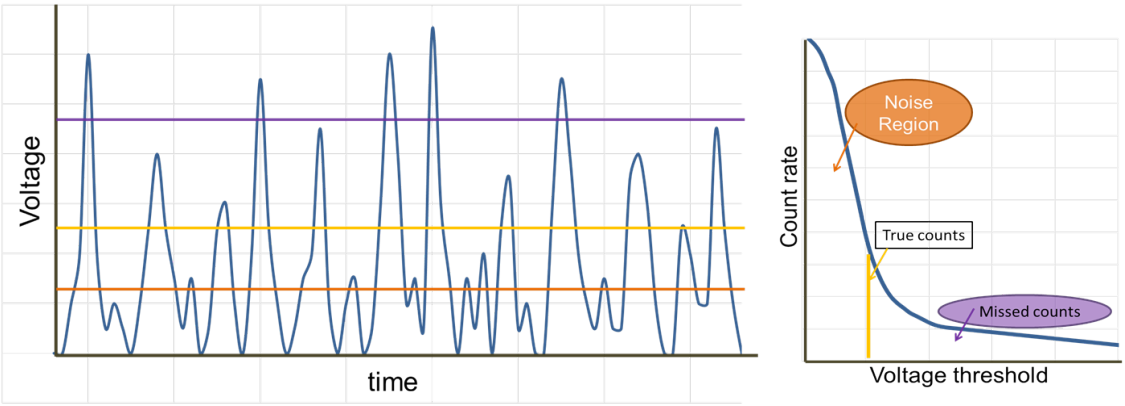

Figure 2.1: Diagram of single photon detection. When a signal exceeds a certain threshold a "count" value is given. In this case, orange shows a threshold too low which will have many counts, most of which are noise. Purple shows a threshold set too high, which misses most of the signal. Yellow is the ideal balance between detecting signals and rejecting noise.

The TTL pulses from the discriminator are short, only 5ns, meaning in the frequency domain the signal carries frequency components beyond 20MHz. This would be fine if the data acquisition (DAQ) board paired with the computer had a similar bandwidth, however the old Fluoview 300 DAQ bandwidth is from DC - 5MHz. Therefore when a TTL is sent directly to the computer the signal is not optimally registered because of the bandwidth mismatch. This task is the crux of the SPC circuit, to transfer these TTL pulses into an analog signal between 0 to +3V with bandwidth from DC - 5MHz, and an impedance of 75ohm. For starters, the circuit input signal is digital TTL pulses and the output needs to be analog, therefore we require a digital to analog (DAC) integrated component (IC). Additionally, we require an IC capable of counting the number of TTL pulses it receives, known as a counter. The counter outputs an 8-bit binary signal along its output leads corresponding to the number of counts it received during a pixel dwell time. However, the counter immediately updates the output every time a pulse is received, and as we want to accrue the total number of received pulses at a given pixel before sending the value to the DAC, a d-flip-flop is used as a register to hold the value until the pixel dwell time is complete. Without the flip flop the DAC would be continuously updating its output, whereas with the flip flop the value is accumulated and given to the DAC once all the counts from that pixel have been collected.

This is important in terms of signal bandwidth which will be addressed later on. At the end of a pixel acquisition, the counter is reset and is ready for the next pixel. The reset function is achieved on the rising edge of a TTL or square wave sent from a wave function generator. The same clock pulse is also used to inform the flip flop that it is time to send the value stored on the input pins along to the output pins. The flip flop output then goes to the DAC input.

The selected DAC (AD745) is known for its high speed and ultra-low noise. It has a chip select and write mode options which controls when the DAC is enabled. This application demands that the DAC should always be running in the write mode, so for this reason the WR and CS pins are held low by being tied to ground. We want to maximize the bandwidth of the DAC output to get the best signal, which means having it output as long as possible in the time domain. Recall that a 1us dwell time corresponds to 1MHz frequency contributions, so we are already pushing the boundary of the 5MHz bandwidth limit. The DAC requires the use of a highly stable voltage reference in order to minimize noise, and for this purpose we use an IC designed to output at -10V. Finally, an inverting op-amp is placed at the end to tailor the signal to the final signal settings to communicate with the Fluoview 300 system. To generate a positive output voltage the simplest solution is to use a negative voltage as the voltage reference, so when it is inverted it will be positive again. The alternative solution is to use two inverting op-amps in series. I also chose the highest recommended Vref and the lowest bit DAC available in order to minimize gain requirements. The more gain the lower the bandwidth that gets amplified and we want to maximize bandwidth.

Here, we learned that the SPC circuit converts TTL pulses to an analog signal proportional to the total number of pulses detected at a given pixel and outputs between 0 and +3V. This concept is relatively straightforward and uses 2 digital ICs (counter and flip flop) and 2 analog ICs (DAC and op-amp). There are, however, many nuanced considerations when designing a mixed signal circuit board. First of all, mixed signal boards require different

grounds. A digital ground (DGND) and all the digital ICs must be separated from the analog ground (AGND), because digital TTL pulses are massively demanding on the ground plane and result in transients that disrupt both the grounding and all voltages held relative to it. This is highly problematic with precision low-noise analog ICs and therefore isolation precautions must be implemented. The first line of defense here is to decouple the bypass capacitors (0.1μF). High frequencies view these as wires, therefore when tied to ground the high frequencies are kept out of the ICs. The second line of defense is ferrite beads on the power supply traces, used to dampen high frequencies by converting their energy to heat. Both these implementations are insignificant if the ground planes are not physically and electrically separated on the PCB. This means including a trench to provide isolation between the copper ground pours between DGND and AGND, and the inclusion of the ferrite bead between the IC power supplies (Vanal and Vdig). There is one spot where the grounds are connected and that is on the DAC. This is known as the star-formation and is the recommended way of integrating mixed signals on a single printed circuit board. Finally, two varistors were used, one on the +15V supply and another for the output. Varistors limit the voltage allowed to travel down a path. While the varistor for the power supply is desirable in case improper grounding prevents excessive voltages, the +4V varistor at the output is imperative to protect the sensitive DAQ card in the Fluoview from damaging high voltages.

The SPC circuit is an effective way to manipulate the electronic signal so that it can be effectively integrated with the DAQ card. However, if the DAQ did not have a bandwidth mismatch the circuit could have been avoided all together. Additionally, an alternative method is to use an arbitrary waveform generator that outputs a longer wave every time it is triggered by an incoming TTL pulse. This is a simpler solution, and the one I found preferential for its ease of use. Here, a longer pulse is outputted from the waveform generator to the Fluoview DAQ instead of the 5ns TTL pulse. Experimentally, a 10MHz square wave at +5V with a 93 % duty cycle was found to have ideal parameters, though in lower signal

cases such as the TSFG modality the frequency can be lowered to 7-8MHz. Though this will inhibit the detection of signals from future pulses, we are well within the single photon limit with a single signal photon detected on the order of every tenth repetition of the laser, so this is not a concern. While we are still above the 5MHz bandwidth window, setting the output to a 5V instead of 3V increases the amount of signal passed on to the DAQ.

2.4 Superachromatic relay lenses

An achromatic doublet or achromat is composed of two single lens elements designed in combination to correct for chromatic aberrations at two target wavelengths. The individual element powers of the doublet are determined by the total power and the individual Abbe numbers of the material. To obtain color correction an achromat has both a crown element and a flint element. Numerically these values are represented by the Abbe number (V_n) where a V_n value of 55 or larger is considered a crown and anything lower is a flint. In the preferred embodiment of a doublet, the Fraunhfer design, a positive crown element is followed by a negative flint element. Doublet elements can be either cemented together for easier alignment and fabrication, or separated by an air-spacer for improved design performance.

Table 2.1: Properties of CaF_2 and sapphire optical substrates used for doublet

Properties	Calcium-fluoride	Sapphire
n(λ_1), n(λ_2), n(λ_3) [μm]	1.4289, 1.4179, 1.3989	1.7557, 1.7122, 1.6239
IR-Abbe number (V_n)	13.98	5.41
Transmission	180nm - 8 μm	150nm - 5 μm
Thermal expansion [1/k]	24×10^{-6}	6.7×10^{-6}
Knoop hardness	158	1370

2.4.1 Design of achromats

For a 2-element lens system to have axial color correction at a given focal length the linear dispersion must be zero and satisfy the following equations

$$\phi_{total} = \sum_{n=1}^{2} \phi_n = \phi_1 + \phi_2 \tag{2.1}$$

$$\sum_n \frac{\phi_n}{V_n} = \frac{\phi_1}{V_1} + \frac{\phi_2}{V_2} \tag{2.2}$$

therefore,

$$\phi_1 = -\phi_2 \frac{V_1}{V_2}. \tag{2.3}$$

Where ϕ is the power of each element and V_n is a modified IR- Abbe number defined over the wavelength range of interest,

$$V_n = \frac{n(\lambda_2) - 1}{n(\lambda_1) - n(\lambda_3)} \tag{2.4}$$

where $\lambda_1 = 1\mu$m, $\lambda_2 = 3\mu$m, and $\lambda_3 = 5\mu$m. Optical and mechanical properties for relevant substrates are reported in table 2.1.

A multi-element lens has a number of parameters that can be adjusted during the design phase; this is a double-edged sword. Each lens has a front radius of curvature, back radius of curvature, and a center thickness, while a mirror has only one surface. In a two-lens design with an air gap, such as the design of our tube lens, there are a total of 7 variable parameters in additional to substrate selection. With this much control, lens systems can be designed for superior aberration mitigation including chromatic aberration.

The most common refractive lens systems for use in the NIR/MIR are plano-convex singlets are made from fluoride crystals. These lenses produce distorted focal spots due to spherical aberration and field curvature, and lack any sort of control on chromatic aberration. Such low performance lenses could greatly benefit from an improved multi-component optical design. In general, the on-axis spot size of an f/5 achromat doublet is ∼25 times smaller than a singlet of the same aperture. Figure 3 shows the profile view of a CaF_2 plano-convex single element lens and an air-spaced CaF_2: sapphire achromat, both with a 150 mm focal length. On the right, the spot diagram summarizes the quality of the focal spot observed in the focal plane on-axis.

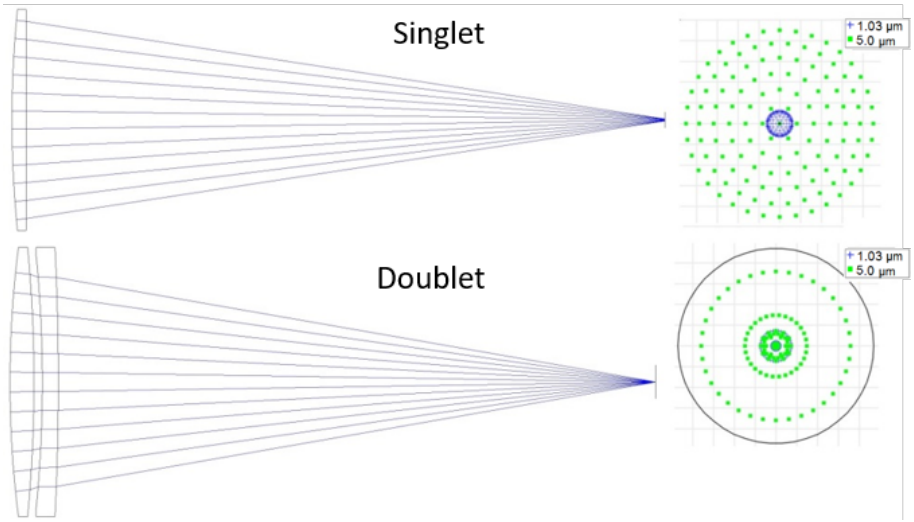

Figure 2.2: Ray diagram and spot diagram of (top) CaF_2 singlet lens and (bottom) CaF_2 and sapphire doublet. The spot diagram shows the energy distribution of two wavelengths at focus. The singlet has poor performance while the doublet is entirely within the Airy disk which defines diffraction limited performance.

The doublet design (bottom) shows that light at 1030 nm and 5μm are focusing entirely within the Airy disk, shown as a black circle that defines diffraction-limited performance. The singlet lens, on the other hand, has such a large focal point that the Airy disk circle defining the diffraction limit cannot be seen (although it is in the very center of the spot diagram). The spot radius for the singlet is 135 μm and about 22 times larger than the 5 μm spots size provided by the doublet. Not only is focusing performance enhanced by

eliminating aberrations, color correction is also included in the design. Figure 8 shows the chromatic aberration, i.e. the change in focal length as a function of wavelength, for the two lens systems. The achromat has a maximum focal shift of 957μm between wavelengths of 1-5 μm with perfect color correction at 1030 nm and 4.2 μm. The singlet lens on the other hand has 11 mm of focal shift between 1-5 μm, which is more than an order of magnitude worse than the achromat's performance.

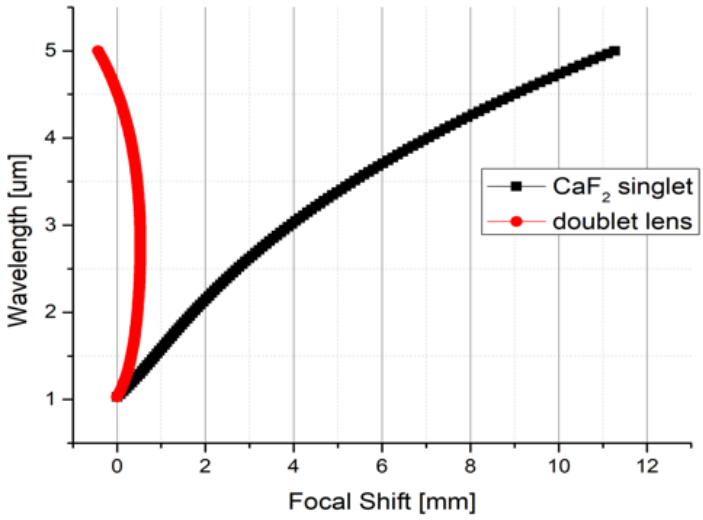

Figure 2.3: Shift in focal length as a function of wavelength for a f= 150mm plano-convex CaF_2 lens (black) and a CaF_2 and sapphire doublet (red). The doublet shows significant improved spectral performance by minimizing color dependent focal lengths.

Prior to the development of the achromats, our microscope relied on plano-convex CaF_2 singlets for the relay optics. They were riddled with third-order and chromatic aberrations. We designed and manufactured a pair of doublets to improve performance. The design parameters closely matched those of the commercial Fluoview 300 system, i.e. a 50mm focal length scan lens followed by a 180mm focal length tube lens– ubiquitous across Olympus microscopes. The 50mm lens was designed as a fast f/2 1-inch optic so that it would be compatible with other experimental setups. The tube lens was designed as an f/6 lens with a 32mm clear aperture. Combined, these lenses form an optical relay system which maps

the plane of the scan mirror onto the back aperture of the objective lens. The lenses were designed to eliminate axial chromatic aberration at 1030nm and 3.8μm, and minimize the rms spot size both on-axis and at a field angle of 5-degrees. Importantly, lateral color was also minimized to ensure spatial overlap of the excitation beams. Both lateral and longitudinal (axial) color corrections are needed for beam overlap, essential for nonlinear generation. The choice of optical materials is key for developing a high performing optic that is also affordable. Common optical materials do not qualify for producing a NIR/MIR superachromat. Common lens materials consist of silica or silicon dioxide (SiO_2) glasses with small percentages of dopants. Yet, all glasses have strong IR absorption beyond 2.5 μm mainly due to hydroxyl bonds in silica. This limitation has severely hampered the advancement of red-shifted achromats beyond the 2.5 μm cliff in the transmission spectrum. The solution for extending transmission beyond this cutoff is the use of non-glass materials. Of the 20 commercially available MIR materials many have insufficiently broad transmission ranges of operation. The remaining materials can be broken up into four categories: fluorite crystals, salt crystals, chalcogenide crystals, and other. There are about a dozen or so optical substrates that transmit light from the visible into the mid-infrared as seen in Figure 5. Our region of interest is highlighted by the blue box; for a material to be considered its transmission has to span the entire width of the blue box.

Fluorites enjoy very low dispersion (high Abbe number) meaning less chromatic aberration. While their index of refraction is low (around 1.4) necessitating strong curvatures and therefore spherical aberration, the mechanical properties are commensurate with easy manufacturability. Of the fluorites, despite being somewhat soft and easily damaged, CaF_2 has the most attractive characteristics including affordability and an anomalous partial dispersion, which helps reduce secondary color. The salt crystals such as NaCl, KBr, and KCl have a higher index of refraction and are affordable. However, they are hygroscopic and, therefore, unattractive for general applications. The chalcogenide crystals are commonly used, but are relatively expensive. An often overlooked characteristic of ZnS and ZnSe in the optics

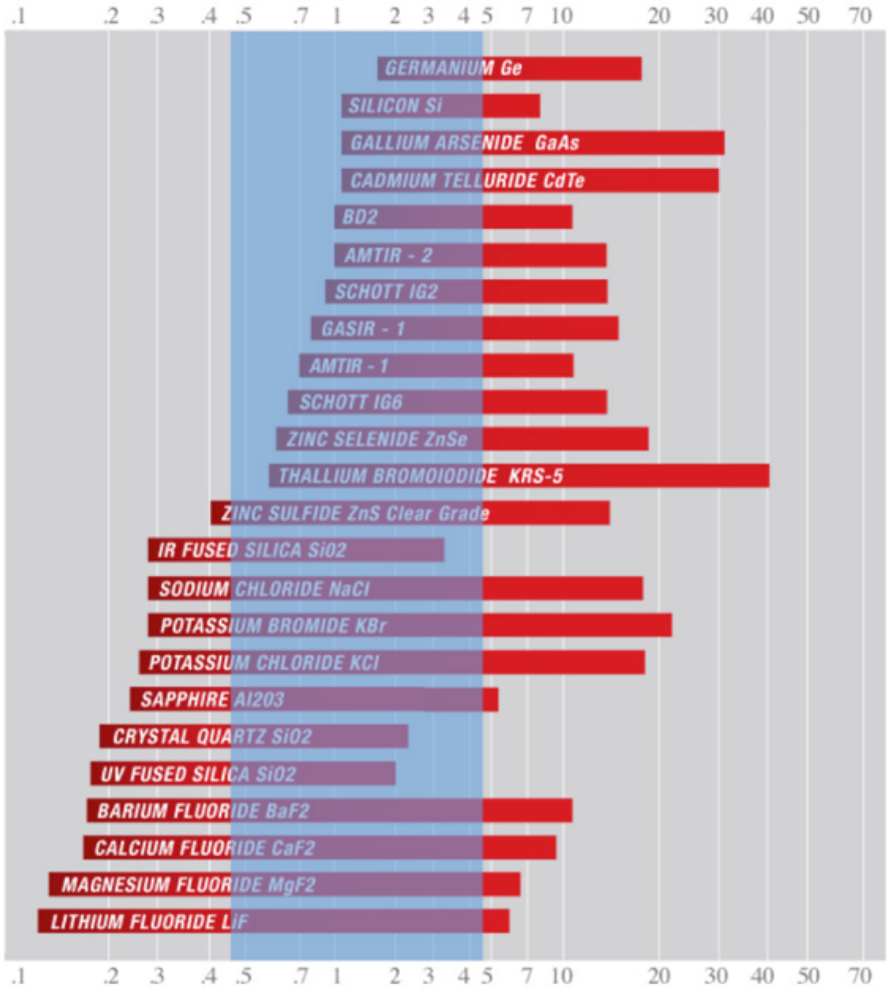

Figure 2.4: x-axis in [μm] Transmission range of commercially available substrates in the MIR. Blue box indicates spectral range of interest. For a substrate to be considered its transmission must span over the entire blue box.

community is their high optical nonlinearity resulting from their Zinc-blend crystal structures. When large peak energies transmit through these materials, as is the case with pulsed lasers, strong second-order nonlinear frequency conversions occur, generating spurious radiation beyond the incident wavelength. This trait is undesirable and therefore these materials are incompatible with high power pulsed lasers for most microscopy applications. Of the few remaining materials, sapphire and KRS-5 (thallium bromiodide) are the most relevant. Although these materials are drastically different, they have rather similar qualities, such as a high index of refraction and a broadband transmission range. Whereas sapphire displays

transmission into the UV, the transmission window of KRS-5 closes at 620nm (it appears red). KRS-5 has good mechanical properties, but due to low quantity and therefore high unit price KRS-5 was not chosen as part of the achromat design. Sapphire, which may sound expensive, is actually commonly used and reasonably priced. Because of its hardness, sapphire is difficult to shape and cannot be diamond-turned, decreasing yield and increasing cost. Sapphire is also birefringent, but has a uniaxial crystal structure so as long as the crystal axis is aligned with the optical axis, known as C-cut, birefringence can be eliminated and the lens can still be compatible with the use of polarized light. Our superachromatic lenses consist of systems composed of CaF2 and C-cut sapphire as the primary materials for the lens system. As underlined by the discussion above, these materials were chosen after careful consideration of numerous relevant parameters and characteristics.

Lenses designed for the MIR have the additional requirement that they cannot be cemented doublets and must be air-spaced. Optical cements are commonly variations of PDMS (poly-di-methyl-siloxane), which suffers from the same parasitic optical absorption as glass. An air-spaced gap has the added benefit that the radii of curvatures of the surfaces facing the air gap do not have to be identical; the additional radius parameter can be varied, which means improved optical performance. However, unlike cemented doublets, air-spaced doublets must be anti-reflection (AR) coated on both sides of the lens, thus increasing production cost. If left uncoated, Fresnel reflections for our design will reduce transmission by about 18 percent. Although broadband AR coatings tend to be thicker and more difficult than narrowband coatings, this is not expected to be a problem for our lenses. Companies that specialize in AR coatings such as ISP Optics have commercially available coating designs that reduce reflections across the broad spectral range of 1-5 μm.

Optimization of the final lens designs were carried out with dedicated optical design software. Zemax is a professional ray tracing program for optimizing lens designs to minimize aberration. It is one of the most popular and trusted lens design software packages used by

optical engineers worldwide.

To ensure a quality product, the design was optimized for manufacturability by running Monte Carlo simulations in Zemax with precision tolerances as defined by Optimax. The worst offenders were surface and element decentration of the sapphire element. The tube lens has an f-number of approximately f/6 and therefore benefited from looser tolerances than the f/2 50mm lens with similar performance.

In our first demonstration of the lenss focusing ability we focused both the 1030nm and the 3.5 μm beams onto a 0.3mm thick GaP crystal for SFG generation. The upconverted signal was detected near 800nm using an Ocean Optics spectrometer and a bandpass filter (FBH800-40). From the data we see that the doublet generated more signal due to a tighter confinement of the excitation fields.

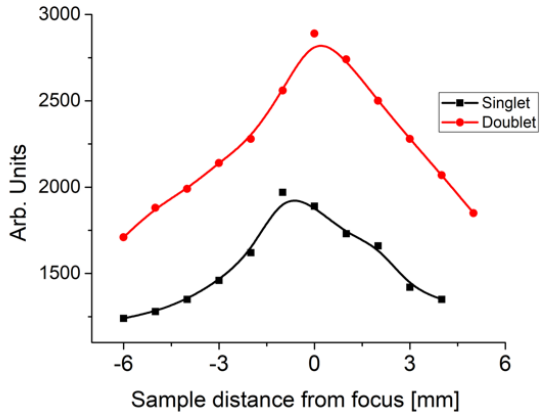

Figure 2.5: SFG signal from a GaP crystal using a CaF_2 plano-convex singlet (black), and an air-spaced achromat (red). Signal with the doublet is much larger due to the tighter overlap in beam focus. Both lenses have approximately 180mm focal length.

We then measured the SFG signal in the SFG microscope. The signal not only was significantly larger with the doublet, the resolution was also increased since the beams had less aberration. To further validate the chromatic shift difference we captured transmission images of an USAF1951 plate using both the NIR and MIR beams as shown below in figure 2.6. On the left we see the images acquired with the singlet, top is with NIR, bottom with MIR.

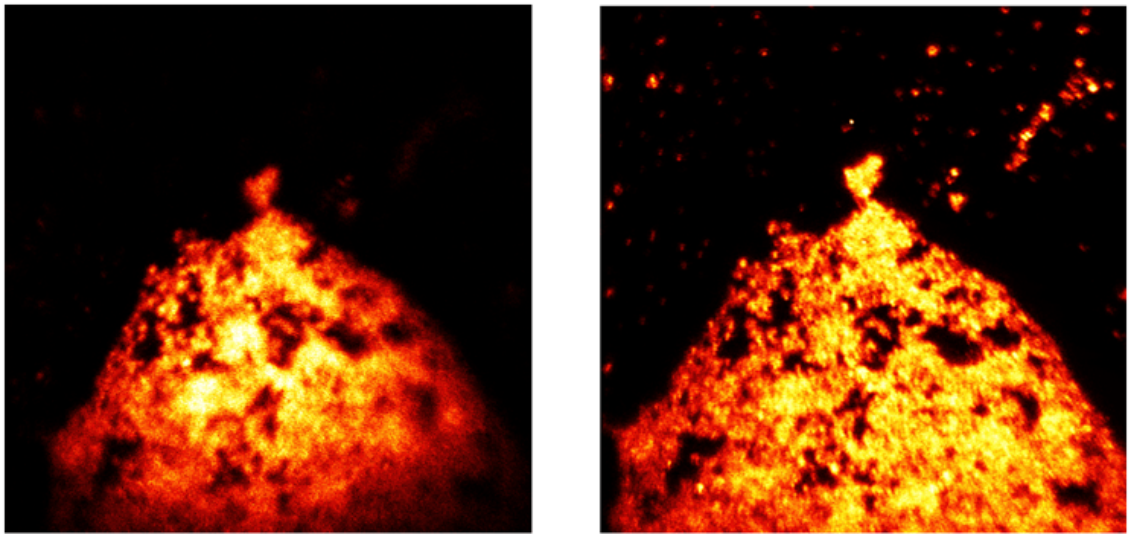

Figure 2.6: Comparison of barium titanate images acquired in the SFG microscope using A. CaF_2 singlets and B. air-spaced achromats for the scan and tube lenses. We see more signal and better contrast with the achromats. Field of view width and height- 80μm.

Similarly on the right, NIR on top and MIR on bottom, but instead using the achromats.

The results are quite clear: when the image plane is in focus for the NIR beam, it is out of focus at the MIR wavelength. However, with the doublets in place both wavelengths are simultaneously in focus at the same focal plane. This development strongly boosts the upconversion efficiency, enabling fast imaging of biological samples, as discussed in Chapters 3–5.

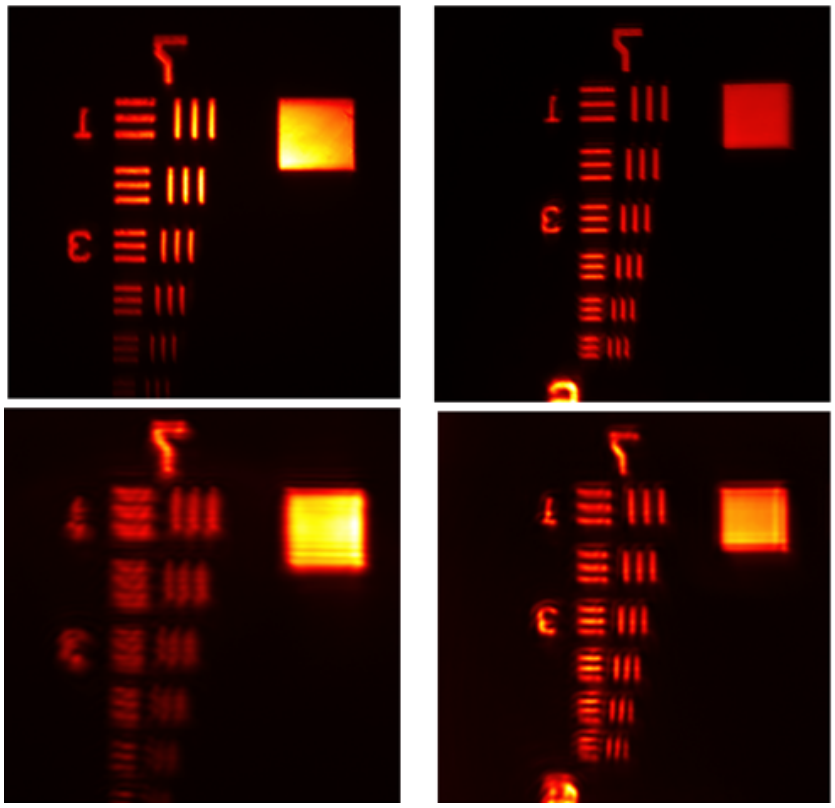

Figure 2.7: Test plate images acquired in transmission using Left. CaF_2 singlets NIR (top) MIR (bottom) and right. air-spaced doublets NIR (top) and MIR (bottom). With the singlets the two colors are out of focus due to chromatic shift, resulting in a blur. This aberration is corrected for with the achromat, bringing both colors to a common focal distance.

Chapter 3

Hyperspectyral Sum Frequency Generation Microscopy

3.1 Introduction

In nonlinear optical (NLO) microscopy, two or more photons combine to interact with the sample and induce a nonlinear polarization, which produces radiation that can be captured with a far-field photodetector. Over the past two decades or so, various NLO imaging techniques have been developed and some of them are now regularly used to support biological and biomedical research [75]. A subset of these NLO techniques are based on the coherent driving of molecules in the focal volume, thus producing coherent radiation. Examples include second- and third-harmonic generation (SHG, THG) [14], coherent anti-Stokes Raman scattering (CARS) and stimulated Raman scattering (SRS) [18]. All these techniques exhibit an intrinsic three-dimensional resolution, and can be conveniently carried out with laser-scanning microscopes, which feature rapid imaging capabilities and are easy to use for routine imaging applications. In fact, a typical laser-scanning NLO microscope incorporates

several detectors for capturing various nonlinear optical signals simultaneously, enabling multimodal imaging.

Vibrationally resonant sum-frequency generation (SFG) is another member of the family of coherent NLO techniques. In SFG, the sample is illuminated by a mid-IR beam at ω_1 and a vis/NIR beam at ω_2, producing a signal at $\omega_3 = \omega_1 + \omega_2$ [100, 18, 118]. It can be considered a hybrid between SHG and CARS. Like SHG, SFG is a second-order optical effect, which relies on non-centrosymmetries in the sample. Like CARS, SFG is based on a vibrational excitation, followed by an anti-Stokes Raman interaction. However, unlike CARS, the vibrational excitation is driven by a low energy, mid-infrared photon (ω_1), rather than by a two-photon Raman interaction. When the energy of the mid-IR photon is near a vibrational resonance, the SFG response is enhanced, giving the technique its vibrational sensitivity. Because of these properties, SFG microscopy is sensitive to the same structures as seen in nonresonant SHG microscopy, with the important difference that it adds (vibrational) spectroscopic contrast to the images.

Despite these attractive properties, SFG microscopy is not frequently used for biological imaging applications. A fundamental complication for the SFG modality is that the mid-IR beam driving the resonant vibration is incompatible with standard microscope optics that accommodate the visible/NIR spectrum. For this reason, SFG microscopes often follow very different excitation and detection strategies compared to a laser-scanning microscope. In particular, several wide-field, non-collinear illumination schemes have been developed and implemented for spectroscopic and microscopic SFG applications. In such wide-field configurations, the SFG radiation from a large area is commonly captured by an objective lens and projected onto a CCD camera [76, 46, 57, 19, 103]. Although useful for spectroscopic studies of surfaces, such microscope designs are less attractive for rapid imaging of three-dimensional cell and tissue samples. An alternative non-collinear excitation scheme, which has been proven more successful for imaging bulk second-order optical nonlinearities in bi-

ological samples, uses oblique illumination of the mid-IR beam (ω_1) whereas the ω_2 beam is tightly focused by a high numerical aperture (NA) lens [73, 80, 71]. In the latter system a confocal detector is used, making it possible to acquire SFG images with sub-μm resolution. Despite these advantages, such a non-collinear design is not compatible with other forms of NLO imaging, thus complicating convenient integration of SFG into a multimodal microscope.

Laser-scanning microscopes make use of collinear illumination of the excitation beams, suggesting that an integrated SFG modality should be based on a collinear excitation geometry as well. Sakai and co-workers implemented a collinear illumination by using a regular lens to focus the ω_1 and ω_2 beams to a common, though shallow, focus [49, 54]. In the case of thin samples, the phase-matched signal in this configuration propagates in the forward direction, along with the excitation beams. If detection is performed with a high NA microscope objective, SFG images can be acquired with a resolution defined by the collecting lens. Even better performance is obtained if the illuminating lens is replaced by a high NA objective, consistent with the layout of a standard laser-scanning microscope. Because the mid-IR wavelengths are not supported by commercial refractive microscope objectives, a reflective objective can be used, which are inherently achromatic. Such a microscope focuses both beams to a tight focal spot, enabling SFG imaging with sub-μm resolution, while retaining much of the design elements of common NLO microscopes. This approach has enabled detailed SFG imaging studies of biological structures with non-vanishing second-order nonlinearities, such as collagen [90, 38, 66, 37] and cellulose [60] fibers.

So far, collinear SFG microscopes have used sample scanning to generate images [90, 60, 117], which is inherently slow. In this work, we demonstrate laser-scanning SFG microscopy by integrating the SFG modality directly into a conventional NLO microscope with only minor modifications. The resulting imaging platform is capable of generating SFG images at unprecedented rates, similar to the frame rate of the accompanying SHG and CARS

signals acquired on the same system. We demonstrate the utility of the laser-scanning SFG microscope by performing hyperspectral and polarization-resolved imaging studies of various relevant biological structures, highlighting the unique information attainable with SFG microscopy beyond what can be obtained with existing modalities. The advances and imaging examples showed herein underline that SFG imaging is an attractive and feasible addition to the multimodal NLO microscope, providing new spectroscopic contrast previously inaccessible in routine imaging applications.

3.2 Methods

3.2.1 Light source

The layout of the laser-scanning SFG microscope is shown in Fig. 3.1. The main light source is a picosecond Er^{+}-doped fiber laser (aeroPULSE, NKT Photonics) centered at 1030 nm (6 ps pulse width, 76 MHz repetition rate) that drives a synchronously-pumped optical parametric oscillator (OPO). The OPO, which is optimized for NIR and MIR generation (Levante IR OPO, APE Berlin), includes a fanned periodically-poled nonlinear crystal, generating a spectrally tunable signal in the 1350 nm to 2000 nm range that is resonant in the OPO cavity. The idler beam, which is generated upon each passage of the signal pulse through the crystal, is coupled out of the cavity and used as the ω_1 beam in the SFG experiments. The idler can be tuned from 2200 nm to 4300 nm corresponding to molecular vibrations in the 2320 cm^{-1} to 4550 cm^{-1} range. In addition to the signal (NIR) and idler (MIR) delivered by the OPO, the residual pump beam can also be used in the NLO experiments. For SFG, we use the idler beam for the ω_1 excitation, whereas the 1030 nm beam is used for the ω_2 excitation. CARS is achieved by using the 1030 nm beam for the pump interaction and the OPO signal for the Stokes interaction. The 1030 nm beam is also used for generating SHG

signals. The beams are conditioned with spatial filters and their linear polarization state is controlled with a polarizer and a half-wave plate. For the mid-infrared beam, a low-order magnesium fluoride half-waveplate ($3\lambda/2$ retardance at 2860 cm^{-1}) and a BaF_2 holographic wire grid polarizer (extinction ratio 150:1 at 3300 cm^{-1}) are used. For the near-infrared beam, an achromatic half-waveplate and a calcite Glan-Taylor polarizer are utilized. Using two custom dichroic mirrors (Layertec GmbH), the beams are combined in a collinear fashion, as shown schematically in Fig. 3.1.

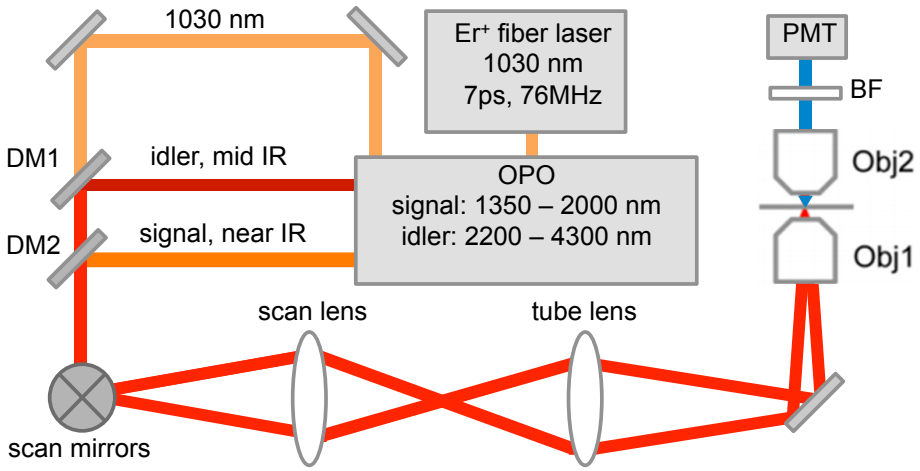

Figure 3.1: Schematic of the SFG microscope. Yb^+ oscillator seeds the OPO. Galvanometric mirrors are part of an Olympus Fluoview 300 laser scanner, and excitation and collection optics are part of an Olympus IX71 frame. PMT: photomultiplier, BF: bandpass filter, Obj: microscope objective, DM: dichroic mirror.

3.2.2 Microscope

The microscope system consists of a modified laser-scanning module (Fluoview 300, Olympus) and inverted microscope frame (IX71, Olympus). To accommodate the NIR and MIR beams, the scan lens (f = 50 mm) and tube lens (f = 180 mm) are replaced by CaF_2 lenses, which are transparent to the relevant range of frequencies used in the experiments.

The beams are steered into the laser-scanning module, passing a set of Al-coated galvonometric mirrors, and coupled into the microscope where they are focused by a 0.65NA, 74x, Cassegrain reflective objective (5007, Beck). The NLO signals are captured in the forward direction by a refractive condenser lens (achromatic/aplanatic condenser, max. NA = 1.40, Olympus) and passed through a short pass and a bandpass filter before being detected by a photomultiplier tube (PMT). In our study, we focus on the vibrational modes near 2945 cm^{-1}, resulting in a SFG and CARS signal near 790 nm. The SHG signal is detected at 515 nm. The average illumination power of the MIR and NIR beams onto the sample were in the 1–4mW and 15–40mW range, respectively. The lateral resolution of the SFG images is dictated by the reflective objective and amounts to ~ 0.6 μm [90]. The axial resolution is inherently affected by the central obfuscation of the Cassegrain objective [66, 122] and is approximately 15 μm.

Note that the polarization conditions in collinear SFG microscopy are markedly different from those in surface SFG spectroscopy experiments. The latter implies that different combinations of tensor elements of the nonlinear susceptibility are probed. The tensor elements are written as $\chi^{(2)}_{ijk}$, where (i, j, k) are the polarization directions of the $(\omega_3, \omega_2, \omega_1)$ fields in the molecular frame. In all SFG experiments reported herein, the linear polarization direction of the ω_1 and ω_2 beams are identical, resulting in excitation fields in the focal plane that have their strongest component polarized in the lateral (XY) plane. No analyzer is used in front of the detector, implying that the experiments are most sensitive to the $\chi^{(2)}_{iXX}$ and $\chi^{(2)}_{iYY}$ tensor elements, where $i = X, Y$ and (XY) are the coordinates of the laboratory frame [37].

3.2.3 Single photon counting

We have incorporated a single photon counter scheme, which provides higher sensitivity than the more conventional analog detection for the signal levels relevant to our experiments.

The current output from the red/NIR sensitive PMT (7422-50, Hamamatsu) is preamplified (TIA60, Thorlabs) and sent to a discriminator (F-100T, Advanced Research Instruments, CO). The discriminator outputs a digital TTL pulse of 5V and a duration of 5ns every time a photon is detected. The advantages here are palpable, as it increases the signal to noise ratio by eliminating the contributions below the discriminator's threshold. A possible drawback is the lower dynamic range of digital detection, as a maximum of one photon per pulse can be detected. However, practical counting rates for the SFG signal are well below the pulse repetition rate (76 MHz), which constitutes a favorable regime for single photon counting. The TTL output pulses are conditioned with a function waveform generator (AFG3102, Tektronix) to yield pulses with an amplitude of 6V and a duration of 10ns. The latter parameters optimizes the integration of the signal pulses by the Fluoview acquisition card. Detection of MIR light without the upconversion process in the light-matter interaction may be possible with a biased silicon or GaAs photodiode, and ideally a focal plane array (FPA). This is acheived by modulating the MIR beam and detecting the non-degenerate TPA when mixed with a NIR beam, which is below the semiconductors bandgap. In our case, a 1480nm beam and a tunable MIR beam around 3.5μm are combined to generate a TPA signal. This could be used to perform linear IR measurements, and may be a preferred detection method in the monolithic fabrication of integrated optic and electric SOI/ SOS devices compared to current MIR sensors riddled with noise and low sensitivity.

3.2.4 Sample

A rat tail, dissected from a rat, was stored at -20 ^{o}C until use. Individual tendon fascicles about 100 μm long were removed from the tendon bundles under a dissecting microscope, and flattened between two cover slips before SFG imaging. The cholesterol sample was obtained by dissolving cholesterol powder (C75209, Sigma-Aldrich) in chloroform and allowing the

solute to recrystallize on the cover slip upon evaporation of the solvent. The medium-sized powdered cellulose fibers (c6288, Sigma-Aldrich) were suspended in a few drops of water, then air dried onto a cover slip.

3.2.5 Image analysis

Hyperspectral images of the samples were acquired to reconstruct the spectra in the CH stretching range (2800 cm^{-1} to 3100 cm^{-1}). Image acquisition times were typically 1 s/frame (512 x 512 pixels). For hyperspectral SFG imaging, images were taken for different wavelength settings of the ilder beam, using manual adjustment of the OPO in between images. Hyperspectral datasets consisted of 20 spectral acquisitions. To facilitate visual inspection of the data, some of the hyperspectral datasets were analyzed with vertex component analysis (VCA) using home-written code in MATLAB. VCA is an algorithm for spectral unmixing, providing pseudocolor contrast highlighting regions within the field of view with distinct spectral features [**?**]. Spectral analysis with VCA has been used previously for Raman [78] and coherent Raman microscopy [111].

3.3 Results

3.3.1 Hyperspectral SFG reveals molecular orientation in fibrous structures

Like SHG microscopy, SFG microscopy is sensitive to molecular orientation. To acquire orientation information in SHG imaging, the polarization direction of the incident fields is

typically varied. In SFG microscopy, however, orientation of molecules can be obtained directly from variations in the spectral features, information that is inaccessible in SHG measurements. In Fig. 3.2, a tendon tissue is visualized with both SFG and SHG contrast. The SHG results are shown in panels (a)–(c). In Fig. 3.2(a), the polarization orientation of the incident beam is aligned with the long axis of the collagen fiber bundles, resulting in a strong signal. When the incident polarization is rotated by 90^o, as shown in Fig. 3.2(b), the signal is significantly lower, except for the region where the fibers are bent. The polar plot in Fig. 3.2(c), acquired from the boxed region of interest, shows a clear dependence of the SHG signal on the polarization direction of the incident beam, which can be related to the orientation of the collagen fibers [89, 108, 114]. Similar information can be obtained from SFG images. In Fig. 3.2(d), the SFG at 2945 cm^{-1} is shown when the polarization direction of both beams are aligned with the main axis of the fibers, while panel 3.2(e) shows the SFG image when the input polarization is rotated by 90^o. Although the features in the image appear sharper in the SFG channel due to a much higher anisotropy of the resonant signal [37], overall the SFG and SHG images appear very similar.

The differences between SHG and SFG imaging become clearer when the SFG image is spectrally resolved. In panel 3.2(f), two SFG spectra are extracted from the boxed areas of panels 3.2(d) and 3.2(e), which are part of a hyperspectral data stack recorded between 2840 cm^{-1} and 3050 cm^{-1}. The red spectrum is obtained from the area indicated in panel 3.2(d), when the polarization direction of the beams is aligned with the long axis of the fibers. This spectrum shows a clear resonance that peaks at 2945 cm^{-1} and mimics previously published SFG spectra in this range [37, 95]. The blue spectrum is acquired in the same area, but with the polarization of the incident beams rotated by 90^o. In the latter setting, SFG signal is significantly weaker. The 2945 cm^{-1} peak is almost completely suppressed for this polarization setting. However, the blue spectrum shows a clear and reproducible feature around 2890 cm^{-1} [37]. This feature is strongest when the polarization of the ω_1 beam is orthogonal to the long fiber axis.

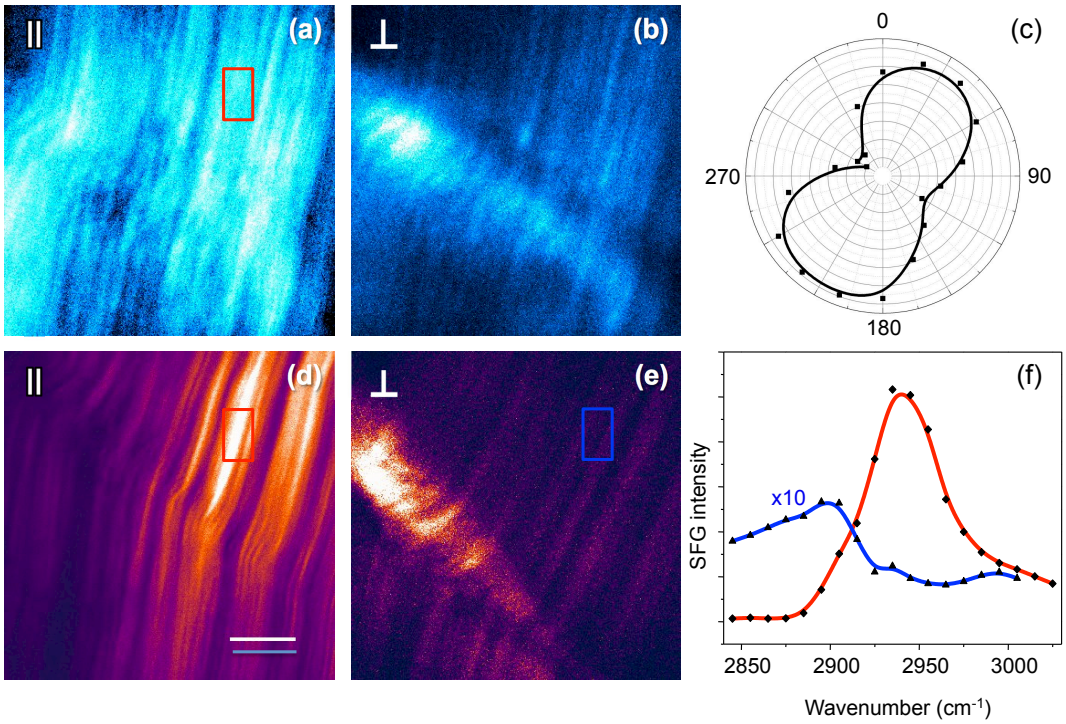

Figure 3.2: SHG and SFG imaging of rat tail tendon, a collagen I rich tissue. a) SHG image obtained with the polarization orientation of the incident beam parallel to the long axis of the collagen fibers. b) SHG image similar to a), but with the polarization orientation rotated by 90^o. c) SHG polarization plot taken in the red region of interest shown in a). Direction refers to the polarization orientation of the incident beam. d) SFG image at 2945 cm^{-1} of the same sample and with the polarization orientation of both beams aligned with the main axis of the collagen tissue. e) SFG image similar to e), but with the polarization orientation rotated by 90^o. f) SFG spectra extracted from the hyperspectral data stack. Red spectrum refers to the region of interest in d) and blue spectrum refers to the region of interest indicated in e). Scale bar is 15 μm.

These different spectral features allow a direct reading of the collagen orientation without the need to change the polarization. This is shown in Fig. 3.3, which shows the VCA image of three end-members extracted from the SFG hyperspectral data stack associated with Fig. 3.2(e). Note that the three endmember spectra retrieved by the VCA are found by linear unmixing of the hyperspectral dataset, and constitute spectral profiles (red, green, blue) through which each pixel can be properly represented as an RGB color. The spectrally unmixed image thus allows for an easy inspection of spectrally significant differences in the dataset. Although the unmixing does not necessarily separate the response into individual

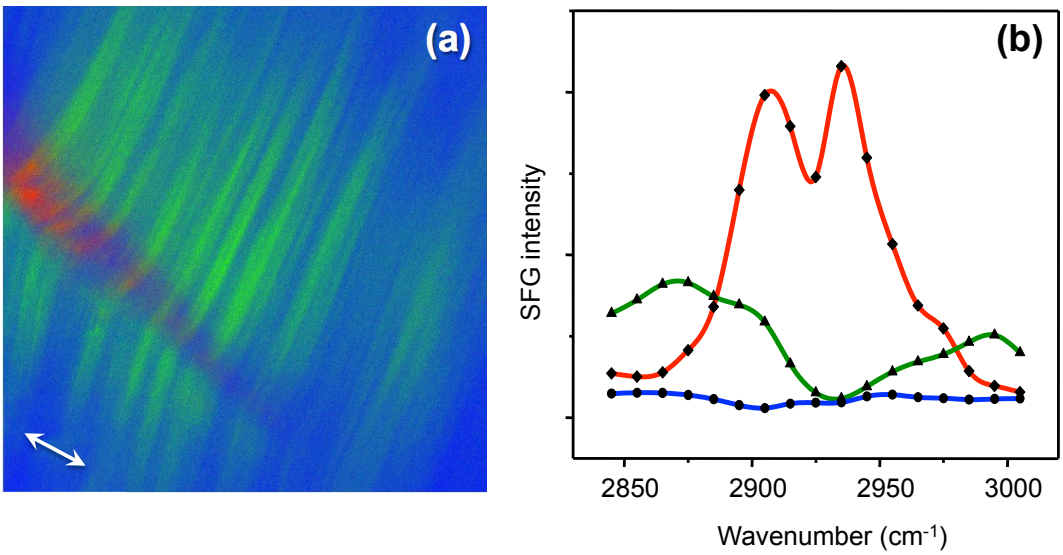

Figure 3.3: Multivariate analysis of collagen rich tissue. a) Vertex component analysis (VCA) image showing three end-members in red, green and blue, based on a hyperspectral SFG data stack. The arrow indicates the polarization direction of the incident beams. b) Corresponding end-member SFG spectra extracted from the VCA.

vibrational modes or tensor elements, the retrieved spectra carry meaningful information on collagen's SFG spectral response. The green spectrum, depicted in Fig. 3.3(b), is reminiscent of the collagen spectrum when the ω_1 polarization direction is orthogonal to that of the fiber alignment. This endmember spectrum shows similarities with the blue spectrum in Fig. 3.2(f). The region where the fibers are bent yields a very different spectrum, represented by the red spectrum in Fig. 3.3(b). This spectrum appears to be a combination of modes, including the 2945 cm^{-1} mode, that are driven in the red region under these polarization conditions. The aligned and bent fibers are clearly demarcated by their SFG spectra, which reflects their orientation, without changing the polarization of the incident beams. Note that a similar feat is not possible with SHG imaging, where rotation of the polarization is required to obtain information on molecular orientation.

Another example of hyperspectral SFG imaging of fibrous structures is shown in Fig. 3.4. Figure 3.4(a) shows an SFG image of a cellulose fiber. Similar to collagen I fibers, cellulose fibers of the Iβ allomorph exhibit a non-vanishing second-order optical nonlinearity [14, 74,

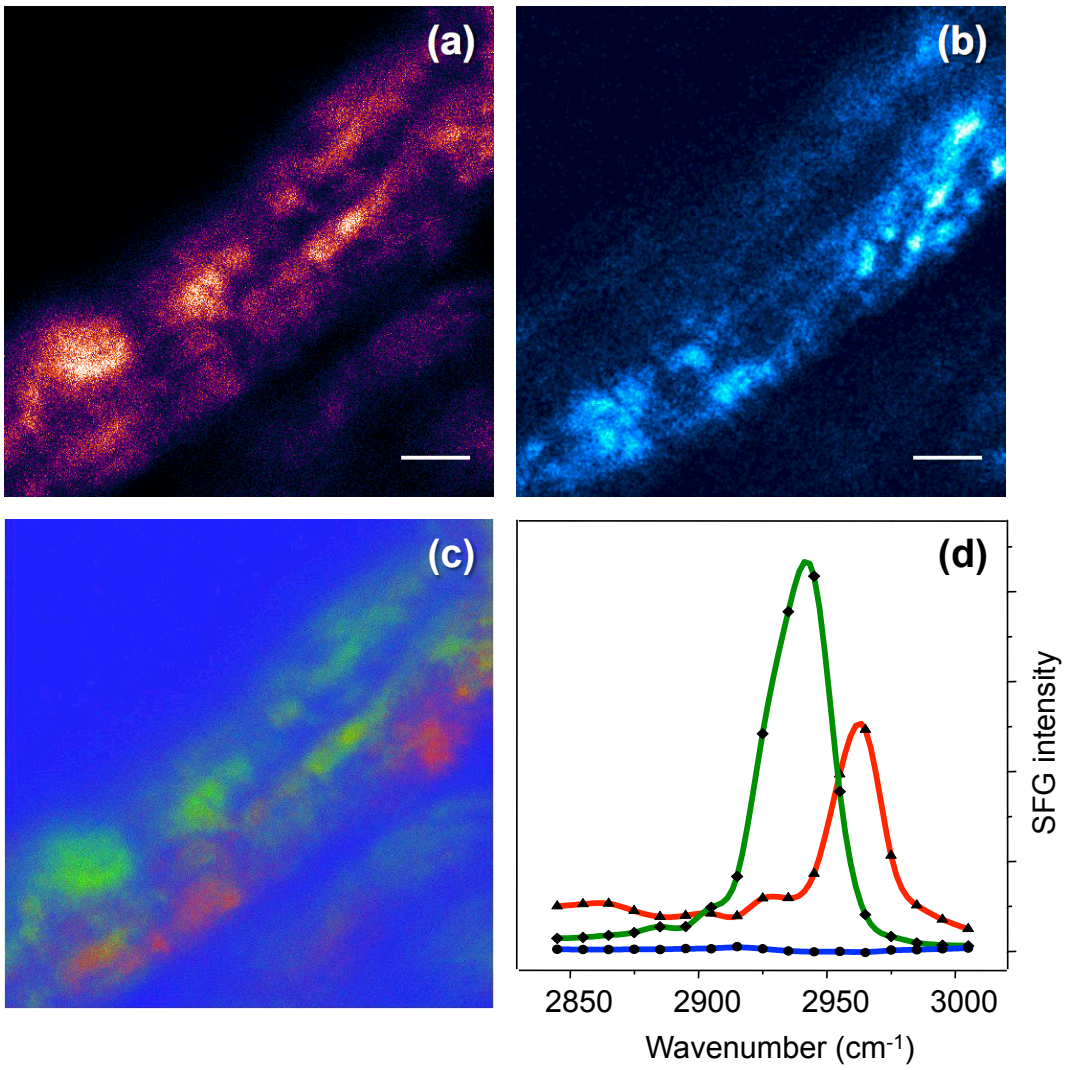

Figure 3.4: Hyperspectral SFG imaging of a cellulose fiber. a) SFG image taken at 2945 cm^{-1}. b) Corresponding SHG image. c) VCA image of the SFG hyperspectral data stack, showing three end-members in red, green and blue. d) SFG end-member spectra obtained from the VCA. Scale bar is 10 μm.

131]. A strong resonant SFG signal from the cellulose fiber is observed when the ω_1 beam is tuned near 2940 cm^{-1} [80, 64, 66, 128]. The corresponding SHG signal is shown in panel 3.4(b). The VCA image from the SFG hyperspectral recording is shown in panel 3.4(c). The VCA spectral segmentation identifies two dominant spectral components, shown in Fig. 3.4(d), that correspond to different regions in the fiber. The SFG spectrum of cellulose Iβ is dependent on molecular orientation and packing [66, 60], and thus the VCA image highlights

microdomains in the fiber with different arrangements of the cellulose units. Similar to the collagen example above, the molecular arrangement information is encoded in the spectral domain and is acquired with a single setting of the incident polarization.

3.3.2 Hyperspectral SFG imaging of crystalline structures

Besides visualizing fibrous structures, the SFG microscope is sensitive to molecular micro-crystals that exhibit non-centrosymmetry. An example is given in Fig. 3.5, which shows SFG imaging results on micro-crystals of cholesterol. At 2850 cm^{-1}, the symmetric methylene stretching vibration, a strong SFG signal is observed from cholesterol. This is evident in Fig. 3.5(a), where several bright domains can be discerned along with dimmer crystalline structures. The signal from these structures is strongly dependent on the polarization direction of the incident beams, as is evident from the SHG polar plot shown in Fig. 3.5(b), which shows the (nonresonant) second-order optical signal for two selected regions in Fig. 3.5(a). The SFG spectra from the same regions of interest are shown in Fig. 3.5(c), featuring several modes in the CH-stretching range. The mode amplitudes of the retrieved spectrum, however, differ from previous SFG measurements of cholesterol in monolayers [53, 33]. The latter can be attributed to the different excitation (polarization) geometry used in SFG microscopy and the fact that the molecular ordering in crystalline cholesterol is different from its arrangement in monolayers. The amplitude of the different modes depends strongly on the orientation of the micro-crystals. This property is utilized in Fig. 3.5(d), where images taken at the 2955 cm^{-1} (blue), 2925 cm^{-1} (green), and 2845 cm^{-1} (red) vibrational energies are normalized and overlaid in a color map. The resulting image illustrates the different orientation of the crystal domains as encoded in the SFG spectra.

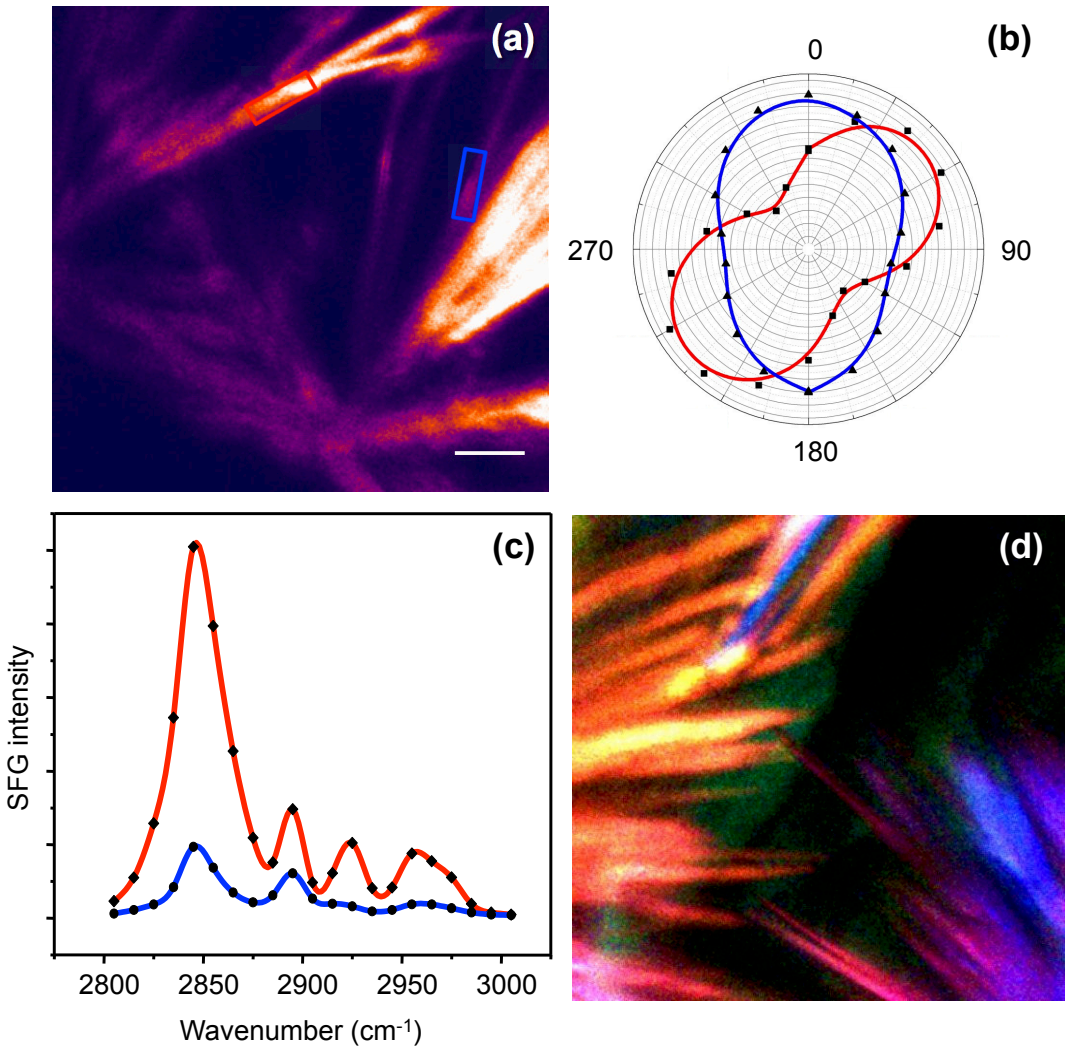

Figure 3.5: SFG imaging of cholesterol microcrystals. a) SFG image at 2845 cm^{-1}. Scale bar is 10 μm. b) SHG polar plots obtained in the red and blue boxed regions of interest of the image in a). c) SFG spectra extracted from the regions of interest in image a). The red spectrum is obtained from the red box, whereas the blue spectrum is obtained from the blue box. d) Composite SFG image formed by overlaying images taken at 2955 cm^{-1} (blue), 2925 cm^{-1} (green), and 2845 cm^{-1} (red).

3.3.3 Multimodal SFG imaging

In previous subsections we have shown SFG and SHG images recorded from the same field of view. It is also possible to acquire CARS images with the same laser-scanning microscope. To generate a CARS image, we add the signal beam of the OPO (ω_s), which acts as the Stokes interaction in the CARS process while the ω_2 ($\lambda = 1030$ nm) beam acts as the pump

interaction. For instance, if we are interested in driving a vibrational resonance at 2845 cm^{-1}, the Stokes beam is tuned to 1457 nm. Note that both the signal and idler beams are delivered by the OPO, and are thus related as $\omega_s = \omega_2 - \omega_1$. In the case all three beams are present (ω_1, ω_2 and ω_s), the CARS and SFG processes both take place. By tuning the idler to a given frequency, both the CARS and the SFG processes drive the sample at the same vibrational energy, because $\omega_2 - \omega_s = \omega_1$. However, since $2\omega_2 - \omega_s = \omega_1 + \omega_2 = \omega_3$, the frequencies of the CARS and the SFG signals are identical as well. Hence, whereas the SHG and SFG signals can be measured simultaneously in different channels, the CARS signal emerges in the same wavelength channel as the SFG signal. To obtain both CARS and SFG images of a given sample, images can be recorded consecutively. SFG is measured when blocking the ω_s beam, and CARS is detected when blocking the ω_1 beam. An example is shown in Fig. 3.6, displaying the SFG and CARS image of a cluster of cholesterol microcrystals visualized at a vibrational energy of 2845 cm^{-1}. Although both modalities probe methylene stretching modes of cholesterol in the images shown, the SFG image is sensitive only to spatial symmetries captured by $\chi^{(2)}$, while the CARS image results from the bulk allowed $\chi^{(3)}$ of the material. The sensitivity to molecular orientation is different between the modalities, resulting in different features in the image. The availability of both the $\chi^{(2)}$ and $\chi^{(3)}$ response at the same vibrational energy is helpful for a more complete analysis of molecular arrangements at the microscale. For example, the combination of SFG and Raman spectral profiles can facilitate the band assignments in the CH-stretching range of microcrystallites like the cholesterol sample shown here. SFG band assignments in this vibrational range can be challenging [118], and the additional information on the polarization properties of spectral signatures provided by Raman can help determine mode symmetry and orientation.

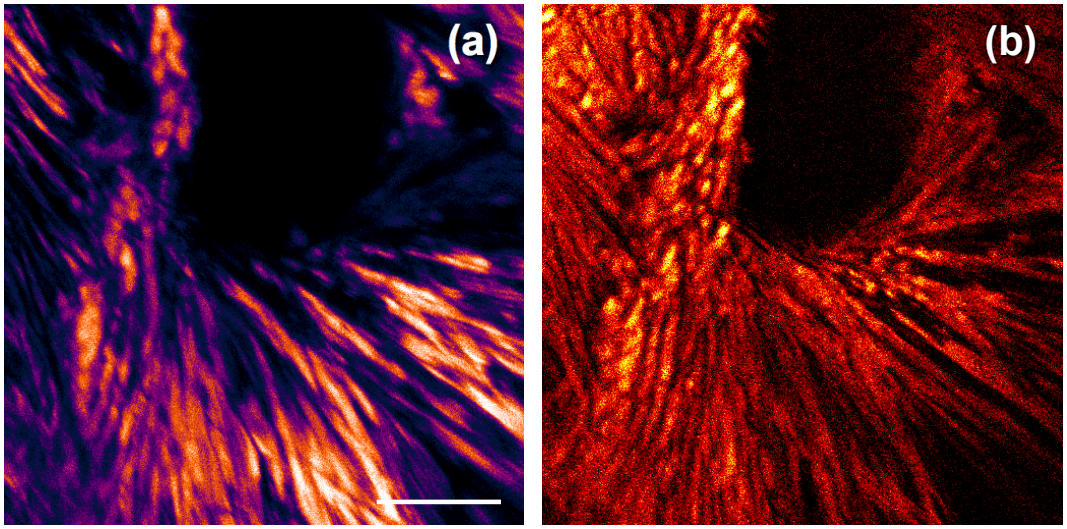

Figure 3.6: Cholesterol microcrystals visualized with a) SFG and b) CARS. Vibrational driving frequency in both images is set at 2845 cm^{-1}. Scale bar is 10 μm.

3.4 Discussion

In this work, we have integrated vibrationally sensitive SFG as a modality into a laser-scanning, nonlinear optical microscope. This advance enabled us to acquire bright SFG images from biological samples with an image acquisition rate of 1 frame/s, similar to the acquisition rate of other NLO modalities. Such a frame rate is almost two orders of magnitude higher than previously reported point-scanning SFG microscopes. With this improvement in scanning speed and ease-of-use, the SFG modality is no longer an exotic variant of NLO microscopy, but can be considered a practical addition to the multimodal NLO microscope.

It is useful to compare the signal strength of SFG microscopy to existing imaging techniques. For instance, at vibrational resonance, the SFG signal is typically stronger that the SHG signal measured from the same sample. In our system, the SHG signal is generated at 515 nm by 15–40 mW of the 1030 nm beam. The SFG signal is generated at the same average power of the 1030 nm beam (ω_2), by adding 1–4 mW of the mid-IR beam (ω_1). Under these conditions, the SFG signal of collagen-rich tissue at 2945 cm^{-1} is almost 10 times as strong

as the accompanying SHG signal. When tuned off-resonance, the SFG signal is comparable to the nonresonant SHG signal. This example shows that the vibrationally resonant SFG signal can be very strong and thus constitutes a practical imaging modality. In terms of signal strength, the image acquisition speed can be improved even more. Currently, the frame rate is limited by the scanning hardware/software of our microscope rather than by the magnitude of the SFG signal.

One of the reasons why SFG has become a feasible contrast option is the practicality of generating the mid-IR pulsed radiation needed for the SFG technique. In most SFG spectroscopic studies, an amplified femtosecond laser system is the standard light source for producing the ω_1 and ω_2 beams. However, amplified laser systems are less suitable for rapid imaging studies, because the pulse repetition rate is typically too low for fast image acquisition. A high repetition rate oscillator in combination with a synchronously pumped OPO is a much more attractive option for laser-scanning microscopy. Such light sources are commonly used in coherent Raman scattering (CRS) microscopy studies and are commercially available. The OPO used here is optimized for generating an idler beam in the mid-IR range, but otherwise the light source is identical to a "conventional" light source for picosecond CRS microscopy.

The NIR/MIR system used in this study enabled us to perform SFG, SHG and CARS imaging studies, using exclusively excitation beams with wavelengths longer than 1 μm. This wavelength regime is interesting for imaging tissue samples with a thickness of up to a few hundred μm. For thicker tissues, the use of MIR light is not practical, as absorption by tissue water gives rise to unwanted heating. The studies discussed in this work were limited to samples of $\sim$100 μm thickness, in which case no noticeable heating effects were observed.

The faster acquisition and integration into a standard microscope platform has enabled us to carry out hyperspectral SFG imaging studies. Hyperspectral SFG microscopy is not new, as several broadband implementations have been described in the literature, both for non-collinear [19, 129] and collinear [60] SFG microscopes. Here we introduce narrowband hyper-

spectral SFG microscopy as an attractive option for spectral mapping of three-dimensional biological samples. This approach is very similar to picosecond hyperspectral CARS [72, 6, 35] and SRS[109, 84, 127] microscopy, where the wavelength of one of the incident beams is systematically varied in between images. At 1 frame/s, the acquisition time of a hyperspectral datastack is limited by the time it takes to change the wavelength. Currently, the wavelength is tuned manually by adjusting the position of the fan-poled nonlinear crystal in the OPO. Automation of this procedure is straightforward, and would enable the acquisition of a hyperspectral datastack within one minute or so.

Through several examples, we have shown that hyperspectral SFG imaging is sensitive to molecular orientation. The use of multivariate analysis of the datastacks has yielded intuitive, spectrally-unmixed images that highlight differences in molecular orientation within the field of view. Although a deeper analysis of the orientation of molecular vibrational modes in the laboratory frame is beyond the scope of this work, it is possible to extract detailed information from the images shown. Recent work has discussed several formalisms of connecting the information from the molecular frame to experimentally accessible parameters [28]. In combination with the proper spectral assignments of the observed bands in the CH-stretching range [43, 44], future work will focus on translating hyperspectral datasets into information on the effective orientation of the molecular modes within the probing volume.

The hyperspectral SFG imaging examples discussed in this work emphasize the use of the technique for studying molecular orientation in detail. However, the utility of spectral SFG mapping is not limited to molecular orientation studies. For instance, examination of image features with new and unexpected SFG spectral features can lead to the discovery of new markers of molecular properties that are difficult or impossible to extract from nonresonant SHG images. The blue spectrum shown in Fig. 3.2(f), for instance, contains a weak but reproducible spectral feature at 2890 cm^{-1}. This feature is maximized when the polarization of the incident beams is orthogonal to the long axis of the fibers, i.e. this signature can be

considered a marker for the short axis of the fiber. This also implies that the 2890 cm^{-1} can be used to visualize collagen fibers that are aligned longitudinally along the axial dimension. In SHG microscopy, longitudinally oriented fibers are very challenging to visualize [93], making it difficult to generate pictures of three-dimensional fiber distributions. The use of SFG, which uses unique information encoded in the spectral dimension, might offer a solution for directly and confidently imaging of out-of-plane fibers.

Although the current multimodal NLO microscope allows the generation of hyperspectral SFG images with good contrast, several improvements would enhance the image quality even more. First, the singlet CaF_2 scan and tube lenses used in this study suffer from chromatic aberrations. Because the spectral gap between the NIR and MIR beams is substantial, chromatic aberrations are inevitable. These aberrations are expected to deteriorate the image quality for large scan angles and thus limit the workable field of view of the microscope. The design of refractive lenses that are achromatic over the NIR/MIR range would improve the field of view and image quality accordingly. Second, although the reflective objective used in our SFG studies is achromatic, the Cassegrain reflector blocks the center portion of the beam and limits the angular components needed for forming a focal volume that is highly confined in three-dimensions [61]. As a consequence, compared to refractive objectives, the use of the reflective objective elongates the focal volume along the optical axis and decreases the axial resolution. The design and incorporation of a fully refractive objective lens with achromaticity over the desired NIR/MIR range, would significantly benefit the SFG modality.

3.5 Conclusion

In this work, we have made simple modifications to a commercial laser-scanning microscope to enable the generation of SFG images in an easy and rapid manner. The improvement in image acquisition time by almost two orders of magnitude compared to previous point-

scanning SFG microscopes has also allowed us to record hyperspectral SFG datastacks and perform multivariate analysis of various spectral signatures of the sample. These imaging capabilities make it possible to study the microscopic arrangement of molecules in detail. The advances discussed in this work add some of the unique properties of SFG spectroscopy to the convenience of a laser-scanning microscope, establishing SFG imaging as a valuable member of the family of NLO microscopy techniques. We thank Dr. Giuseppe de Vito for helping out with the early stages of this work. Alba Alfonso-García was instrumental in writing the code for the multivariate analysis.

Chapter 4

Triple Modal Coherent Nonlinear Imaging With Vibrational Contrast

In coherent nonlinear optical spectroscopy, molecules are driven in unison with laser beams to induce a coherent radiative response. The coherent excitation of an ensemble of molecules can reveal important information about the dynamics of relevant molecular states, information that is often difficult to obtain from linear spectroscopy measurements [82]. In addition, the coherent driving mechanism gives rise to a signal that benefits from the aligned phases of the waves radiated from the sample. The resulting mutual constructive interference between the waves produces a signal that can be of appreciable magnitude in a phase-matched direction. This latter property of signal coherence can be useful for amplifying otherwise weak optical effects. Coherent Raman scattering (CRS) is a prime example of a nonlinear optical technique that takes advantage of the coherent amplification of the optical response, yielding signals that can be orders of magnitude stronger than linear Raman signals.

The stronger signals afforded by the coherence among the driven molecules have enabled CRS measurements of very small sample volumes at rapid signal acquisition speeds. CRS

microscopy makes use of this capability, offering vibrational Raman signals from microscopic volumes with pixel dwell times of microseconds or less [18, 13, 88]. Coherent anti-Stokes Raman scattering (CARS) and stimulated Raman scattering (SRS) microscopy are both successful implementations of CRS, enabling real time imaging applications with vibrational spectroscopic contrast [31, 97], despite the intrinsic weakness of the Raman scattering effect. Laser-scanning CRS microscopy has matured into a trusted imaging tool with applications in cell and tissue biological research [59, 67], as well as pharmaceutical research [123, 102, 106], food science [77, 96] and material analysis [115, 65, 12].

The success of CRS microscopy has opened the door to adopting other forms of coherent vibrational spectroscopy as imaging contrast mechanisms in laser-scanning microscopy. In this regard, it would be particularly useful to have access to spectroscopic signatures that are complementary to those provided by CRS. Since CRS methods probe Raman active molecular modes, additional spectroscopic information is obtained through methods that probe vibrational modes with strong infrared (IR)-activity. Vibrationally sensitive sum-frequency generation (SFG) is a coherent spectroscopic technique that uses infrared radiation to drive a vibrational mode, followed by a Raman interaction to generate a signal in the visible or near-IR range [100, 30]. The SFG light-matter interaction has been successfully used as a contrast mechanism in microscopy [76, 46, 19, 73, 49, 90, 103, 60, 117], and has recently been integrated into a laser-scanning microscope [40]. Like second-harmonic generation (SHG) microscopy [85], laser-scanning SFG microscopy is sensitive to non-centrosymmetric structures such as fibrillar collagen, which display a non-vanishing second-order susceptibility $\chi^{(2)}$. With SFG microscopy it is possible to visualize such structures with spectroscopic vibrational contrast, thus enabling a deeper analysis of molecular structure than what is possible with nonresonant SHG microscopy. Bulk-sensitive SFG microscopy has been used to study collagen-rich tissues [38, 37], cellulose fibers[80, 40] and biomolecular micro-crystals [18].

Adding a SFG module to the laser-scanning CRS microscope enables a more complete vi-

brational spectroscopic analysis of the sample. Advances in coherent light sources and microscope optics have made it possible to perform multi-modal CRS and SFG imaging studies [40]. However, although SFG adds complementary contrast to CRS images, it does not constitute a direct IR-active analogue of the Raman-based contrast of the CRS microscope. First, since SFG signals originate from non-centrosymmetric structures, SFG microscopy is only sensitive to particular molecular assemblies and materials. On the other hand, CRS microscopy probes the bulk-allowed $\chi^{(3)}$ properties of the specimen. This implies that CRS contrast is not restricted by the condition of non-centrosymmetry, thus opening up its application to a wider range of samples. Second, the vibrational modes probed in the SFG interaction must exhibit both Raman and IR-activity. Consequently, SFG is sensitive to a only sub-set of the Raman-active modes, thereby suppressing vibrational modes that are predominantly IR-active (with little to no Raman activity).

An alternative excitation scheme that involves an IR excitation followed by a two-photon upconversion would fill the remaining void left by CRS and SFG vibrational microscopy. This third-order sum-frequency (TSFG) process, which relies on the $\chi^{(3)}$ response of the material, is bulk-allowed and sensitive to IR-active modes. Versions of the TSFG interaction have been used in electronically resonant and non-resonant fashion in microscopy [99, 98], bearing a close resemblance to third-harmonic generation (THG) imaging [4, 105, 125]. Vibrationally sensitive forms of TSFG have been used in (bulk) spectroscopy studies, using two-photon IR excitations to induce vibrational transitions [9, 113]. So far, TSFG has not yet been used to generate vibrationally sensitive images in a laser-scanning microscope.

In this contribution, we discuss the possibility to perform imaging studies with vibrational contrast provided by CARS, SFG and TSFG. All three techniques are sensitive to vibrational molecular motions and produce coherent optical signals. The combination of these nonlinear optical methods on a single imaging platform permits a complete vibrational spectroscopic assessment of the sample at high spatial resolution. We provide a brief overview of

the capabilities of these nonlinear optical processes and describe how they can be integrated into a laser-scanning microscope. In particular, we report the first TSFG images with vibrational contrast. In addition, we point out some interesting imaging properties of the different modalities and present examples of multi-modal vibrational imaging of micro-structured samples. Finally, we discuss the prospects and challenges of triple-modal vibrational nonlinear microscopy in the context of biomedical imaging.

4.1 Coherent vibrational microscopy

4.1.1 Probing vibrational coherences

The SFG, CARS and TSFG techniques derive their vibrational sensitivity from the induced vibrational coherence in the sample. In SFG and TSFG, this coherence between the ground state and the vibrationally excited state of the molecule is established with an IR pulse of frequency ω_{IR}, tuned to the frequency difference ω_ν between the molecular states. In CARS, the vibrational coherence is driven by two light fields at frequencies ω_p (pump) and ω_S (Stokes) through a Raman interaction, such that $\omega_p - \omega_S = \omega_\nu$. To probe the vibrational coherence of the sample, both SFG and CARS use an anti-Stokes Raman interaction to translate the magnitude of the coherence at ω_ν into signal field amplitude. Hence, if the ω_p field is used as the probe, then both SFG and CARS generate signals at $\omega_p + \omega_\nu$, which typically corresponds to a frequency in the visible or near-IR (NIR) range of the spectrum. On the other hand, the TSFG probing interaction is based on an anti-Stokes hyper-Raman process, producing a signal at $2\omega_p + \omega_\nu$. Figure 4.1 shows the Jablonski energy diagrams for the three nonlinear processes. Table 4.1 summarizes several key properties of the SFG, CARS and TSFG techniques.

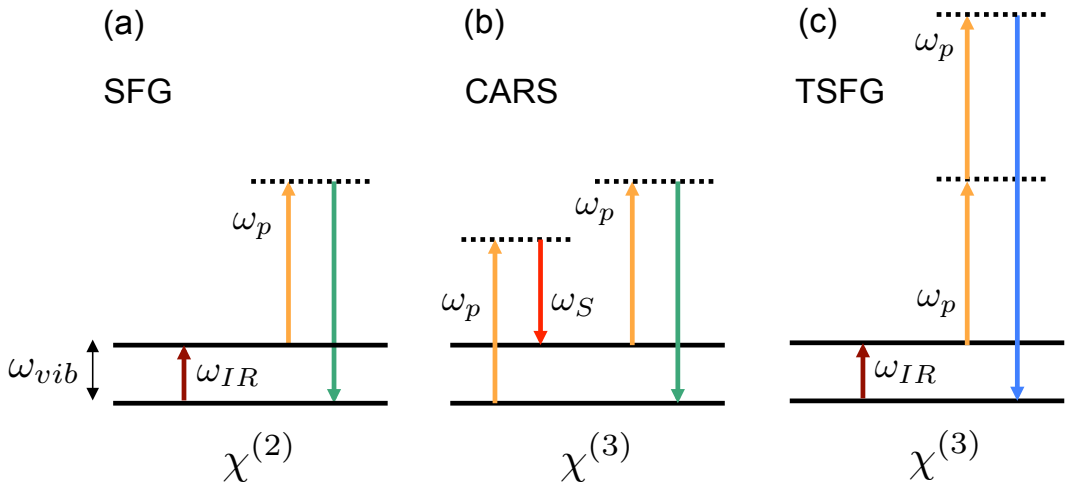

Figure 4.1: Jablonski diagrams of the (a) SFG, (b) CARS and (c) TSFG processes.

4.1.2 Selection rules

The CARS process involves two sequential Raman interactions. Therefore, it probes vibrational modes that are Raman-active, i.e. that display a change in the (electronic) polarizability upon a displacement of the nuclei. Vibrational modes that are highly symmetric are usually highly Raman-active.

The SFG process includes a direct dipole-allowed transition followed by an anti-Stokes Raman interaction. This excitation scheme is sensitive to modes that are both IR and Raman-active [100, 116]. In practice, many vibrational modes of biomolecules exhibit the required combined IR and Raman activity.

The TSFG process relies on a dipole-allowed vibrational transition, which imposes that the mode be IR-active. Modes that produce a change in the electric dipole moment as a function of the nuclear displacement are IR-active. The anti-Stokes hyper-Raman probing interaction of the TSFG process is sensitive to IR-active modes as well [25, 130]. Although hyper-Raman interactions also probe modes that are non-IR-active, the latter modes are not registered in the overall TSFG nonlinear process, which is thus only sensitive to IR-active modes. Hence, the spectral properties of the TSFG technique are expected to be closely related to the

sample's infrared absorption spectrum.

4.1.3 Nonlinear susceptibilities

The magnitude and frequency-dependence of the nonlinear optical signals can be estimated from expressions for the material's nonlinear optical susceptibility $\chi^{(n)}$, as obtained through perturbation theory in the semi-classical framework [82]. Here n is the order of the light-matter interaction, which is $n = 2$ for SFG and $n = 3$ for CARS and TSFG. The nonlinear susceptibilities are tensors of rank 3 ($n = 2$) and 4 ($n = 3$), which relate the vectorial components of the incident fields to the vectorial components of the induced polarization in the material. However, to simplify the discussion here, we will ignore the tensor character of the nonlinear susceptibility and instead study some of its properties in scalar form. In this context, the nonlinear optical susceptibilities probed in each of the three vibrationally sensitive methods can be summarized as:

$$\chi^{(2)}_{SFG}(\omega_{IR}) = \chi^{(2)}_{nr,SFG} + \chi^{(2)}_{r,SFG}(\omega_{IR}) \tag{4.1}$$

$$\chi^{(3)}_{CARS}(\omega_p - \omega_S) = \chi^{(3)}_{nr,CARS} + \chi^{(3)}_{r,CARS}(\omega_p - \omega_S) \tag{4.2}$$

$$\chi^{(3)}_{TSFG}(\omega_{IR}) = \chi^{(3)}_{nr,TSFG} + \chi^{(3)}_{r,TSFG}(\omega_{IR}) \tag{4.3}$$

All the nonlinear susceptibilities above include a vibrationally non-resonant term $\chi^{(n)}_{nr}$ and vibrationally resonant $\chi^{(n)}_{r}$ term. The nonresonant terms result from electron motions in the molecule without direct involvement of the nuclear modes. The nonresonant contributions introduce a background, which, in some cases, can be strong and overwhelm the vibrational contributions to the signal. Note that the nonresonant contributions for the different techniques correspond to different electron motions and thus have different values, i.e. $\chi^{(3)}_{nr,CARS}$ and $\chi^{(3)}_{nr,TSFG}$ are not the same. The vibrationally resonant terms are explicitly frequency

dependent and can be written as:

$$\chi^{(2)}_{r,SFG}(\omega_{IR}) = \sum_{\nu} \frac{a_\nu}{\omega_\nu - \omega_{IR} - i\gamma_\nu} \tag{4.4}$$

$$\chi^{(3)}_{r,CARS}(\omega_p - \omega_S) = \sum_{\nu} \frac{b_\nu}{\omega_\nu - (\omega_p - \omega_S) - i\gamma_\nu} \tag{4.5}$$

$$\chi^{(3)}_{r,TSFG}(\omega_{IR}) = \sum_{\nu} \frac{c_\nu}{\omega_\nu - \omega_{IR} - i\gamma_\nu} \tag{4.6}$$

The summation is over the molecular states ν and the dephasing parameter γ_ν is a measure of the homogeneous linewidth of the transition from the ground state to state ν. The parameters a_ν, b_ν and c_ν are proportional to the transition dipole moments involved in each of the nonlinear interactions. It can be seen that $\chi^{(2)}_{SFG}$ and $\chi^{(3)}_{TSFG}$ are both resonant when ω_{IR} approaches a vibrational frequency ω_ν. In CARS, the nonlinear susceptibility is enhanced when $\omega_p - \omega_S$ approaches ω_ν.

In all cases, the signal is generated at a frequency different from the frequency of the incident fields. The amplitude of the signal field is proportional to the nonlinear susceptibility. The far-field photo-detector is sensitive to the square of the signal field, which implies that the detected signal $S(\omega)$ is proportional to $\left|\chi^{(n)}\right|^2$. This is the so-called homodyne detection mode, as the signal field is not mixed with another reference field but detected as a complex product with itself. The modulus square of the nonlinear susceptibility introduces mixing terms between the resonant and nonresonant contributions:

$$S(\omega) \propto \left|\chi^{(n)}_{nr}\right|^2 + \left|\chi^{(n)}_{r}(\omega)\right|^2 + 2\chi^{(n)}_{nr}\mathrm{Re}\left\{\chi^{(n)}_{r}(\omega)\right\} \tag{4.7}$$

The last term on the right hand side of Equation (4.7) gives rise to a dispersive lineshape. The stronger the nonresonant contribution relative to the vibrational contribution, the more dispersive the band profiles. Because in typical CARS applications the nonresonant com-

ponent can be substantial, the lineshapes exhibit a significant dispersive character [29]. Although $\chi^{(2)}_{nr}$ is often smaller in SFG applications, homodyne-detected SFG band profiles are nonetheless inherently dispersive. Based on similar arguments, it is expected that the spectrally-resolved TSFG signal also displays dispersive lineshapes.

In the homodyne detection scheme, all three nonlinear processes shown in Figure 4.1 are parametric, i.e. the initial and final states of the molecule are the same, implying that no effective energy transfer has taken place between the light fields and the molecule [91, 36]. The molecular resonances thus act as facilitators in transferring energy between the light fields, without explicitly absorbing energy. This does not mean that the material remains cold while illuminated with the incident pulses, as there are other processes such as linear heating at ω_{IR} or Raman heating at $\omega_p - \omega_S$ (through SRS) that occur simultaneously.

4.1.4 Phase matching

As in all forms of coherent spectroscopy, efficient transfer of energy from the incident fields to the signal field can only take place under proper phase matching conditions. The polarization induced by the incident fields must sustain a spatial phase in the interaction volume that mimics the phase of a propagating signal field. If the phase difference $\Delta\Phi$ between the propagating field and the induced polarization is larger than π, energy cannot be efficiently transferred to the signal field. The phase difference is found as $\Delta k \cdot L$, where Δk is the difference in the wavevector projections of the interacting fields in the propagation direction, and L is the distance over which the fields interact. In SFG, CARS and TSFG, the wavevector mismatch Δk is not zero. However, if L is sufficiently short, the product $\Delta k \cdot L$ can still be smaller than π and thus phase-matching can be achieved [50].

In nonlinear coherent microscopy, the incident fields are commonly focused in the sample in a collinear fashion with the aid of a high numerical aperture (NA) lens. In this scenario, the

fields only interact over a distance of a few μm or less in the main propagation direction. When the signal is collected in the forward propagating direction, $\Delta k \cdot L$ is smaller than π for all three nonlinear techniques discussed here, including TSFG. Consequently, the signal is not limited by phase shifts due to the wavelength dependent wavevector mismatch. However, another source of phase differences between the interacting fields, namely the Gouy phase shift, can affect the magnitude and propagation direction of the signal. The Gouy phase shift is an additional $\phi_i = \pi$ phase shift that a field E_i accumulates when propagating through a focal waist. In CARS, the Gouy related phase difference is $\Delta\Phi_g = 2\phi_p - \phi_S - \phi_{sig}$, where ϕ_{sig} is the Gouy phase shift of the signal field. Because the π phase shift is accumulated within approximately 1 μm of propagation lengths for all beams, the effective Gouy phase difference is $\Delta\Phi_g \approx 2\pi - \pi - \pi \approx 0$. The CARS signal is thus not significantly affected by the Gouy phase shift [50].

In SFG, on the other hand, $\Delta\Phi_g = \phi_{IR} + \phi_p - \phi_{sig}$. Using the same reasoning as above, we obtain $\Delta\Phi_g \approx \pi$, which would be significant enough to affect the energy transfer to the signal field, especially along the on-axis propagation direction. Indeed, the Gouy phase mismatch of about π is the reason for the off-axis radiation profiles that are familiar in SHG microscopy [81, 16]. In SFG, however, the focal depth of the ω_{IR} field is significantly larger than that of the other fields, which means that the interaction between the fields does not take place over the entire distance over which the ϕ_{IR} phase shift evolves. Effectively, $\Delta\Phi_g < \pi$ and the radiation profile in collinear SFG microscopy is expected to be less affected by the Gouy phase shift than is typical in SHG microscopy.

A similar comparison is relevant for TSFG microscopy, which is closely related to THG imaging. It is well known that the Gouy phase mismatch in THG microscopy amounts to about 2π, which is substantial and effectively suppresses the forward propagating signal from bulk materials [16, 23]. This large phase mismatch is the reason for the sensitivity of THG to interfaces and sub-wavelength interfacial structures. In TSFG, which substitutes one of

Table 4.1: Properties of SFG, CARS and TSFG imaging methods

Properties	SFG	CARS	TSFG
Mode selectivity	IR + Raman active	Raman-active	IR-active
Susceptibility	$\chi^{(2)}$	$\chi^{(3)}$	$\chi^{(3)}$
Sample symmetry	non-centrosymmetric	all	all
Power dependence	$I_{IR}I_p$	$I_p^2 I_S$	$I_{IR}I_p^2$
Lineshape	dispersive	dispersive	dispersive
Conc. dependence	c^2	c^2	c^2
Gouy $\Delta\Phi_g$	$< \pi$	≈ 0	$< 2\pi$
Lateral resolution	sub-μm	sub-μm	sub-μm

the fields with a field of longer wavelength, it can be predicted that $\Delta\Phi_g < 2\pi$. However, the Gouy-related phase mismatch is larger than π, so significant distortion of the radiation profile can be expected which may suppress the signal from bulk materials.

The effective phase shifts are ultimately determined by the details of the spatial phase of the focal fields. These parameters are primarily determined by the wavelength of light and the characteristics of the focusing lens. For the reflective objective used in the studies described herein, the axial extent of the focal volume is significantly larger than what is common for the depth of focus achieved with refractive objectives. We may therefore expect somewhat different phase-matching conditions relative to the situation with refractive high numerical optics. We will discuss this point in more detail in Section 4.3.3.

4.2 Nonlinear optical microscope for multi-modal vibrational imaging

4.2.1 Light source

The common implementation of the nonlinear optical (NLO) microscope uses a tight focal spot that is raster-scanned rapidly across the sample. The light source is chosen such that the pulse conditions in focus are optimal for generating the highest amount of signal in the shortest amount of time without altering the sample. Nonlinear optical processes are more efficient for higher peak powers, which can be achieved by shortening the pulses while keeping the average power below the limits set by linear heating of the sample. At the same time, the sampling rate is improved by increasing the pulse repetition rate. For this reason, femtosecond laser oscillators with repetition rates in the 50–100 MHz range have become the standard light source in NLO microscopy, in particular for use in two-photon excited fluorescence (TPEF) and SHG imaging studies [104, 47].

For vibrational microscopy, spectral resolution is an additional requirement. The use of picosecond light sources constitutes a straightforward solution. Although picosecond pulse trains offer lower peak powers compared to femtosecond pulse trains at the same average power, they provide pulses with spectral widths that comply with the linewidths of the vibrational spectrum (~ 10 cm^{-1}), enabling selective excitation of vibrational modes. Picosecond lasers, often in combination with a synchronously pumped optical parametric oscillator (OPO), have successfully powered CRS microscopes for the last 15 years or so [50, 34, 6]. These sources provide pump and Stokes beams with average powers and pulse energies in the range of 5–30 mW and 60–320 pJ at the sample, respectively, which produce strong CRS signals at ~ 1 μs pixel dwell times in a typical laser scanning microscope.

The OPOs used in CRS microscopy produce signal (ω_s) and idler (ω_i) beams. Whereas the

ω_s beam is often used in combination with the pump laser beam (ω_p) for NIR illumination of the sample in CRS imaging, the idler beam extends out to much longer wavelengths. OPOs pumped by the fundamental of ps Nd:vanadate or Yb-fiber lasers deliver idler beams that are tunable into part of the MIR (2.2–4.8 μm), corresponding to the vibrational energies of C-H, O-H and N-H stretching modes. Consequently, such light sources are not only suitable for CRS, but also for SFG [90, 40] and TSFG vibrational imaging.

For the triple-modal vibrational imaging studies described here, we use a 10 W Yb-fiber laser (aeroPULSE, NKT Photonics) that produces 5 ps pulses with a center wavelength of 1030 nm and a pulse repetition rate of 76 MHz. The 1030 nm beam pumps a synchronously pumped OPO (Levante IR ps, APE Berlin), which delivers a signal (1.35–2.00 μm) and idler (2.2–4.7 μm) beam. The combination of the fundamental, signal and idler enable CARS, SFG and TSFG with a single light source. For CARS, we use the fundamental as the ω_p beam and the signal as the Stokes ω_S beam. To drive the 2845 cm^{-1} vibrational mode, the Stokes is tuned to 1460 nm with the pump fixed at 1030 nm, producing an anti-Stokes signal at 796 nm. For SFG, we use the idler as the ω_{IR} beam and the fundamental as the ω_p beam. The vibrational energy of 2845 cm^{-1} corresponds to an idler wavelength of 3515 nm, generating a SFG signal at 796 nm (same as in CARS). The same combination of beams is used for TSFG imaging, using the ω_p beam twice for the up-conversion. For the 2845 cm^{-1} mode, the TSFG signal appears at 449 nm. Tuning of the vibrational resonances in SFG and TSFG is accomplished by spectrally tuning the idler (ω_{IR}) beam. With the pump beam fixed at 1030 nm, the signal wavelength thus varies when probing different vibrational energies.

Before sending the excitation beams into the laser-scanning microscope, they are each conditioned with spatial filters, properly delayed with translation stages and collinearly combined at custom dichroic mirrors (Layertec, GmbH). A schematic of the setup is shown in Figure 4.2.

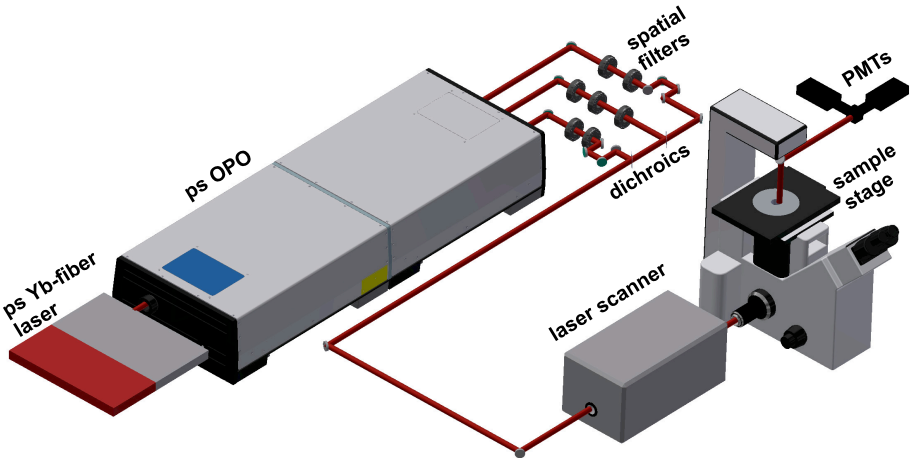

Figure 4.2: Schematic of the triple-modal vibrational microscope system. The synchronously-pumped OPO delivers three beams (ω_p, ω_S and ω_{IR}) that are properly conditioned, delayed and collinearly combined on dichroic mirrors. The imaging platform is a modified laser-scanning microscope, optimized for NIR and MIR throughput. The condenser lens and detection bandpass filters are not explicitly shown in this schematic.

4.2.2 Microscope

Because commercial laser-scanning microscopes are optimized for visible to NIR light, the incorporation of an additional MIR excitation beam requires a few modifications of the imaging system. Our imaging platform is based on an Olympus Fluoview 300 scan system interfaced with an Olympus IX71 microscope frame. The galvanometric mirrors are aluminum coated, which provides sufficient reflectivity in the 1.0–4.5 μm range. The scan lens is replaced with a CaF_2 lens of similar focal length. Calcium fluoride exhibits excellent transmissive properties in both the NIR and MIR range. Similarly, the tube lens in the IX71 from is replaced by a 180 mm CaF_2 lens. We use a 74x, 0.65 NA reflective objective (5007, Beck), which is a Cassegrain design with a central obscuration. Typical average powers at the sample are 10–40 mW for the ω_p and ω_S beams and 1-5 mW for the ω_{IR} beam.

Because all of the signals in the triple-modal vibrational microscope are in the visible/NIR range, standard refractive optics can be used to relay the radiation to the detection channels. The signal is collected in the forward propagating direction with an achromatic/aplanatic

condenser lens with oil immersion (Olympus), which features an adjustable detection numerical aperture (max. NA = 1.40). The signal is split with a dichroic mirror into two detection channels, each equipped with switchable bandpass filters (Semrock). It is also possible to capture the signal in the epi-direction [90], however, for the experiments reported in this contribution all signals are collected in the forward direction.

4.2.3 Signal detection

We employ two photomultiplier tube (PMT) detection channels. One channel uses a Hamamatsu 7422-40 (blue-sensitive) detector, and the other channel uses a 7422-50 (red-sensitive) detector. Both PMTs are equipped with a Thorlabs TIA60 preamplifier. A single photon counting scheme is used to reduce background noise. For this purpose, the electron bursts are passed through a discriminator (F-100T, Advanced Research Instruments), which converts detection events into TTL pulses. The TTL pulses are conditioned with a waveform generator (AFG3102, Tektronix) for optimum registration and integrated by the Fluoview acquisition card.

The red-sensitive PMT is used for detecting SFG or CARS, while the blue sensitive PMT is utilized for detecting the SHG or TSFG signals. Note that the SFG and CARS signals arrive at the same wavelength and cannot be discriminated with bandpass filters. Therefore, the SFG and CARS signals are detected consecutively. SFG images are obtained when the ω_s beam is blocked, while CARS images are acquired when the ω_i beam is blocked.

4.3 Imaging properties

4.3.1 Spatial resolution

One of the defining features of the nonlinear vibrational microscope is its ability to visualize structures at high spatial resolution. The spatial resolution is primarily determined by the properties of the microscope objective lens. The Schwarzschild-type Cassegrain objective used here has a nominal NA of 0.65, allowing sub-μm lateral resolution while offering a relatively low axial resolution (> 10 μm) [66, 83]. We have characterized the lateral resolution with 0.3 μm barium titanate ($BaTiO_3$) nanoparticles for the different modalities supported by the imaging platform. $BaTiO_3$ particles are used because they exhibit a strong and nonvanishing $\chi^{(2)}$, while also featuring a $\chi^{(3)}$ of sufficient magnitude to visualize single particles.

Figure 4.3(a) shows the SHG (blue) and CARS (red) signal obtained when scanning the focal spot across an individual particle. The FWHM of the profile is 0.55 μm for SHG and for 0.44 μm CARS, which is a representative measure for the resolution attainable in the microscope. The tighter focal spot for CARS is expected because of the higher nonlinearity of the process. The corresponding SFG and TSFG profiles are depicted in Figure 4.3(b). We find a FWHM of 0.66 μm for SFG and 0.45 μm for TSFG. Note that even though the vibrational resonance is driven with light in the MIR, here for wavelengths in the 3–4 μm range, the lateral resolution in both SFG and TSFG is well below a μm. Compared to FTIR microscopy techniques, the up-conversion step in SFG and TSFG permits IR-based vibrational imaging at essentially sub-diffraction limited resolution.

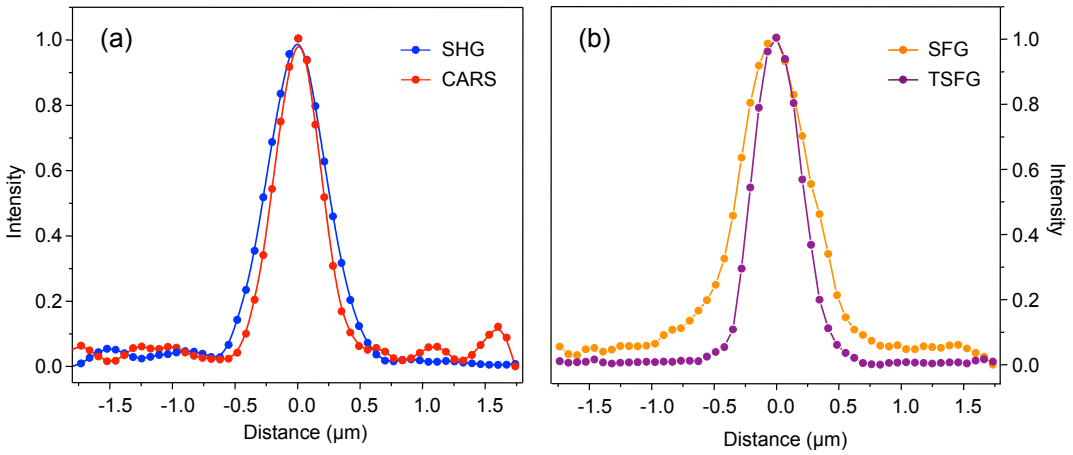

Figure 4.3: Lateral pointspread function measurements with $BaTiO_3$ nanoparticles. (a) SHG and CARS, (b) SFG and TSFG.

4.3.2 Spectral dependence

The spectral dependence of the CARS and SFG techniques has been discussed extensively in the literature [18, 100, 18, 116]. Therefore, we will focus mainly on the spectral dependence of the TSFG signal, which has not been reported before. In Figure 4.4, we compare the CARS image of droplets of immersion oil in D_2O with the corresponding TSFG image. When the $\omega_p - \omega_S$ frequency is tuned to 2845 cm^{-1}, the symmetric stretching mode of the methylene group, the droplets are clearly visible in the CARS image displayed in Fig. 4.4(a). While the resonant contribution of the methylene mode is strong, the nonresonant background signal from D_2O is very weak, producing an image with high contrast. Tuning to 3005 cm^{-1}, off-resonance with the methylene mode, produces much a lower signal and an image with characteristically inverted contrast due to destructive interference with the nonresonant background. The internal structure of the oil in panel (a) can possibly be ascribed to interferences between the two coverslips between which the droplets are sandwiched. Nonetheless, this accidental image feature helps to point out differences between the CARS and the TSFG channel, which is why we choose to display it here.

The corresponding TSFG image taken at 2845 cm^{-1} is shown in Fig. 4.4(c). Although

weaker as in CARS, the signal from the droplets is well above the background signal from D_2O. When tuning to the 3005 cm^{-1} vibrational energy, the signal is substantially weaker, although the signal of the oil droplets remains above the background signal. These images show that TSFG, like CARS, enables vibrational imaging of isotropic materials like liquid oil. Whereas CARS visualizes the oil through a Raman process, TSFG probes the material through a dipole-allowed transition. In both cases, the image contrast arises because of the selective driving of the methylene vibrational mode.

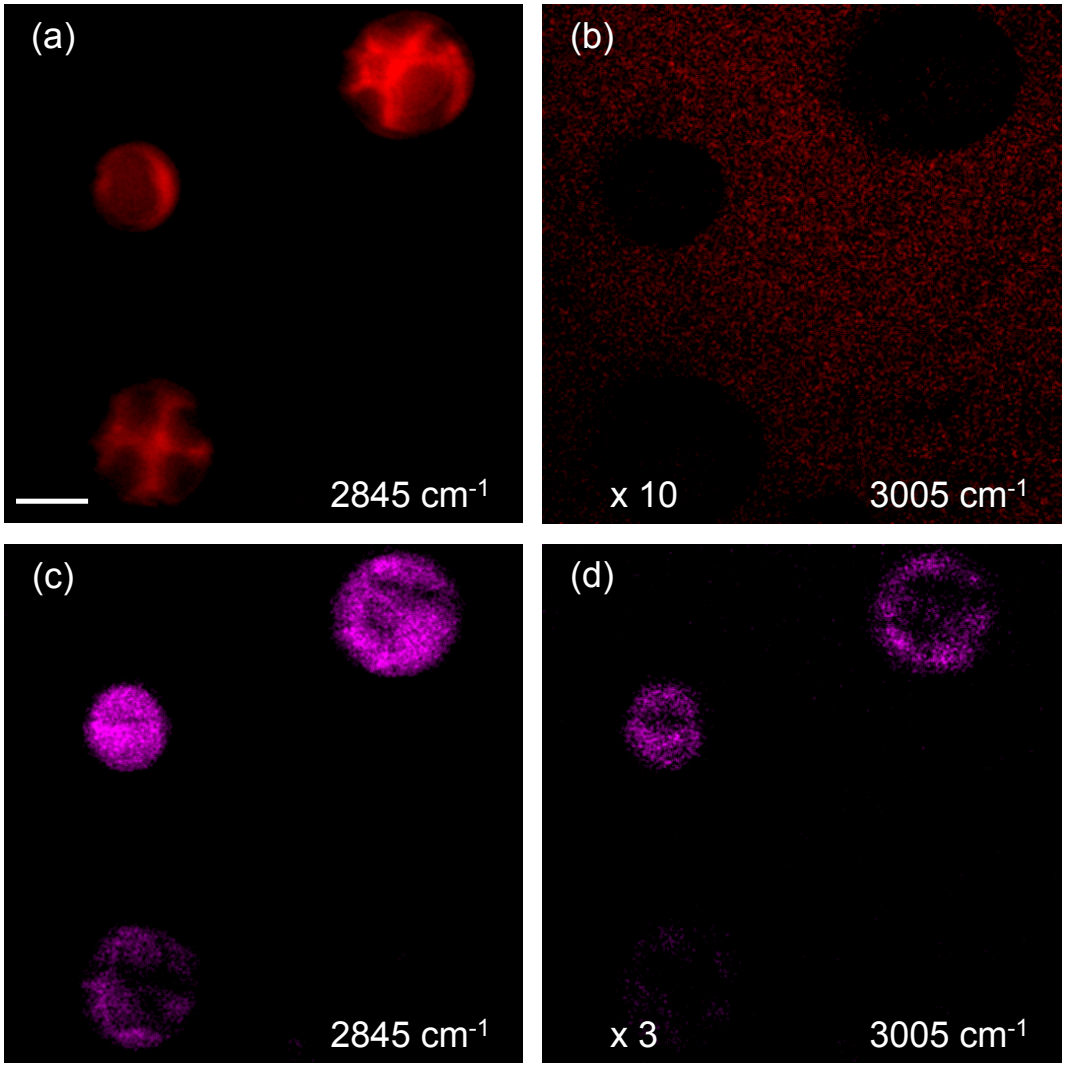

Figure 4.4: Vibrational imaging of immersion oil droplets in D_2O. (a) CARS at 2845 cm^{-1}, (b) CARS at 3005 cm^{-1} multiplied by 10 times relative to the signal at 2845 cm^{-1}, (c) TSFG at 2845 cm^{-1}, (d) TSFG at 3005 cm^{-1} multiplied by 3 times relative to the signal at 2845 cm^{-1}. Scale bar is 10 μm.

The spectral dependence of the CARS and TSFG signals from the immersion oil is shown in Figure 4.5. The CARS signal shows a band profile that is characteristic for CARS spectra of aliphatic molecules. The peak at 2845 cm^{-1} is attributed to the aforementioned methylene symmetric stretching mode. The signal dips near 2980 cm^{-1} are due to interference with the nonresonant background. The TSFG spectrum also shows a maximum and a minimum in this range, but the overall shape is different. First, the offset of the signal at lower energies, due to the nonresonant background, is significantly higher compared to CARS. Second, due to a higher contribution of the nonresonant signal, the bandshape is more dispersive. The maximum of the TSFG signal, also assigned to the methylene symmetric stretch, is red-shifted relative to the CARS spectrum. These observations indicate that for the oil sample studied here, the $\chi_r^{(3)}/\chi_{nr}^{(3)}$ ratio for TSFG is lower than for CARS. Note that the dispersive lineshape is a direct consequence of the coherent character of the TSFG signal.

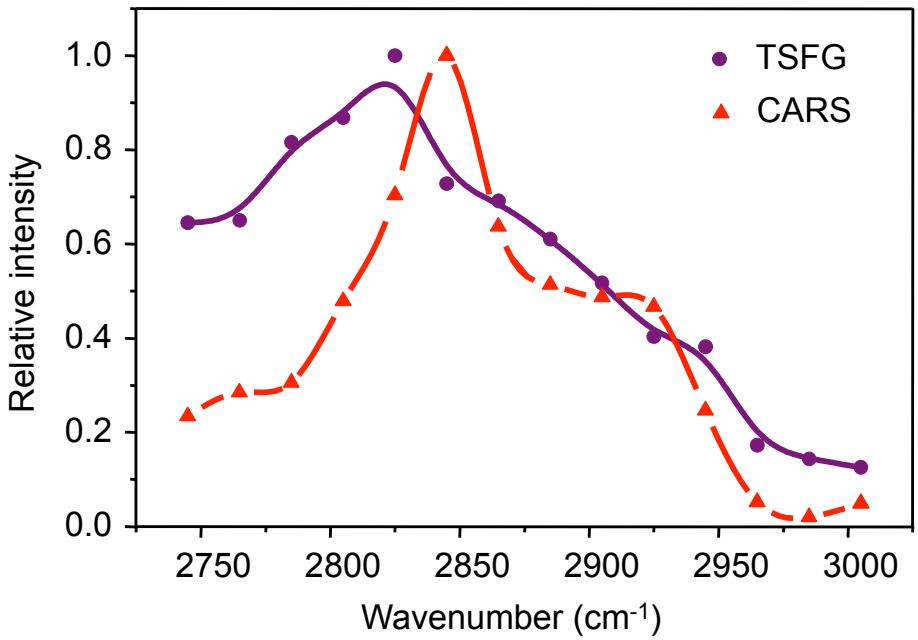

Figure 4.5: Spectral dependence of the CARS (red triangles) and TSFG (purple dots) signal obtained from the immersion oil droplets shown in Figure 4.4. Solid lines are a guide for the eye.

It is interesting to compare the TSFG signal from aliphatic compounds with the THG signal from lipid droplets. In THG imaging it is known that the $\chi_{nr}^{(3)}(-3\omega;\omega,\omega,\omega)$ of lipids is

significantly higher than the $\chi^{(3)}_{nr}$ of the surrounding aqueous medium [24]. The difference in the nonresonant response makes it possible to visualize lipid droplets in THG. In TSFG, we also find a relatively high $\chi^{(3)}_{nr}(-2\omega_p - \omega_{IR}; \omega_{IR}, \omega_p, \omega_p)$ from the aliphatic material versus the aqueous medium. In addition, TSFG exhibits a vibrationally resonant contribution, which is absent in nonresonant THG. The $\chi^{(3)}_r$ contribution is sufficient to generate images with clear vibrational contrast, as is evident from Figure 4.4.

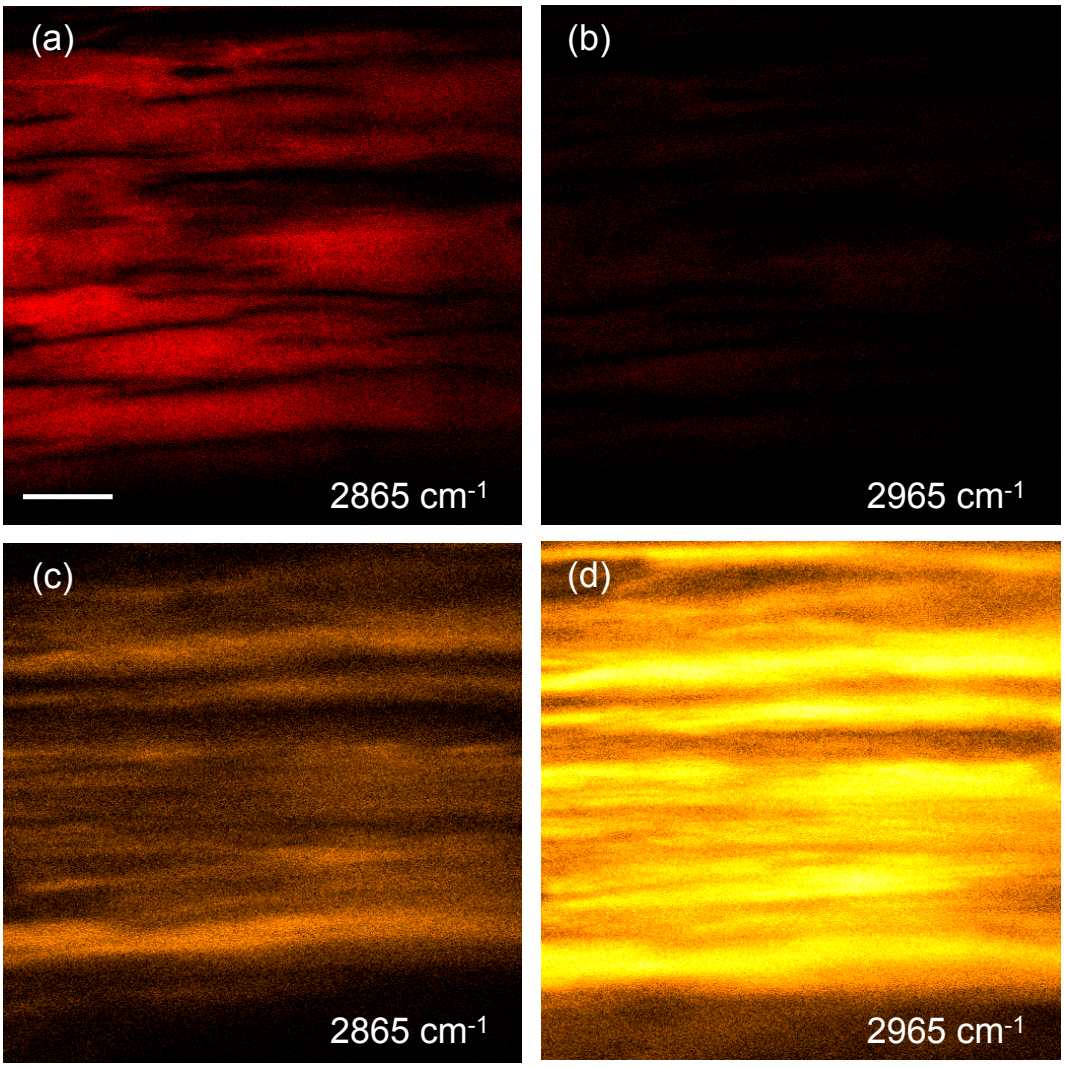

Figure 4.6: Vibrational imaging of rat tail tendon. (a) CARS at 2865 cm^{-1}, (b) CARS at 2965 cm^{-1}, (c) SFG at 2865 cm^{-1}, (d) SFG at 2965 cm^{-1}. Scale bar is 10 μm.

Figure 4.6 compares the CARS and SFG images of rat tail tendon. This tissue is rich in aligned collagen I fibers. The noncentrosymmetry of the collagen I fibrils gives rise to a

strong SFG signal. Panels 4.6(a) and (c) show the CARS and SFG images, respectively, when tuning to a vibrational energy of 2865 cm^{-1}. Note that the spatial features of the fibrous tissue appear differently in these modalities. Whereas CARS is sensitive to the bulk architecture of the tissue, the SFG images shows more refined fibrous details. Similar to SHG imaging, SFG is sensitive to the polar alignment of fiber domains, introducing $\chi^{(2)}$-specific image features related to average polar alignment of the collagen moieties [38, 21]. The latter features are not observed in the CARS image.

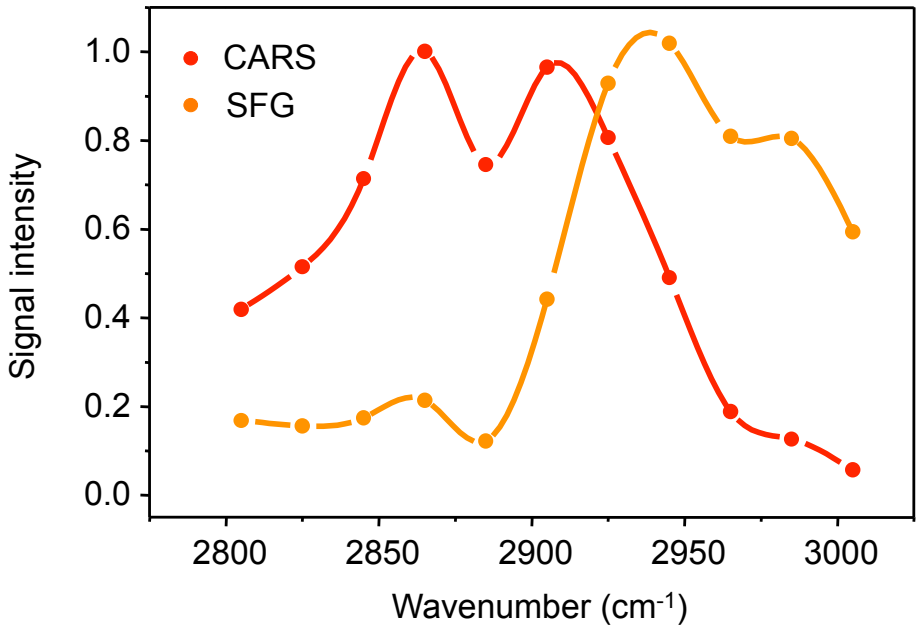

Figure 4.7: Spectral dependence of the CARS (red dots) and SFG (orange dots) signal obtained from the rat tail tendon images shown in Figure 4.6. Solid lines are a guide for the eye.

Panels 4.6(b) and (d) show the corresponding CARS and SFG images when tuning to 2965 cm^{-1}. While the CARS signal has diminished at this vibrational energy, the SFG signal has increased. Collagen I is rich in methylene groups and has a relatively low density of methyl groups, underlining that the vibrational spectrum in the CH-stretching range is dominated mostly by methylene modes. Yet, the CARS and SFG spectral response of the sample is markedly different. The differences are exemplified in Figure 4.7, which shows the CARS and SFG spectra extracted from a hyperspectral data stack. The CARS spectrum shows two

maxima in this range, previously attributed to the symmetric and asymmetric CH_2 stretching modes [119]. The SFG spectrum exhibits a remarkably different profile, with a maximum near 2950 cm^{-1}. Although the origin of this peak is not entirely clear, it has been proposed before that a Fermi-resonance between the CH_2 stretching and bending overtone might be responsible for this signature [95]. The comparison between the CARS and SFG spectrum thus reveals that the two different modalities illuminate very different spectroscopic details of the sample, providing complementary information about content and structure.

4.3.3 Image features

The Cassegrain objective lens exhibits a central obscuration, resulting in annular illumination with an extended focal range. The focal distribution shares similarities with a Bessel beam, which also features an extended axial focal profile. Despite these focal properties, the nonlinear optical processes discussed here all produce detectable signals, captured by the high NA condenser lens. The CARS signal yields contrast similar to what is observed under tight focusing with a high NA refractive objective [6], indicating that the phase-matching conditions for CARS are not significantly altered by the use of the reflective lens. Previous work has also shown that SHG from non-centrosymmetric materials such as collagen fibers, obtained with a reflective objective, appear with image features that are comparable to SHG signals generated by refractive objectives. Similarly, the detectable SFG and TSFG signals from bulk materials suggest that the coherent radiation appears at phase-matching angles that are within the cone angle of the 1.4 NA condenser lens.

As shown in Fig. 4.4, TSFG is obtained from the bulk oil medium. No particular highlighting of D_2O/oil interfaces is observed. These imaging properties are notably different from what is commonly seen in THG microscopy with high NA refractive lenses, where bulk signals are not allowed because of the Gouy phase-mismatch. The detected TSFG response from

the bulk suggests that a similar Gouy phase-mismatch is not suppressing the signal in the detection direction. As discussed in Section 4.1.4, the Gouy phase mismatch in vibrationally-sensitive TSFG is relaxed relative to THG because of the longer wavelength of one of the light-matter interactions. Also, in the case of perfect Bessel beams, it is known that phase matching for THG can be achieved at an off-axis angle in bulk materials [23, 112]. This latter mechanism may partially contribute to the detectable bulk signals encountered in the current TSFG imaging experiments.

Compared to the CARS and SFG signals, the TSFG signal is about 5 times weaker under resonant conditions. Yet, the TSFG signal clearly stands out against other spurious signals. We do not observe a strong multi-photon fluorescence signal in the TSFG channel, as the signal disappears when the detection bandpass spectral window is red-shifted by 50 nm to exclude the 449 nm TSFG signal wavelength. Since fluorescence emission is typically broadband, a substantial portion of the signal would be expected at the detector upon red-shifting the detection window, if the origin of the signal were fluorescence. The signal in the TSFG channel also disappears if either one of the ω_p and ω_{IR} beams is blocked or when the two pulse trains are temporally offset beyond the width of the pulses (5 ps).

4.4 IR-induced effects on CARS

The addition of a MIR beam to the NLO laser-scanning microscope not only enables the implementation of the vibrationally-sensitive SFG and TSFG modules, but also offers an opportunity to study other MIR-induced effects. One such effect is shown in Figure 4.8, where the CARS signal from immersion oil is studied while the sample is illuminated by the additional MIR-beam. We observe that the on-resonance CARS signal decreases for higher average power of the MIR-beam, both for the immersion oil and a sample of olive oil. When the MIR beam is tuned to 2910 cm^{-1}, away from the dominant symmetric methylene

vibration, the depletion of the CARS signal is significantly less.

These observations indicate that a vibrational-selective excitation by the MIR beam alters the magnitude of the CARS signal. A possible explanation is the change in the refractive properties of the material after vibrational heating of the sample, which changes the focusing properties in the medium and can thus affect the amount of signal intercepted by the condenser lens. Such a process is reminiscent of the mechanism behind photothermal MIR imaging, which uses the refractive changes experienced by a vis/NIR probe beam due to the MIR excitation of the material [65, 126]. In the present case, the heating induced by the MIR excitation would defocus the anti-Stokes radiation and reduce the amount of signal captured by the collimating lens. However, we find that changing the NA of the condenser in the 0.7–1.4 NA range does not dramatically alter the depletion trend shown in Fig. 4.8.

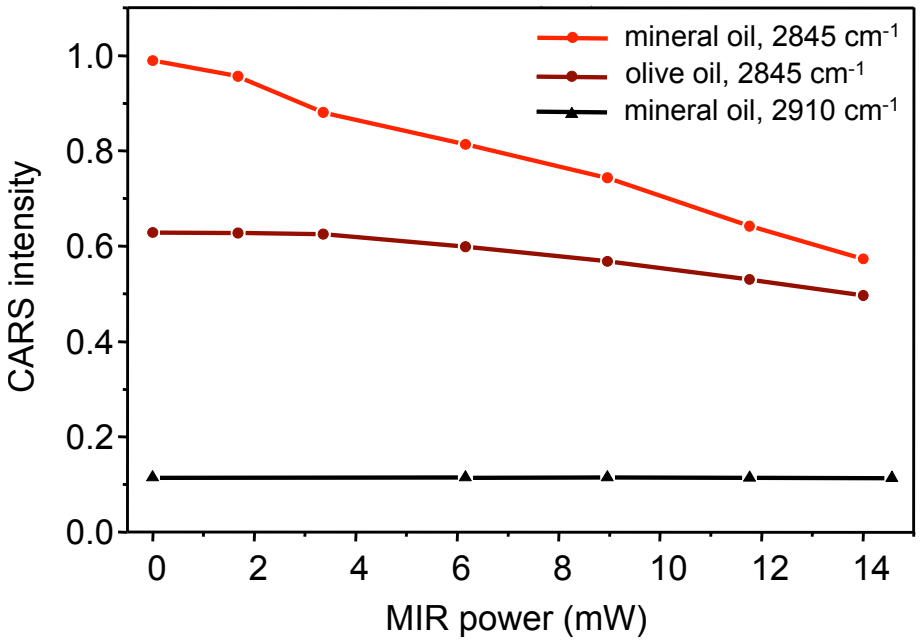

Figure 4.8: CARS intensity as a function of average power of focused MIR radiation. Average power is measured at the sample location.

Ground state depletion is an alternative mechanism that could lead to a decrease of the CARS signal. By transferring population from the ground state to the vibrationally excited state, the ground state population becomes depleted and the regular parametric CARS pathway is

blocked. The latter process can be useful in potential super-resolution techniques [5, 20]. In either case, the IR-beam offers a mechanism for controlling the amount of detected CARS signal, which could have interesting future applications.

4.5 Triple-modal vibrational imaging

The examples shown in Figures 4.4 and 4.6 highlight some of the capabilities of the triple-modal vibrational microscope. Another example is given in Figure 4.9 where a cellulose granule is visualized with CARS, SFG, TSFG and SHG. Since cellulose has a non-vanishing $\chi^{(2)}$, it is suitable for detailed investigations using all four imaging modalities. Cellulose has been studied rather extensively with CARS and SHG microscopy [131, 101, 86], but the example shown here underlines that high resolution images can be obtained with the SFG and TSFG modalities as well. This capability is useful for an in-depth analysis of microdomains, which is relevant for understanding the spatial heterogeneity of cellulose hydrolysis kinetics. In particular, SFG spectroscopic contrast provides a wealth of information about chain orientation and packing density [63, 62, 60].

4.6 Prospects and challenges

In this contribution, we discussed an imaging platform that integrates three vibrationally sensitive imaging modalities, namely CARS, SFG and TSFG. Whereas CARS probes Raman-active modes, TSFG is sensitive to IR-active modes. In addition, the SFG modality enables spectroscopic studies of non-centrosymmetric materials. The combination of these three modalities allows for a complete vibrational spectroscopic assessment of the sample. All imaging techniques offer sub-μm lateral resolution, which, for the IR-based modalities, represents an effective sub-diffraction limited resolution compared to IR-absorption microscopy.

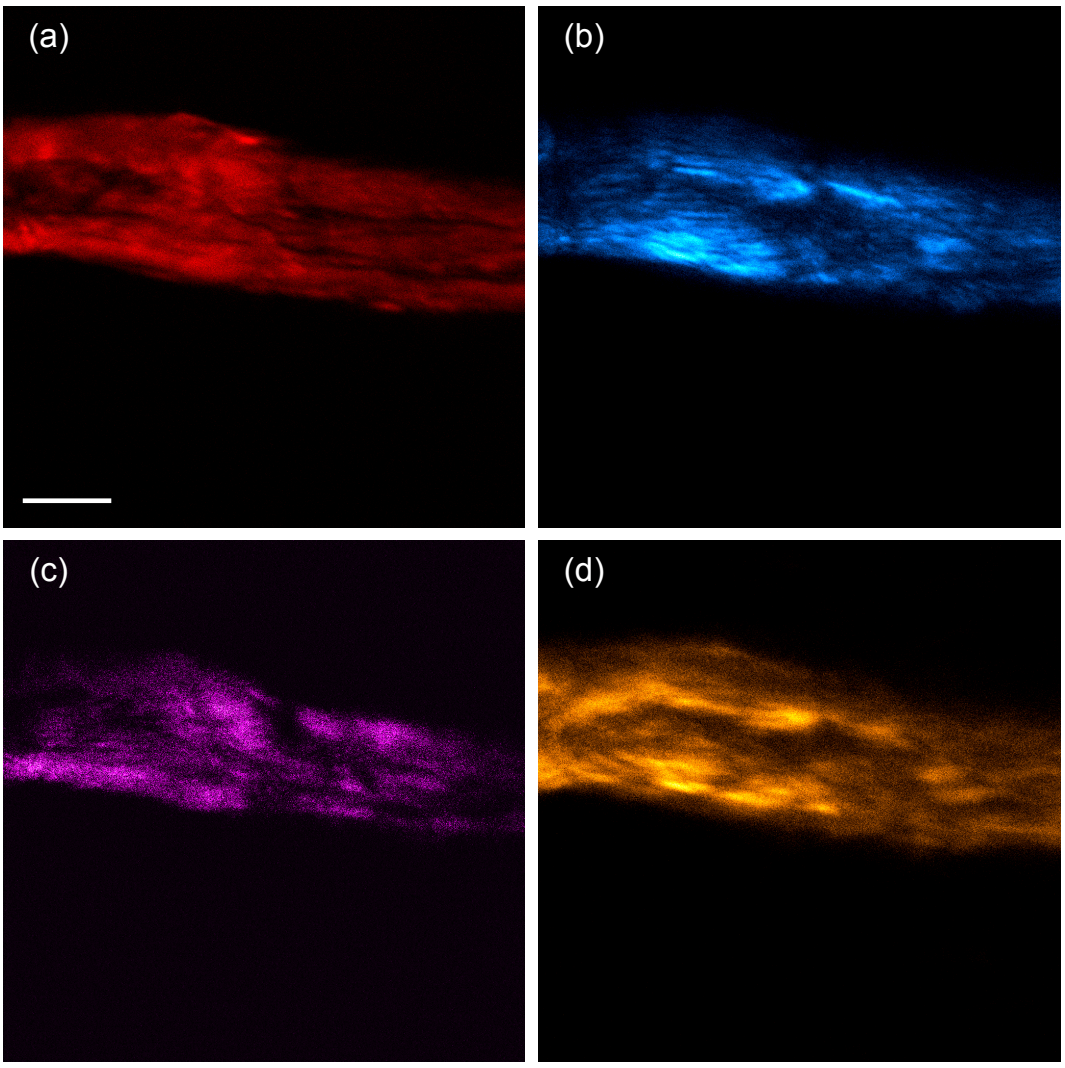

Figure 4.9: Multi-modal vibrational imaging of a cellulose granule. (a) CARS at 2845 cm^{-1}, (b) SHG, (c) TSFG at 2845 cm^{-1}, and (d) SFG at 2845 cm^{-1}. Scale bar is 10 μm.

Among the available coherent vibrational techniques, the TSFG modality has not been previously demonstrated. The images presented in this work underline that TSFG signals are at detectable levels that are suitable for laser scanning microscopy applications, at least for organic materials examined in the CH-stretching range of the spectrum. We have shown that the TSFG signal is vibrationally sensitive, but that the $\chi_r^{(3)}/\chi_{nr}^{(3)}$ ratio is lower than for CARS. In this context it is relevant to emphasize that the resonant response of the IR-active CH stretching modes is much weaker than the response of various modes in the fingerprint region (1000–1800 cm^{-1}). For instance, the Amide I mode exhibits an absorption

cross section that is about an order of magnitude higher than the corresponding response of the CH-stretching modes, implying that $\chi_r^{(3)}$ for the Amide I mode is significantly higher. Since TSFG scales as $|\chi_r^{(3)}|^2$, the TSFG signals in the fingerprint range are expected to be substantial. In addition, the dispersive character of TSFG in this range is expected to be reduced. Therefore, TSFG imaging may be particularly useful for mapping modes in the fingerprint range. Although our current lightsource is not suitable for generating ω_{IR} in this region, future efforts will focus on pushing TSFG microscopy to the 1000–1800 cm^{-1} vibrational range.

One of the merits of TSFG is that it offers a nonlinear alternative to conventional IR microscopy. Although it is sensitive to the same vibrational modes as probed in FTIR microscopy, the signal is detected in the visible range of the spectrum, thus greatly simplifying the detection strategy. In addition, the lateral resolution is beyond the IR-diffraction limit, allowing the generation of images with IR contrast with $\sim$ 0.5 μm resolution. This resolution is predominantly determined by the two-photon upconversion process rather than by the ω_{IR} interaction. Consequently, the high resolution can be maintained independent of the λ_{IR} wavelength. In this regard, the TSFG shares similarities with photothermal IR imaging techniques. [68, 126] A potential advantage of TSFG imaging over photothermal approaches is that no modulation scheme is required and that the spatial resolution is not directly linked to heat diffusion. Because TSFG relies on optically driven vibrational coherences, it is not directly sensitive to photothermal populations, implying that the imaging resolution is expected to be independent of material or position in the sample.

The combination of different vibrational NLO techniques on a single platform is helpful for a deeper spectroscopic assessments of samples. For instance, it can be challenging to analyze biomolecular microcrystals in complex media when the exact chemical composition is unknown. Since many biomolecules form non-centrosymmetric crystals, they can be assessed by SFG in addition to CARS and TSFG microscopy. The ability to selectively sample IR

and Raman-active modes, as offered through TSFG and CARS, respectively, can help determine the spectroscopic mode symmetries and thus information about chemical content and molecular orientation. The SFG information, aided by polarization-sensitive measurements, can furthermore provide information about structure and orientation that complement the bulk-sensitive TSFG and CARS measurements. Potential examples include the study of microcrystallites in atherosclerotic lesions [109], microdomains in cellulose [131, 101, 86], and nucleation of polypeptide crystals [41].

However, the triple-modal vibrational microscope is not without its limitations. Because it combines NIR with MIR incident beams, optical elements are needed that are non-standard on regular laser-scanning microscopes. The large spectral gap between the NIR and MIR excitation beams implies that optical components need to be chosen that operate over a broad wavelength range. This requirement holds not only for sample substrates, but also for lenses and relay optics. Although all-reflective imaging systems represent a broadband and achromatic solution [2, 129], such optical components are not easily integrated into conventional laser scanning microscopes. Broadband refractive components, such as the CaF_2 lenses used here, retain the original design of the laser-scanning microscope while expanding its transmission range into the MIR. Nonetheless, singlet optical elements such as CaF_2 lenses introduce chromatic aberrations, which ultimately limit the image quality. In this regard, the development of achromatic broadband lenses would significantly impact the practical implementation of the NLO multimodal vibrational microscope.

Another limitation is the elongated focal volume associated with the use of a Cassegrain reflective lens. The extended axial focal range deteriorates the axial resolution and reduces the sensitivity of the microscope to sub-μm structures. Alternative reflective lens designs, which produce focal volumes that exhibit a higher degree of 3D confinement, would be welcome. Although the design criteria are rather challenging, refractive objective lenses capable of achromatically focusing light in the 1–4.5 μm range to a tight spot are also

desirable. Developments in this area are sure to improve the utility of the triple-modal vibrational microscope.

4.7 Conclusion

In this contribution, we introduced the principle of triple-modal vibrational imaging with contrast generated by CARS, SFG and TSFG. The spectral properties of these modalities complement each other, enabling a more complete spectroscopic assessment of the sample at the sub-μm scale. The implementation discussed in this work emphasizes the feasibility of multi-modal vibrational contrast, including the practicality of TSFG microscopy, a new technique that provides images based on the excitation of IR-active vibrational modes. We expect that with further improvements of broadband optical elements, the use of IR-based vibrational technologies will grow in importance in laser-scanning NLO microscopy of biological materials.

Chapter 5

High Resolution Infrared Imaging of Biological Sampels with TSFG

5.1 Introduction

The mid-infrared (MIR) wavelength range roughly stretches from 3 to 10 μm, and covers the energy range of many fundamental molecular vibrations. The absorption of MIR radiation by molecular vibrational modes forms the basis of the contrast seen in IR spectroscopy and microscopy. In Fourier transform IR (FTIR) microscopy, the absorption signatures are recorded as a function of position in the sample, producing a chemical map without the need for sample labeling. This capability is of tremendous relevance to biomedical imaging, and many efforts have shown that FTIR microscopy holds promise as a label-free imaging method for tissue inspection.[120, 45, 7, 42, 124]

Recent developments have further underlined the potential of IR absorption contrast for mapping biological and biomedical samples. The availability of focal plane arrays (FPA) have made the detection of IR images practical, accelerating developments in IR microscopy.[45]

In addition, the use of quantum cascade lasers (QCL) have enabled imaging with a much brighter lightsource, while also changing the spectral acquisition mode from broadband interferometry to discrete frequency mapping.[87, 55, 7] Furthermore, by optimizing the pixel size on the detector for the wavelength dependent pointspread function, IR images can be recorded with high definition, which improves image quality and contrast.[92] These combined advances have increased the utility of MIR spectroscopic imaging for tissue diagnostics and pathology.[124]

Despite these advances, several fundamental limitations of MIR-based microscopy remain. For instance, although FPA technology makes IR imaging possible, the detection efficiencies and costs do not compare well with detection technologies in the visible range of the spectrum, ultimately limiting the routine use of the IR microscopy technique. Another limitation is the relatively low spatial resolution. The diffraction-limited resolution is dictated by the wavelength of light, corresponding to a practical point spread function in the 4 to 7 μm range for the fingerprint vibrational bands. Although individual cells can be examined[79, 27], the intracellular structures are typically not resolved in MIR microspectroscopic imaging because of the limited resolution. The low resolution affects the diagnostic capabilities of the MIR approach to imaging. Additionally, since MIR radiation is strongly absorbed by water over a wide range, microscopic imaging of hydrated tissue samples in this wavelength regime is challenging. For this purpose, most imaging studies are performed on dehydrated samples, thus largely excluding applications that focus on aqueous specimens or live cells and tissues.

Several approaches have been undertaken to tackle some of the issues above. In terms of improving the detection strategy, a handful of methods have been developed that convert the MIR information to a visible signal. For example, the principle of up-conversion of MIR radiation in a nonlinear material has been used for this purpose[51], enabling the detection of IR images with a silicon-based camera.[22, 52] Another technique uses a secondary visible laser beam to probe the MIR-induced photothermal effect in the sample.[65, 126, 70] The

heat induced refractive index changes in the sample affect the beam properties of the visible beam upon traversing the specimen, which can be captured with a visible photodetector. In both approaches, expensive MIR detectors can be avoided and replaced by more efficient and cost effective detectors in the visible/NIR.

Other efforts have focused on improving the spatial resolution of MIR-based imaging. The most commonly used microscope focusing element is a reflective Cassegrain objective, which is commercially available and features numerical apertures (NA) up to ~ 0.7. However, over the past three decades, there has been limited progress in developing reflective objectives with a higher NA. An alternative focusing configuration uses a solid immersion lens (SIL) to improve the NA of the reflective mirrors. For instance, a silicon SIL has been used to improve the MIR imaging resolution by twofold.[58] Yet, the resolution of the imaging system is still determined by the IR-diffraction limit. The spatial resolution in the photothermal MIR imaging technique, on the other hand, is not determined by the diffraction-limited focal volume of the MIR excitation alone, but rather by the overlap volume of the MIR pump and the visible probe. The dimensions of this interaction volume are roughly equal to the diffraction-limited spot size of the tightly focused visible laser beam, thus offering a sub-μm imaging resolution. Recent implementations of the photothermal MIR microscopy technique have reached a lateral resolution in the 0.6 μm range[126, 69], which is about an order of magnitude better than the resolution set by the IR-diffraction limit of the same lens.

The discussion above emphasizes the advantages of a technique like photothermal MIR microscopy. Shifting the probing of the MIR absorption event to the visible range of the spectrum both relaxes the constraints on the photodetector and substantially improves the effective spatial resolution of the imaging system. It is also possible to probe MIR-excited vibrational modes in a fully coherent manner with nonlinear optical (NLO) microscopy. A current example is sum-frequency generation (SFG) microscopy[90], which uses a MIR pump beam to prepare a coherent superposition of the ground state and a vibrationally excited

state. The coherence is subsequently probed with a visible/NIR laser pulse, producing a SFG signal in the visible range of the spectrum. Like photothermal MIR microscopy, SFG benefits from shifting the detection to a visible wavelength. Laser-scanning SFG microscopy offers MIR-sensitive images with 0.6 μm lateral resolution and image acquisition times that are similar to the acquisition times in coherent Raman scattering (CRS) microscopy.[40] Nonetheless, SFG microscopy is a second-order NLO technique that probes materials that exhibit non-centrosymmetry. While SFG is a good method for studying fibrillar collagen[38, 37] or cellulose[80, 48], structures that fulfill the requirement for non-centrosymmetry, it is less useful as a general IR-sensitive imaging technique.

We have recently shown the feasibility to perform third-order SFG (TSFG) measurements in a laser-scanning microscope.[39] In TSFG, the MIR-driven coherence is probed with a two-photon hyper-Raman interaction, producing a coherent signal in the visible part of the spectrum, as shown in Figure 5.1(A). Unlike SFG, which probes the $\chi^{(2)}$ properties of the sample, TSFG is a four-wave mixing technique that is sensitive to the $\chi^{(3)}$ properties of the material. Like CRS methods, TSFG is not limited to certain symmetries of the sample, and can thus be used as a general vibrationally sensitive imaging technique. Whereas CRS techniques are sensitive to Raman-active modes of the sample [17], TSFG is sensitive to IR-active modes. In other words, the TSFG microscope can be regarded as a nonlinear equivalent of the MIR-absorption microscope.

Although the feasibility of measuring TSFG has been demonstrated, it is unclear what the potential of the technique is in the context of biological and biomedical imaging. In this contribution we push TSFG in the direction of biomedical imaging application. In particular, we discuss the resolution and spectral dependence of the signal in the CH-stretching range of the spectrum. We also study the TSFG signal of neutral lipids in aqueous medium and compare the image features with those of coherent anti-Stokes Raman scattering (CARS) images. We furthermore present the first TSFG images of intact biological tissue. These

results indicate that TSFG microscopy holds promise as an IR-sensitive NLO imaging tool for biological and biomedical imaging applications.

5.2 Methods

5.2.1 Light source

The light source consists of a Yb-doped fiber laser (aeroPULSE, NKT Photonics), which produces a 76 MHz pulse train at 1032 nm (ω_p). The pulse width is about 10 ps. The laser output synchronously pumps an optical parametric oscillator (Levante OPO, A.P.E. Berlin). The OPO produces a signal (ω_s) and idler (ω_i) beam through parametric down-conversion of the pump photon ($\omega_p = \omega_s + \omega_i$). The OPO has been modified to accommodate the generation of mid-IR radiation. The linear cavity is resonant with the signal and includes a fanned periodically-poled crystal that allows signal generation in the 1350–2000 nm range, corresponding to 2200–4300 nm for the idler beam (2320–4550 cm^{-1}). At an average pump power of 7.5 W, the power in the signal beam is $\sim$ 1.5 W, while the idler power is $\sim$ 550 mW. All three output beams ($\omega_p, \omega_s, \omega_i$) are attenuated with a half waveplate and a polarizer, and the transverse beam profiles are improved with spatial filters. The ω_p and ω_s beams are delayed with translation stages such that all pulse trains overlap temporally after combining the beams collinearly on custom dichroic mirrors (Layertec, GmbH). A schematic of the beam routing is shown in Figure 5.1(B).

5.2.2 Microscope

The microscope is based on a laser-scanning imaging system (Fluoview 300, Olympus), interfaced with an inverted microscope frame (IX71, Olympus). The scanning mirrors are

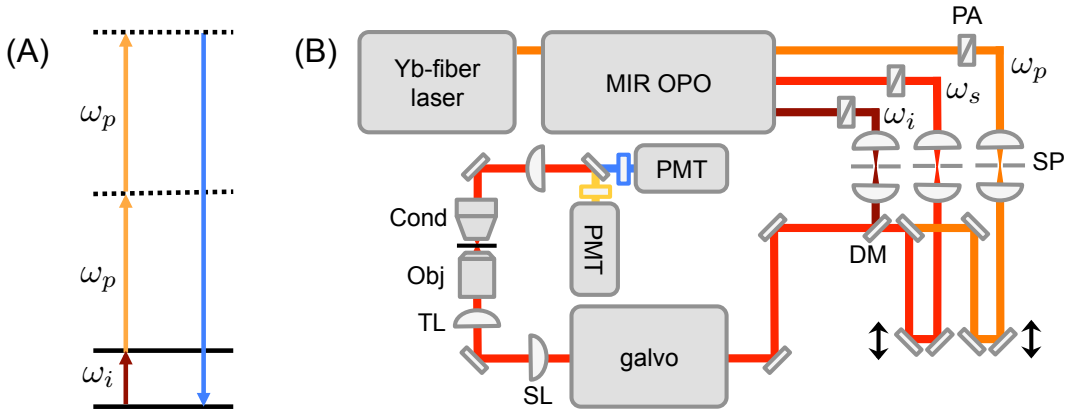

Figure 5.1: (A) Jablonski diagram of the TSFG process. (B) Schematic of the TSFG microscope system. PA: polarization based attenuator; SP: spatial filter; DM: dichroic mirror; SL: CaF_2 scan lens; TL: CaF_2 tube lens; Obj: 0.65 NA reflective objective lens; Cond: 1.4 NA oil immersion condenser; PMT: photomultiplier tube.

aluminum coated, and support all beams used in the experiments reported here. The beams pass a f=50mm CaF_2 scan lens and a f=200mm CaF_2 tube lens before entering a 0.65 NA reflective objective (5007, Beck). For the TSFG experiments, the powers at the sample are 1–10 mW for the idler beam and 10–50 mW for the pump beam. For the CARS experiments, the idler beam is blocked and the signal beam is allowed to pass through the sample at average powers of 1–20 mW. Signals are collected in the forward direction by a 1.4 NA oil immersion condenser. A dichroic mirror splits the signal into two contributions, one isolates the TSFG signal through a 450 ± 10 nm bandpass filter, and the other captures the CARS signal through a 780 ± 20 nm bandpass filter. Both detectors are photomultiplier tubes (7422, Hamamatsu) equipped with pre-amplifiers (TIA60, Thorlabs). Signals are detected in the single photon counting mode, by passing the signals through a discriminator (F-100T, Advanced Research Instruments), which converts each counting event into a TTL pulse. The TTL pulses are subsequently stretched in time by a waveform generator (AFG3102, Tektronix) to optimize the integration of the signal directly on the ADC card. The pixel dwell time is 1 μs. To improve image contrast, frame averaging is used with up to 60 averages, giving rise to a maximum acquisition time of about a minute per averaged image.

5.2.3 Sample preparation

The D_2O used in the experiment is purchased from Sigma-Aldrich. A droplet of Olympus immersion oil is used as the mineral oil sample. Barium titanate ($BaTiO_3$) nanoparticles of diameter < 0.1 μm are obtained from Sigma-Aldrich. Tissue samples are derived from adult mouse adipose tissue and eyelid skin. Excised skin was embedded in OCT medium and cut to slices of either 10 or 25 μm thickness. Sectioned tissue was rinsed with room temperature saline buffer (either H_2O or D_2O based) to remove OCT medium, and placed on a standard microscope glass slide. A borosilicate coverslip was placed on the immersed tissue and the sample was sealed with epoxy adhesive to prevent dehydration of the specimen. On some slides, droplets of neutral lipid were present and they formed during the cutting process. The droplets were used in the some of the experiments as representative neutral lipids for characterizing the TSFG signal.

5.3 Results

5.3.1 Observation and characteristics of the TSFG signal

With the ω_i beam tuned to 2820 cm^{-1}, the TSFG signal at $2\omega_p + \omega_i$ is expected at 446 nm. Using a droplet of mineral oil on a glass coverslip as the sample, we indeed observe a signal in the TSFG channel when the ω_i and ω_p beams are overlapped in time. Interestingly, we also observe a signal near 652 nm, which we attribute to the TSFG signal at $2\omega_i + \omega_p$. Both signals observed from the oil droplet show a spectral dependence when the ω_i beam is tuned, indicating that both TSFG signals probe the molecular vibrational resonance. Nonetheless, because the average power of the MIR beam is purposely tuned much lower than the average power of the pump beam, the signal at $2\omega_p + \omega_i$ is significantly stronger that the signal

at $2\omega_i + \omega_p$. For this reason, the TSFG signals are detected in the wavelength range near 445–450 nm. The inset in Figure 5.2(A) shows the dependence of the $2\omega_p + \omega_i$ TSFG signal on the average power of the ω_i and ω_p beams. A linear and quadratic fit confirm that the TSFG signal scales linearly with the ω_i beam and quadratically with the ω_p beam.

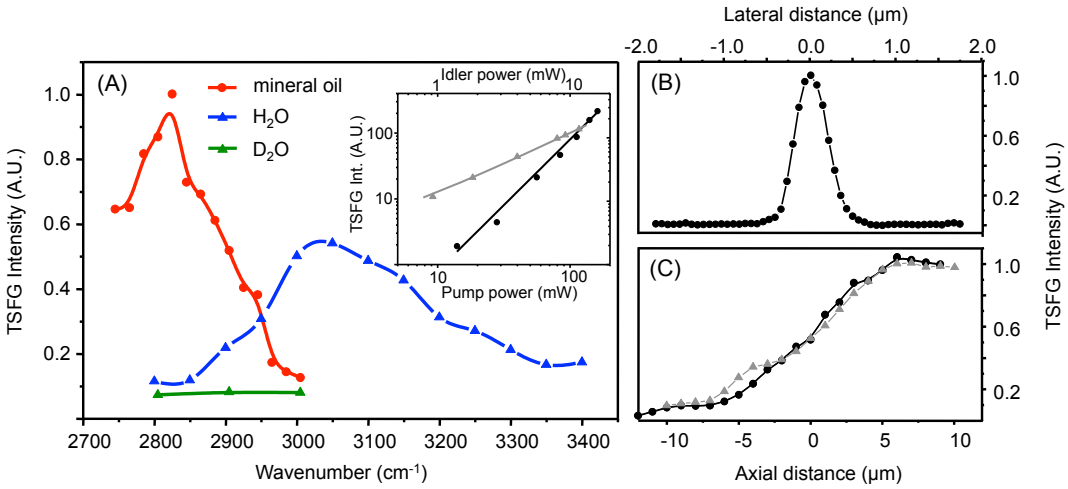

Figure 5.2: (A) Spectral dependence of the TSFG signal of mineral oil (circles, red), H_2O (triangles, blue) and D_2O (triangles, green). The spectral profiles are normalized to the peak of the mineral oil spectrum. The solid lines are a guide for the eye. The inset shows the power dependence of the idler beam (triangles, gray) and the pump beam (circles, black). The solid lines are a linear fit (gray, slope = 1.0) and a quadratic fit (black, slope = 2.0). (B) Lateral dependence of the TSFG signal when scanning a 0.1 μm $BaTiO_3$ particle through focus. (C) Axial dependence of the TSFG signal (circles, black) and the CARS signal (triangles, gray) when scanning a glass/oil interface through focus.

Figure 5.2(A) also depicts the spectral dependence of the TSFG signal observed from the mineral oil droplet (red circles). The signal peaks near 2820 cm^{-1} and dips near 3000 cm^{-1}. The spectral profile does not directly mimic the IR absorption profile of the oil, but rather shows a dispersive lineshape. Similar to CARS spectral lineshapes[17], the interference between resonant and nonresonant $\chi^{(3)}$ contributions produces a dispersive profile.[39] The maximum TSFG signal from the oil samples in this range appears at 2820 cm^{-1}. The TSFG signal observed from a droplet of water is shown by the blue triangles. Near 2820 cm^{-1} the signal from water is significantly less than that from mineral oil, enabling imaging of concentrated aliphatic compounds without interference from a strong water signal, but near 3000 cm^{-1} the water signal has increased and is stronger than the signal from oil. Beyond

3050 cm^{-1}, we observe a decrease of the water signal when the vibrational frequency is increased. Again, the maximum TSFG signal appears significantly red-shifted from the maximum IR absorption in this range ($\sim$ 3400 cm^{-1}). A similar observation has been made for the CARS spectrum of water [15], and is due to the interference of resonant and nonresonant components. Note that the signal from D_2O (green triangles) is relatively constant in the CH-stretching range (2800–3000 cm^{-1}), due to the absence of O-H resonances. As expected, we observe an increase in the TSFG signal from D_2O when ω_i is tuned to $\sim$2550 cm^{-1}, which is closer to the O-D resonances.

A measure of the lateral spatial resolution is given in Figure 5.2(B), which shows the dependence of the TSFG signal when scanning a 0.1 μm $BaTiO_3$ particle through focus. The full-width half maximum (FWHM) of the resulting profile is 0.45 μm, corresponding to a resolution that is significantly higher than the resolution defined by the IR-diffraction limit. A measure for the axial resolution can be obtained by scanning an oil/glass interface axially through focus at 2820 cm^{-1}. The results of such a step-edge scan are shown in Figure 5.2(C). We observe that the transition from the nonresonant glass signal to the resonant oil signal occurs in about 10 μm. A similar dependence is observed for the CARS signal, underlining the comparable performance of the two techniques. Among other factors, the axial resolution is largely dictated by the microscope objective. An elongated focal volume in the axial dimension is characteristic for laser beams focused by reflective Cassegrain objectives. Although the axial resolution is much less than what is common for NLO microscopes that use high NA refractive objective lenses, the probing volume is truly three dimensional because of the two-photon probing interaction with ω_p. We note that unlike TSFG, regular IR-based microscopes do not exhibit an intrinsic 3D resolution.

5.3.2 Image features of TSFG microscopy

Figure 5.3(A) shows a TSFG image of lipid droplets immersed in water. The neutral lipids are obtained from adult mouse white adipose tissue and thus represent a relevant tissue component. The droplets are clearly observed in the image at 2820 cm^{-1}, whereas the TSFG signal from water is significantly less at this vibrational frequency. When the MIR frequency is tuned to 3005 cm^{-1}, shown in Figure 5.3(B), the signal from the droplets drops significantly while the water signal has increased. The droplets now appear with negative contrast relative to an elevated signal from the surrounding medium.

The corresponding CARS images are shown in panels 5.3(C) and 5.3(D). There is a striking resemblance between the TSFG and CARS images. In both cases the signal shows a clear positive signal when tuned near the symmetric CH_2 stretching mode, and inverted contrast when tuned off-resonance at 3005 cm^{-1}. This resemblance underlines the similarities between TSFG and CARS, as both signals are coherent, carry vibrationally resonant and nonresonant contributions, and scale as $|\chi^{(3)}|^2$. The main difference between the techniques is that TSFG drives IR-active vibrational modes whereas CARS drives Raman-active modes. Note that some of the subtle differences between the image features in the TSFG and CARS images can be attributed to the slight difference between the axial position where the TSFG and CARS signals are maximized. Under the current imaging conditions, the TSFG signal is weaker than the CARS signal. This is reflected in the signal-to-noise ratio (SNR) extracted from the resonant signals of the images shown in Figure 5.3. The SNR for TSFG is ~ 6 while the SNR for CARS is twice as high.

Because TSFG is also closely related to third-harmonic generation (THG), it is perhaps surprising that the TSFG signal from the bulk inside the droplets is strong and that the interface between the droplet and the aqueous medium is not significantly highlighted. In THG imaging, the Gouy phase shift mismatch between the incident field ω and the signal

field 3ω is significant[16, 23], suppressing the signal from the bulk. At interfaces, phase shifts occur that can offset some of the Gouy phase mismatch, producing far-field THG radiation within the cone angle of the condenser lens. The interface sensitivity of THG is not clearly seen in the TSFG images, indicating that phase-matching conditions are more relaxed in TSFG.[39] Consequently, like CARS, TSFG can be used as a general imaging method that is not significantly affected by interface effects.

5.3.3 TSFG microscopy of biological tissue samples

For imaging of biological tissue samples it is important to reduce the effects of heating of the sample due to MIR absorption, as well as minimize the average power of the pump beam. In the following, we reduce the MIR power to 3 mW and the pump power to 30 mW, and study the feasibility to perform non-destructive imaging of tissue samples. In addition, to relax the imaging conditions, the samples were immersed in a D_2O-based phosphate buffer.

Figure 5.4(A) shows a TSFG image of a sectioned mouse eyelid skin containing the so-called Meibomian gland. Meibomian glands have previously been studied with CRS microscopy.[72, 110] The gland consists of acini that produce the lipid-rich meibum, which is compacted in ductules and collected in a central duct for release through the gland's orifice. The image shows a cross-section through several ductules, which contain a high concentration of compacted wax esters and cholesterol esters. Despite the reduced average powers of the incident beams, the TSFG image clearly identifies the lipid-rich regions in the tissue when the MIR frequency is set at 2820 cm^{-1}. When tuned off-resonance to 3005 cm^{-1}, the signal from the meibum-rich areas becomes very faint, emphasizing the vibrational contrast of the TSFG signal. Note that unlike in Fig. 5.3, the lipid-rich regions appear as positive signals relative to the surrounding matrix. This is due to the much weaker signal of D_2O compared to H_2O at 3005 cm^{-1}. The corresponding CARS images, taken with 1 mW of Stokes light

and shown in panels 5.4(C) and 5.4(D), mirror the observations seen in TSFG, confirming the lipid origin of the observed TSFG image features.

The TSFG signal from the tissue disappears when either the ω_i or ω_p beam is blocked, or when the pulse trains are temporally offset. We find that the TSFG signal is spectrally confined to the expected wavelength range (445–450 nm), and no significant emission is observed that is red-shifted from the expected TSFG wavelength. This implies that nonlinearly excited fluorescence does not significantly contribute to the observed signal under the current excitation conditions.

We observe that the signal magnitude, image resolution and contrast rapidly deteriorate as a function of depth of the image plane in the tissue. We obtain good quality images down to ~ 25 μm in the tissue, but the magnitude of the TSFG signal is insufficient for generating acceptable images deeper into the tissue under the excitation conditions used here. This signal deterioration can be attributed to several factors, including attenuation of the MIR excitation beam and the low quality of the focal volume deeper into the tissue due to scattering. Nonetheless, as shown here, TSFG microscopy produces acceptable images of thin tissue sections, which is a common target in MIR microspectroscopy applications.

5.4 Discussion

In this work, we have examined the TSFG signal of samples and materials of biological relevance. The TSFG technique is based on an optical nonlinearity that has not been used before for imaging biological samples. Although electronically resonant and nonresonant versions of the TSFG interaction have been used as contrast mechanisms in NLO microscopy[99, 98], a vibrationally sensitive variation of the technique constitutes a new approach to biological imaging. The MIR-based TSFG interaction is exclusively sensitive to IR-active vibrational

modes[39], and thus offers a direct NLO analogue of MIR absorption microspectroscopy.

An attractive feature of TSFG is that it can be integrated into a laser-scanning NLO microscope.[39] This implies that IR-vibrational signals can be acquired alongside Raman-vibrational signals through CRS on the same imaging platform. We have not used advanced preparation protocols to specifically enhance the TSFG signal. Samples are mounted on a standard microscope glass slide (thickness 1 mm) and covered with a borosilicate coverslip (thickness 0.17 mm). When illuminating the sample from the coverslip side, MIR attenuation is present but acceptable, and imaging can proceed in a practical manner. Since the TSFG signal is in the 450 nm range, it is not significantly attenuated by the thicker microscope glass slide.

The experiments show a clear spectral dependence of the TSFG signal. Similar to the vibrational signatures in CARS, the vibrational lineshapes in TSFG appear dispersive, indicating the involvement of a nonresonant background. The dispersive lineshape is a clear indication that the signal is coherent, i.e. it does not rely on MIR-induced population transfer to a vibrational state followed by an incoherent hyper-Raman anti-Stokes interaction. The latter mechanism would produce dissipative lineshapes, contrary to what is observed in the experiments discussed here.

The TSFG signal of water in the CH-stretching range of the spectrum shows a significant spectral dependence. This indicates the involvement of the resonant excitation of OH-stretching modes, which extend well into this range in the IR absorption spectrum. Nonetheless, the TSFG signal of pure water at 2820 cm^{-1} is less than the TSFG signal from bulk lipid, enabling the relatively straightforward visualization of lipid materials in aqueous media. Although the TSFG signal itself is not overwhelmed by a water signal, direct absorption of the MIR radiation by water, followed by heating, cannot be avoided. Therefore, similar to any MIR-type measurement, caution should be taken to limit sample heating through absorption by water. Besides heating, absorption also affects the penetration depth.

This is especially challenging in the CH-stretching range, the focus of the present work, but should be more relaxed in the fingerprint region where absorption by water is significantly less.

The spatial resolution in TSFG microscopy is determined predominantly by the two-photon interaction of the NIR pump beam, offering an imaging resolution in the 0.5 μm range. This resolution is virtually independent of the MIR wavelength, and is thus constant while scanning the vibrational energy in the imaging experiment. The TSFG process probes the MIR-induced vibrational coherence of the sample, and is not directly sensitive to the thermal population of vibrational states in the material. This implies that the resolution is also independent of light induced heating and the subsequent heat dissipation dynamics. In other words, the resolution should be the same in samples with either slow or fast heat dissipation properties.

The TSFG signals from tissue sections are reasonable and show clear vibrational contrast. The imaging properties of the TSFG modality are very comparable to those of CARS. Images could be acquired at low average powers of the incident beams, ensuring sample integrity during imaging. We found that the TSFG signal was acceptable up to tissue sections with a thickness of $\sim$ 25 μm. Thicker tissue samples gave rise to deteriorating TSFG signals, both in terms of signal strength and resolution. Adaptive optics approaches may help to improve the image quality at deeper depths, although the penetration depth is determined primarily by absorption rather than by scattering alone. Nonetheless, even without further improvements, TSFG already appears to work well with thin tissue slices, i.e. the type of samples that are of relevance to histopathology.

Among other factors, the image quality is also determined by the focusing properties of the microscope objective. Although the reflective objective enables achromatic focusing of NIR and MIR laser beams, the overall confinement and quality of the focal volume is substantially less compared to a refractive objective. The limited axial resolution of the

Cassegrain objective implies that smaller features in the image are lost due to substantial signal integration along the axial dimension. To achieve high quality depth-resolved images similar to images commonly obtained in CRS with refractive objectives, it will be necessary to develop dedicated refractive lens systems that can handle both NIR and MIR light.

The TSFG technique brings some of the advantages of NLO imaging into the realm of IR-based microscopy. It offers the convenience of laser-scanning microscopy, a higher resolution and simplification of signal detection. Effectively, it moves the complexity of the experiment from the detection side to the excitation side. The picosecond MIR OPO system used in this work is a reliable and robust source, producing tunable narrow band radiation for selective excitation of vibrational modes. Conceptually, this form of microspectroscopy is similar to discrete frequency IR (DFIR) microscopy carried out with QCL excitation in the fingerprint region.[56] However, compared to an array of QCL modules, the OPO light source has a much larger footprint and requires occasional realignment. Further improvements of the light source will help make TSFG more practical. For instance, the picosecond pulses in our current system are not fully compressed to their Fourier transform limited pulse duration. There is much room for shortening the pump pulse, improve and shorten the output pulses from the OPO, and increase the TSFG signal efficiency by at least one order of magnitude. These simple measures would increase the effective image acquisition time and make TSFG more practical and robust. The success of techniques like SFG and TSFG, which rely on the generation of tunable MIR light, are likely to drive further developments of the light source, including reducing its footprint and cost.

Although the work here focuses on vibrational imaging in the CH-stretching range (∼2800–3000 cm^{-1}), the real benefits of TSFG are likely found in the fingerprint region (∼800–1800 cm^{-1}). The vibrational response of IR-active CH-stretching modes is weak compared to some of the most prominent fingerprint modes. Indeed, whereas in Raman spectroscopy the strongest spectral lines are found in the CH-stretching range for biological materials, in

IR-based spectroscopy the strongest modes are located in the fingerprint region. Although the fingerprint vibrational range is outside the tuning range of our MIR OPO system, it is possible to perform an additional difference frequency generation (DFG) step to generate picosecond light of sufficient pulse energy in the 5–10 μm regime. With much higher vibrationally resonant $\chi^{(3)}$ values in the fingerprint region, combined with the $|\chi^{(3)}|^2$ dependence of TSFG, we may expect signals that are up to two orders of magnitude stronger than in the CH-stretching range. The strong fingerprint TSFG signals are likely to outperform CARS in this range, where CARS signals are weak and often overwhelmed by background contributions. Therefore, the fact that TSFG microscopy already produces acceptable images in the challenging CH-stretching range is an encouraging prelude to TSFG imaging in the fingerprint region.

5.5 Conclusion

TSFG microscopy is a new technique that enables the generation of images with contrast based on the IR-activity of molecular vibrations. The TSFG process relies on a third-order light-matter interaction and is sensitive to the $\chi^{(3)}$ properties of the sample. This nonlinear version of the IR microscope offers a high lateral resolution of 0.5 μm and an axial resolution of about 10 μm in its current implementation, thus enabling intrinsic 3D imaging with vibrational sensitivity. The technique can be incorporated into a laser-scanning microscope that uses common visible photodetectors, offering straightforward visualization of biological samples in a manner similar to coherent Raman scattering microscopy. With anticipated improvements of the TSFG approach, fast 3D IR imaging is within reach, and high-resolution mapping of tissues in the fingerprint region is a realistic possibility.

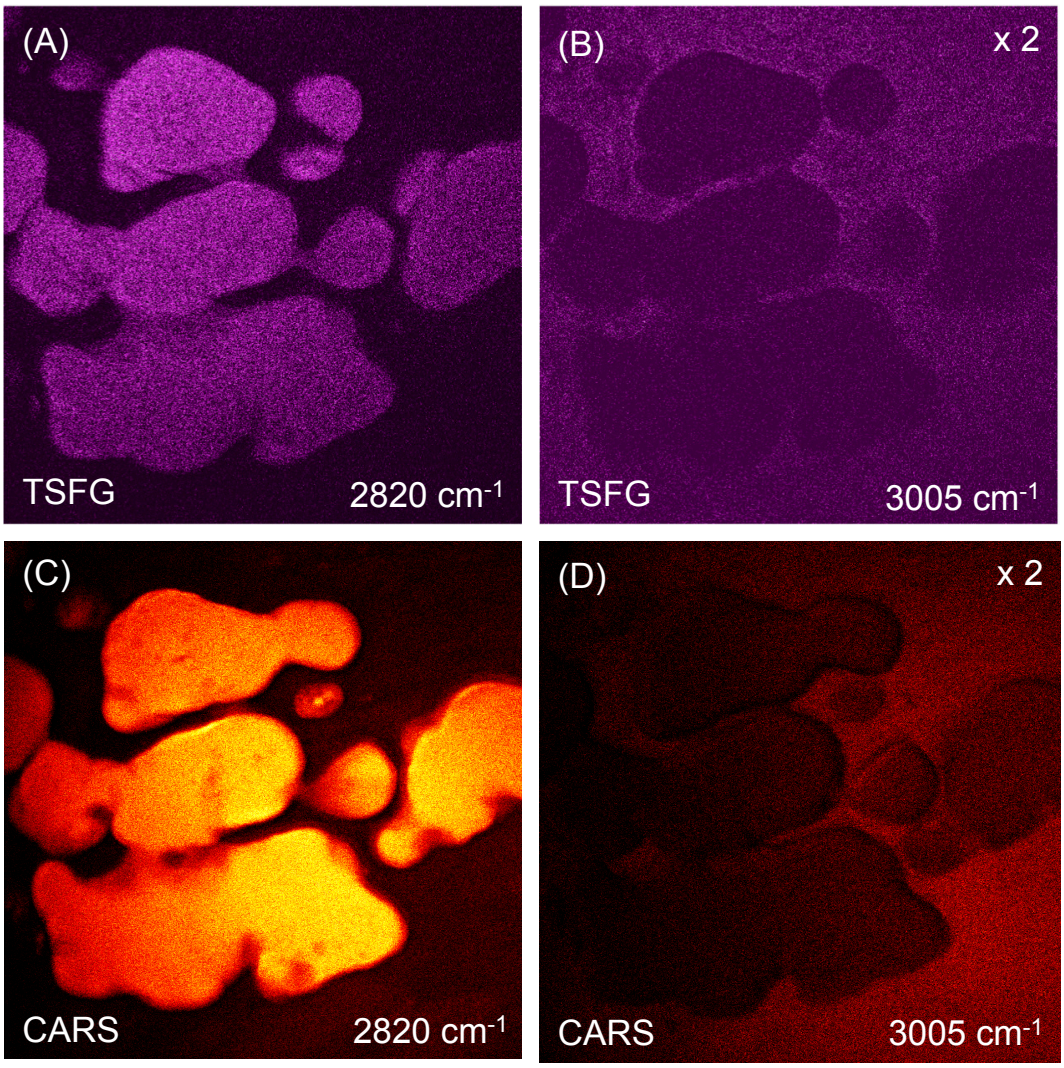

Figure 5.3: TSFG imaging of mouse tissue fat droplets in aqueous medium. (A) TSFG at 2820 cm^{-1}. (B) TSFG at 3005 cm^{-1}. Signal is multiplied by 2 relative to the signal shown in (A). (C) CARS at 2820 cm^{-1}. (D) CARS at 3005 cm^{-1}. Signal is multiplied by 2 relative to the signal shown in (C). Image frames are 50×50 μm^2.

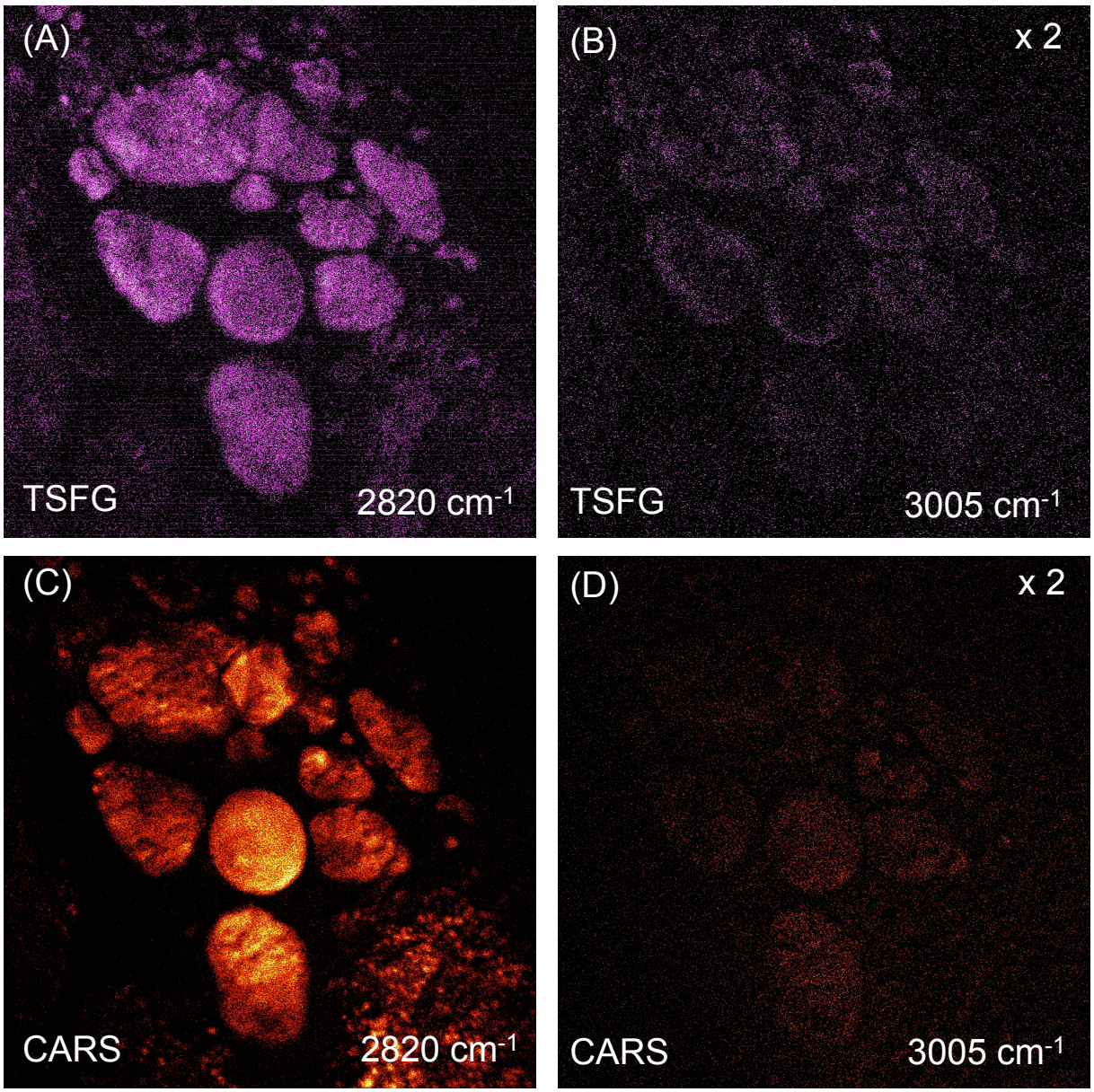

Figure 5.4: TSFG imaging of mouse Meibomian gland. (A) TSFG at 2820 cm^{-1}. (B) TSFG at 3005 cm^{-1}. (C) CARS at 2820 cm^{-1}. (D) CARS at 3005 cm^{-1}. Image frames are 60×60 μm^2.

Chapter 6

Future directions

6.1 Introduction

In this work I have described advancements in label-free nonlinear optical microscopy by using mid-infrared light to probe molecular vibrations for chemical contrast. Chapter 3 described a structurally sensitive imaging technique, SFG, which has been sped up by a factor of 60 using a beam-scanning geometry, making it comparable in speed to CRS. Chapter 4 described the discovery of a new imaging technique, TSFG, which is a lot like THG but with a tunable MIR laser which benefits from a vibrational enhancement on resonance. We found that TSFG is great for imaging small lipid droplets, and in chapter 5 we applied this technique to biological samples, specifically lipid rich cells from a mouse ear. Along the way there have been a number of observations in lab with varying degrees of interest that warrant further investigation.

6.2 Advancements in SFG

Sum frequency generation has excellent sensitivity to crystalline domains, and as a second-order optical effect has been used to determine crystallinity at concentrations lower than those possible by polarization resolved or x-ray diffraction. Paired with fast acquisition speeds, SFG shows great promise in quality control of pharmaceuticals where crystallinity can substantially impact the bioavailability in final dosage forms. This concept was explored in Chapter 3 with the investigation into cholesterol crystal structures which had strong signals benefiting from the methylene resonance. In the same study from Chapter 3 we imaged biological tissue containing type I collagen and reported a polarization dependent spectral response. Applied to the plethora of biologically relevant tissues with type I collagen, SFG shows great promise for imaging many systems with sub-micron resolution. Some interesting avenues to explore could include the cornea and dermis. Additionally, our body contains numerous crystalline structures that it makes on its own accord. Studying these micro-domain structures with SFG is a robust way to elucidate information from them, and has applications in atherosclerotic plaques, biomineralization in the pineal gland, and even spider silk. Though there is more commercial interest in collagen compared to cellulose studies, plant matter high in cellulose can be investigated at the cellular scale. This will be of importance during the renewable resource movement as disposable items are transmogrified from a polymer-plastics composition back to biodegradable, cellulose based materials. Additionally, as we approach the nascent stages of precision agriculture for vertical farming, select produce yielding plants will be extensively studied and engineered. SFG and NLO microscopy will be a valuable high resolution tool to examine these plants at the cellular level to ensure optimal organelle functionality and therefore plant growth.

An important feature of SFG is that it is sensitive to domains that lack inversion symmetry. As shown in figure 1.1, SFG is typically implemented in a non-collinear geometry and used to generate the nonlinear signal at surface interfaces for spectroscopic purposes. Integrating a

surface enhanced version of this technique with integrated photonic devices may prove useful. Pulling from manufacturing techniques optimized for CMOS devices, silicon waveguides are commonly paired with Er^+ laser sources used for telecom, around 1550nm. Crystalline silicon is transparent out to 8μm and would transmit light over the majority of the fingerprint range, however, light sources and detectors in this range are still hampered. Nonlinear upconversion would alleviate the issues with the detector as the light could be converted to the visible/NIR and detected with silicon photodiodes. SFG used on a "lab-on-chip" device for trace gas detection, or integrated with fluidic micro-channels, commonly referred to as optofluidics, has not been implemented yet, however, it would not only have excellent specificity by probing molecular IR absorptions of adsorbed analytes, but also benefit from simplified detection.

6.3 Advancements in TSFG

The future of TSFG as a nonlinear modality for biological applications is also very bright. As discussed in Chapter 4, the signal generation mechanism of TSFG is fundamentally different from SFG, and therefore will find applications in complimentary biological systems. The chemical contrast functionality produces images comparable to CARS. In order to generate larger signals it would be advantageous to have a more tightly (axially) confined focal volume by using an objective lens without a center obscuration. However, this may reduce overall signal or limit it to interfaces, much like THG due to phase matching conditions. Numerical simulations will need to be performed to further understand the signal generation process.

To date it is not clear under what conditions TSFG will be preferential to CARS microscopy. While CARS leverages the Raman scattering mechanism, and TSFG probes IR absorption, macro- and microscpoic biological domains have sufficient molecular diversity that both processes are expressed in abundance. The difference may become more apparent as the MIR beam is tuned deeper into the IR, away from the O-H and C-H vibrations, to probe

amides and other vibrational resonances with a weaker Raman response. Special care to the optical components will again be required to accommodate spectral contributions covering a decade in frequencies (1-10μm.) Nonetheless, CARS is preferred for thick samples with regards to both signal generation and collection. The MIR beam is attenuated by water absorption in the biological sample as it approaches focus, and, once the signal is generated, the two-photon hyper-Raman upconversion pushes the photon energy into the blue/UV, a significant difference from the red/NIR signals in CARS since Rayleigh scattering scales as λ^4. Thin samples such as microtomed tissues are preferred for TSFG. In Chapter 4 we demonstrated a TSFG enhancement on the C-H resonance. This could be leveraged in lipid rich applications such as meibomian glands and myelin sheath, similar to samples sensitive to CARS microscopy. However, tuning further into the fingerprint may reveal applications beyond lipid rich bio systems. Another avenue of exploration for the MIR may be as a label-free solution to ground state depletion for super resolution CRS imaging. This would require MIR vortex wave-plates or axicons for Bessel beam formation, paired with a high NA objective lens designed for broadband applications, such as a non-concentric reflective design. Finally, nonlinear imaging with label-free contrast will reach full realization once compact, affordable, and widely tunable sources are available. Ultrafast sources are seeing continuous improvements in compactness and affordability, though still limited in tunability and device implementations in medical imaging. I foresee the development of a commercial devices using a single colored femto source for hand-held biological imaging in the near future, as soon as 2020. However, despite the late interest in high efficiency MIR sources from the telecom industry, in order to increase energy density while avoiding TPA in silicon, these sources are far behind those in the NIR. Therefore, it will be likely 3 decades before SFG and TSFG will be incorporated into a hand-held device– a similar time-frame between the development of TPA microscopy and the work of this dissertation. Afterward, they will remain an integral part to bio-imaging, pharmaceuticals, micro manufacturing quality control, and other industries seeking non-destructive imaging with sub-micron resolution.

In conclusion, the field of vibrationally sensitive nonlinear optical microscopy with infrared light has emerged as a viable label-free approach to diffraction limited imaging with chemical contrast. Though limited to samples with noncentrosymmetric geometries, SFG has shown to be a bright signal generating modality with signal intensities comparable to CARS in samples rich in type I collagen. TSFG signals can originate from amorphous samples, however, image brightness in our implementation is almost an order of magnitude weaker than CARS. There is much to do to optimize these imaging modalities, particularly in the way of the excitation optics. For this reason, SFG and TSFG are not trivial to adapt as part of a multimodal NLO microscope. Their inclusion will likely be justified as high resolution techniques used in conjunction with vector component analysis and machine learning algorithms to train lower spatial and spectral resolution (multispectral as opposed to hyperspectral) techniques. SFG and TSFG are extraordinary additions to the family of NLO microscopy modalities, and will continue to gain recognition for their utility as label free techniques with sub-micron resolution.

Bibliography

[1] H. S. AlSalem, C. Holroyd, M. Danial Iswan, A. B. Horn, M. A. Denecke, and S. P. K. Koehler. Characterisation, coverage, and orientation of functionalised graphene using sum-frequency generation spectroscopy. *Physical Chemistry Chemical Physics*, 20(13):8962–8967, 3 2018.

[2] B. Amirsolaimani, B. Cromey, N. Peyghambarian, and K. Kieu. All-reflective multiphoton microscope. *Optics Express*, 25(19):23399, 9 2017.

[3] S. Augst, D. Strickland, D. D. Meyerhofer, S. L. Chin, and J. H. Eberly. Tunneling ionization of noble gases in a high-intensity laser field. *Physical Review Letters*, 63(20):2212–2215, 11 1989.

[4] Y. Barad, H. Eisenberg, M. Horowitz, and Y. Silberberg. Nonlinear scanning laser microscopy by third harmonic generation. *Applied Physics Letters*, 70(8):922, 8 1998.

[5] W. P. Beeker, C. J. Lee, K. J. Boller, P. Groß, C. Cleff, C. Fallnich, H. L. Offerhaus, J. L. Herek, H. L. Offerhaus, and J. L. Herek. A theoretical investigation of superresolution CARS imaging via coherent and incoherent saturation of transitions. *Journal of Raman Spectroscopy*, 42(10):1854–1858, 10 2011.

[6] S. Bégin, B. Burgoyne, V. Mercier, A. Villeneuve, R. Vallée, and D. Côté. Coherent anti-Stokes Raman scattering hyperspectral tissue imaging with a wavelength-swept system. *Biomedical optics express*, 2(5):1296–306, 4 2011.

[7] R. Bhargava. Infrared Spectroscopic Imaging: The Next Generation. *Applied Spectroscopy*, 66(10):1091–1120, 10 2012.

[8] N. Bloembergen. *Nonlinear Optics*. WORLD SCIENTIFIC, 1 1996.

[9] M. Bonn, C. Hess, J. H. Miners, T. F. Heinz, H. J. Bakker, and M. Cho. Novel Surface Vibrational Spectroscopy: Infrared-Infrared-Visible Sum-Frequency Generation. *Physical Review Letters*, 86(8):1566–1569, 2 2001.

[10] R. W. Boyd. Infrared Upconversion for Astronomy. Technical report.

[11] R. M. Brown, Jr., A. C. Millard, and P. J. Campagnola. Macromolecular structure of cellulose studied by second-harmonic generation imaging microscopy. *Optics Letters*, 28(22):2207, 11 2003.

[12] R. C. Burruss, A. D. Slepkov, A. F. Pegoraro, and A. Stolow. Unraveling the complexity of deep gas accumulations with three-dimensional multimodal CARS microscopy. *Geology*, 40(12):1063–1066, 12 2012.

[13] C. H. Camp Jr and M. T. Cicerone. Chemically sensitive bioimaging with coherent Raman scattering. *Nature Photonics*, 9(5):295–305, 5 2015.

[14] P. Campagnola. Second harmonic generation imaging microscopy: applications to diseases diagnostics. *Analytical chemistry*, 83(9):3224–31, 5 2011.

[15] J.-X. Cheng, S. Pautot, D. A. Weitz, and X. S. Xie. Ordering of water molecules between phospholipid bilayers visualized by coherent anti-Stokes Raman scattering microscopy. *Proceedings of the National Academy of Sciences of the United States of America*, 100(17):9826–30, 8 2003.

[16] J.-X. Cheng, A. Volkmer, and X. S. Xie. Theoretical and experimental characterization of coherent anti-Stokes Raman scattering microscopy. *Journal of the Optical Society of America B*, 19(6):1363, 6 2002.

[17] J.-X. Cheng and X. S. Xie. *Coherent Raman Scattering Microscopy*. CRC Press, 2016.

[18] C.-Y. Chung and E. O. Potma. Biomolecular Imaging with Coherent Nonlinear Vibrational Microscopy. *Annual Review of Physical Chemistry*, 64(1):77–99, 4 2013.

[19] K. A. Cimatu and S. Baldelli. Chemical Microscopy of Surfaces by Sum Frequency Generation Imaging. *The Journal of Physical Chemistry C*, 113(38):16575–16588, 9 2009.

[20] C. Cleff, P. Groß, C. Fallnich, H. L. Offerhaus, J. L. Herek, K. Kruse, W. P. Beeker, C. J. Lee, and K.-J. Boller. Ground-state depletion for subdiffraction-limited spatial resolution in coherent anti-Stokes Raman scattering microscopy. *Physical Review A*, 86(2):023825, 8 2012.

[21] C.-A. Couture, S. Bancelin, J. VanderKolk, K. Popov, M. Rivard, K. Légaré, G. Martel, H. Richard, C. Brown, S. Laverty, L. Ramunno, and F. Légaré. The Impact of Collagen Fibril Polarity on Second Harmonic Generation Microscopy. *Biophysical Journal*, 109(12):2501–2510, 12 2015.

[22] J. S. Dam, P. Tidemand-Lichtenberg, and C. Pedersen. Room-temperature mid-infrared single-photon spectral imaging. *Nature Photonics*, 6(11):788–793, 9 2012.

[23] D. Débarre, W. Supatto, and E. Beaurepaire. Structure sensitivity in third-harmonic generation microscopy. *Optics Letters*, 30(16):2134, 8 2005.

[24] D. Débarre, W. Supatto, A.-M. Pena, A. Fabre, T. Tordjmann, L. Combettes, M.-C. Schanne-Klein, and E. Beaurepaire. Imaging lipid bodies in cells and tissues using third-harmonic generation microscopy. *Nature Methods*, 3(1):47–53, 1 2006.

[25] V. Denisov, B. Mavrin, and V. Podobedov. Hyper-Raman scattering by vibrational excitations in crystals, glasses and liquids. *Physics Reports*, 151(1):1–92, 7 1987.

[26] W. Denk, J. H. Strickler, . Watt, and W. Webb. Two-Photon Laser Scanning Fluorescence Microscopy. Technical Report 4951, 1990.

[27] J. Doherty, G. Cinque, and P. Gardner. Single-cell analysis using Fourier transform infrared microspectroscopy. *Applied Spectroscopy Reviews*, 52(6):560–587, 7 2017.

[28] X. Dow, E. DeWalt, J. Newman, C. Dettmar, and G. Simpson. Unified Theory for Polarization Analysis in Second Harmonic and Sum Frequency Microscopy. *Biophysical Journal*, 111(7):1553–1568, 10 2016.

[29] G. L. Eesley. *Coherent Raman spectroscopy*.

[30] K. B. Eisenthal. Liquid Interfaces Probed by Second-Harmonic and Sum-Frequency Spectroscopy. 1996.

[31] C. L. Evans, E. O. Potma, M. Puoris'haag, D. Côté, C. P. Lin, and X. S. Xie. Chemical imaging of tissue in vivo with video-rate coherent anti-Stokes Raman scattering microscopy. *Proceedings of the National Academy of Sciences of the United States of America*, 102(46):16807–12, 11 2005.

[32] P. A. Franken, A. E. Hill, C. W. Peters, and G. Weinreich. Generation of Optical Harmonics. *Physical Review Letters*, 7(4):118–119, 8 1961.

[33] L. Fu, S.-L. Chen, and H.-F. Wang. Validation of Spectra and Phase in Sub-1 cm ¡sup¿1¡/sup¿ Resolution Sum-Frequency Generation Vibrational Spectroscopy through Internal Heterodyne Phase-Resolved Measurement. *The Journal of Physical Chemistry B*, 120(8):1579–1589, 3 2016.

[34] F. Ganikhanov, S. Carrasco, X. Sunney Xie, M. Katz, W. Seitz, and D. Kopf. Broadly tunable dual-wavelength light source for coherent anti-Stokes Raman scattering microscopy. *Optics Letters*, 31(9):1292, 5 2006.

[35] E. T. Garbacik, J. L. Herek, C. Otto, and H. L. Offerhaus. Rapid identification of heterogeneous mixture components with hyperspectral coherent anti-Stokes Raman scattering imaging. *Journal of Raman Spectroscopy*, 43(5):651–655, 5 2012.

[36] E. T. Garbacik, J. P. Korterik, C. Otto, S. Mukamel, J. L. Herek, and H. L. Offerhaus. Background-Free Nonlinear Microspectroscopy with Vibrational Molecular Interferometry. *Physical Review Letters*, 107(25):253902, 12 2011.

[37] Y. Han, J. Hsu, N.-H. Ge, and E. O. Potma. Polarization-Sensitive Sum-Frequency Generation Microscopy of Collagen Fibers. *The Journal of Physical Chemistry B*, 119(8):3356–3365, 2 2015.

[38] Y. Han, V. Raghunathan, R.-r. Feng, H. Maekawa, C.-Y. Chung, Y. Feng, E. O. Potma, and N.-H. Ge. Mapping Molecular Orientation with Phase Sensitive Vibrationally Resonant Sum-Frequency Generation Microscopy. *The Journal of Physical Chemistry B*, 117(20):6149–6156, 5 2013.

[39] A. Hanninen, R. Prince, and E. Potma. Triple modal coherent nonlinear imaging with vibrational contrast. *IEEE Journal of Selected Topics in Quantum Electronics*, 25(1), 2019.

[40] A. Hanninen, M. Wai Shu, and E. O. Potma. Hyperspectral imaging with laser-scanning sum-frequency generation microscopy. *Second Harmonic Generation Imaging Coherent Raman Scattering Microscopy Y. R. Shen BIOMEDICAL OPTICS EXPRESS*, 8(4230), 2017.

[41] L. M. Haupert and G. J. Simpson. Screening of protein crystallization trials by second order nonlinear optical imaging of chiral crystals (SONICC). *Methods*, 55(4):379–386, 12 2011.

[42] M. Hermes, R. B. Morrish, L. Huot, L. Meng, S. Junaid, J. Tomko, G. R. Lloyd, W. T. Masselink, P. Tidemand-Lichtenberg, C. Pedersen, F. Palombo, and N. Stone. Mid-IR hyperspectral imaging for label-free histopathology and cytology. *Journal of Optics*, 20(2):023002, 2 2018.

[43] C. Hirose, N. Akamatsu, and K. Domen. Formulas for the analysis of surface sum-frequency generation spectrum by CH stretching modes of methyl and methylene groups Communication: Spectroscopic phase and lineshapes in high-resolution broadband sum frequency vibrational spectroscopy: Resolving interfacial inhomogeneities of "identical" molecular groups Formulas for the analysis of surface sum-frequency generation spectrum by CH stretching modes of methyl and methylene groups. *Journal of Vacuum Science & Technology A: Vacuum, Surfaces, and Films*, 96:241102, 1992.

[44] C. Hirose, H. Yamamoto, N. Akamatsu, and K. Domen. Orientation analysis by simulation of vibrational sum frequency generation spectrum: CH stretching bands of the methyl group. *The Journal of Physical Chemistry*, 97(39):10064–10069, 9 1993.

[45] C. J. Hirschmugl and K. M. Gough. Fourier Transform Infrared Spectrochemical Imaging: Review of Design and Applications with a Focal Plane Array and Multiple Beam Synchrotron Radiation Source. *Applied Spectroscopy*, 66(5):475–491, 5 2012.

[46] D. M. P. Hoffmann, K. Kuhnke, and K. Kern. Sum-frequency generation microscope for opaque and reflecting samples. 2002.

[47] E. E. Hoover and J. A. Squier. Advances in multiphoton microscopy technology. *Nature Photonics*, 7(2):93–101, 2 2013.

[48] S. Huang, M. Makarem, S. N. Kiemle, H. Hamedi, M. Sau, D. J. Cosgrove, and S. H. Kim. Inhomogeneity of Cellulose Microfibril Assembly in Plant Cell Walls Revealed

with Sum Frequency Generation Microscopy. *The Journal of Physical Chemistry B*, 122(19):5006–5019, 5 2018.

[49] K. Inoue, M. Sakai, and M. Fujii. Development of a Non-scanning Vibrational Sum-Frequency Generation Detected Infrared Super-Resolution Microscope and Its Application to Biological Cells. *Applied Spectroscopy, Vol. 64, Issue 3, pp. 275-281*, 64(3):275–281, 3 2010.

[50] Ji-xin Cheng, Andreas Volkmer, L. D. Book, , and X. S. Xie*. An Epi-Detected Coherent Anti-Stokes Raman Scattering (E-CARS) Microscope with High Spectral Resolution and High Sensitivity. 2001.

[51] T. A. Johnson and S. A. Diddams. Mid-infrared upconversion spectroscopy based on a Yb:fiber femtosecond laser. *Applied Physics B*, 107(1):31–39, 4 2012.

[52] L. M. Kehlet, P. Tidemand-Lichtenberg, J. S. Dam, and C. Pedersen. Infrared upconversion hyperspectral imaging. *Optics Letters*, 40(6):938, 3 2015.

[53] P. J. N. Kett, M. T. L. Casford, and P. B. Davies. Sum Frequency Generation (SFG) Vibrational Spectroscopy of Planar Phosphatidylethanolamine Hybrid Bilayer Membranes under Water. *Langmuir*, 26(12):9710–9719, 6 2010.

[54] S. Kogure, K. Inoue, T. Ohmori, M. Ishihara, M. Kikuchi, M. Fujii, and M. Sakai. Infrared imaging of an A549 cultured cell by a vibrational sum-frequency generation detected infrared super-resolution microscope. *Optics Express*, 18(13):13402, 6 2010.

[55] M. R. Kole, R. K. Reddy, M. V. Schulmerich, M. K. Gelber, and R. Bhargava. Discrete frequency infrared microspectroscopy and imaging with a tunable quantum cascade laser. *Analytical Chemistry*, 2012.

[56] M. R. Kole, R. K. Reddy, M. V. Schulmerich, M. K. Gelber, and R. Bhargava. Discrete frequency infrared microspectroscopy and imaging with a tunable quantum cascade laser. *Analytical Chemistry*, 2012.

[57] K. Kuhnke, . D. M. P. Hoffmann, X. C. Wu, A. M. Bittner, and K. Kern. Chemical imaging of interfaces by sum-frequency generation microscopy: Application to patterned self-assembled monolayers. *APPLIED PHYSICS LETTERS*, 83, 2003.

[58] M. Kumbham, S. Daly, K. ODwyer, R. Mouras, N. Liu, A. Mani, A. Peremans, S. M. Tofail, and C. Silien. Doubling the far-field resolution in mid-infrared microscopy. *Optics Express*, 24(21):24377, 10 2016.

[59] T. T. Le, S. Yue, and J.-X. Cheng. Shedding new light on lipid biology with coherent anti-Stokes Raman scattering microscopy. *Journal of Lipid Research*, 51(11):3091–3102, 11 2010.

[60] C. M. Lee, K. Kafle, S. Huang, and S. H. Kim. Multimodal Broadband Vibrational Sum Frequency Generation (MM-BB-V-SFG) Spectrometer and Microscope. *The Journal of Physical Chemistry B*, 120(1):102–116, 1 2016.

[61] C. M. Lee, K. Kafle, Y. B. Park, and S. H. Kim. Probing crystal structure and mesoscale assembly of cellulose microfibrils in plant cell walls, tunicate tests, and bacterial films using vibrational Sum Frequency Generation (SFG) spectroscopy. *Physical Chemistry Chemical Physics*, 16(22):10844, 6 2014.

[62] C. M. Lee, J. D. Kubicki, B. Fan, L. Zhong, M. C. Jarvis, and S. H. Kim. Hydrogen-Bonding Network and OH Stretch Vibration of Cellulose: Comparison of Computational Modeling with Polarized IR and SFG Spectra. *The Journal of Physical Chemistry B*, 119(49):15138–15149, 12 2015.

[63] C. M. Lee, A. Mittal, A. L. Barnette, K. Kafle, Y. B. Park, H. Shin, D. K. Johnson, S. Park, and S. H. Kim. Cellulose polymorphism study with sum-frequency-generation (SFG) vibration spectroscopy: identification of exocyclic CH2OH conformation and chain orientation. *Cellulose*, 20(3):991–1000, 6 2013.

[64] C. M. Lee, N. M. A. Mohamed, H. D. Watts, J. D. Kubicki, and S. H. Kim. Sum-Frequency-Generation Vibration Spectroscopy and Density Functional Theory Calculations with Dispersion Corrections (DFT-D2) for Cellulose Iα and Iβ. *The Journal of Physical Chemistry B*, 117(22):6681–6692, 6 2013.

[65] E. S. Lee and J. Y. Lee. High resolution cellular imaging with nonlinear optical infrared microscopy. *Optics express*, 19(2):1378–84, 1 2011.

[66] E. S. Lee, S.-W. Lee, J. Hsu, and E. O. Potma. Vibrationally resonant sum-frequency generation microscopy with a solid immersion lens. *Biomedical Optics Express*, 5(7):2125, 7 2014.

[67] H. J. Lee and J.-X. Cheng. Imaging chemistry inside living cells by stimulated Raman scattering microscopy. *Methods*, 128:119–128, 9 2017.

[68] Y. J. Lee, D. Moon, K. B. Migler, and M. T. Cicerone. Quantitative Image Analysis of Broadband CARS Hyperspectral Images of Polymer Blends. *Analytical Chemistry*, 83(7):2733–2739, 4 2011.

[69] C. Li, D. Zhang, M. N. Slipchenko, and J.-X. Cheng. Mid-Infrared Photothermal Imaging of Active Pharmaceutical Ingredients at Submicrometer Spatial Resolution.

[70] C. Li, D. Zhang, M. N. Slipchenko, and J.-X. Cheng. Mid-Infrared Photothermal Imaging of Active Pharmaceutical Ingredients at Submicrometer Spatial Resolution. *Analytical Chemistry*, 89(9):4863–4867, 5 2017.

[71] H. Li, Y. Miyauchi, N. A. Tuan, G. Mizutani, and M. Koyano. Optical Sum Frequency Generation Image of Rice Grains. *Journal of Biomaterials and Nanobiotechnology*, 3:286–291, 2012.

[72] C.-Y. Lin, J. L. Suhalim, C. L. Nien, M. D. Miljkovic, M. Diem, J. V. Jester, and E. O. Potma. Picosecond spectral coherent anti-Stokes Raman scattering imaging with principal component analysis of meibomian glands. *Journal of Biomedical Optics*, 16(2):021104, 2 2011.

[73] K. Locharoenrat, H. Sano, and G. Mizutani. Demonstration of confocal sum frequency microscopy. *physica status solidi (c)*, 6(1):304–306, 1 2009.

[74] Y. Marubashi, T. Higashi, S. Hirakawa, S. Tani, T. Erata, M. Takai, and J. Kawamata. Second Harmonic Generation Measurements for Biomacromolecules: Celluloses. *Optical Review*, 11(6):385–387, 12 2004.

[75] B. R. Masters and P. T. C. So. *Handbook of biomedical nonlinear optical microscopy*. Oxford University Press, 2008.

[76] . Mathias Flörsheimer, C. Brillert, , and H. Fuchs. Chemical Imaging of Interfaces by Sum Frequency Microscopy. 1999.

[77] T. Meyer, D. Akimov, N. Tarcea, S. Chatzipapadopoulos, G. Muschiolik, J. Kobow, M. Schmitt, and J. Popp. Three-Dimensional Molecular Mapping of a Multiple Emulsion by Means of CARS Microscopy. *The Journal of Physical Chemistry B*, 112(5):1420–1426, 2 2008.

[78] M. Miljković, T. Chernenko, M. J. Romeo, B. Bird, C. Matthäus, and M. Diem. Label-free imaging of human cells: algorithms for image reconstruction of Raman hyperspectral datasets. *The Analyst*, 135(8):2002, 8 2010.

[79] L. M. Miller and P. Dumas. From structure to cellular mechanism with infrared microspectroscopy. *Current Opinion in Structural Biology*, 20(5):649–656, 10 2010.

[80] G. Mizutani, H. C. Hieu, H. Li, N. A. Tuan, and Y. Miyauchi. Sum Frequency Generation Microscopy Study of Cellulose Fibers. *Applied Spectroscopy, Vol. 65, Issue 11, pp. 1254-1259*, 65(11):1254–1259, 11 2011.

[81] L. Moreaux, O. Sandre, and J. Mertz. Membrane imaging by second-harmonic generation microscopy. *Journal of the Optical Society of America B*, 17(10):1685, 10 2000.

[82] S. S. Mukamel. *Principles of nonlinear optical spectroscopy*. Oxford University Press, 1995.

[83] N. Olivier, D. Débarre, P. Mahou, and E. Beaurepaire. Third-harmonic generation microscopy with Bessel beams: a numerical study. *Optics Express*, 20(22):24886, 10 2012.

[84] Y. Ozeki, W. Umemura, Y. Otsuka, S. Satoh, H. Hashimoto, K. Sumimura, N. Nishizawa, K. Fukui, and K. Itoh. High-speed molecular spectral imaging of tissue with stimulated Raman scattering. *Nature Photonics*, 6(12):845–851, 12 2012.

[85] F. S. Pavone and P. J. Campagnola. *Second harmonic generation imaging*. CRC Press, Taylor & Francis, 2013.

[86] A. Peciulyte, J. Kiskis, P. T. Larsson, L. Olsson, and A. Enejder. Visualization of structural changes in cellulosic substrates during enzymatic hydrolysis using multimodal nonlinear microscopy. *Cellulose*, 23(3):1521–1536, 6 2016.

[87] M. C. Phillips and N. Hô. Infrared hyperspectral imaging using a broadly tunable external cavity quantum cascade laser and microbolometer focal plane array. *Optics Express*, 16(3):1836, 2 2008.

[88] R. C. Prince, R. R. Frontiera, and E. O. Potma. Stimulated Raman Scattering: From Bulk to Nano. *Chemical reviews*, 117(7):5070–5094, 12 2016.

[89] S. Psilodimitrakopoulos, S. I. C. O. Santos, I. Amat-Roldan, A. K. N. Thayil, D. Artigas, and P. Loza-Alvarez. In vivo, pixel-resolution mapping of thick filaments' orientation in nonfibrilar muscle using polarization-sensitive second harmonic generation microscopy. *Journal of Biomedical Optics*, 14(1):014001, 2009.

[90] V. Raghunathan, Y. Han, O. Korth, N.-H. Ge, and E. O. Potma. Rapid vibrational imaging with sum frequency generation microscopy. *Optics Letters*, 36(19):3891, 10 2011.

[91] S. Rahav and S. Mukamel. Stimulated coherent anti-Stokes Raman spectroscopy (CARS) resonances originate from double-slit interference of two-photon Stokes pathways. *Proceedings of the National Academy of Sciences of the United States of America*, 107(11):4825–9, 3 2010.

[92] R. K. Reddy, M. J. Walsh, M. V. Schulmerich, P. S. Carney, and R. Bhargava. High-definition infrared spectroscopic imaging. *Applied spectroscopy*, 67(1):93–105, 1 2013.

[93] K. Reiser, P. Stoller, and A. Knoesen. Three-Dimensional Geometry of Collagenous Tissues by Second Harmonic Polarimetry. *Scientific Reports*, 7(1):2642, 12 2017.

[94] G. H. Rieke, G. S. Wright, T. Böker, J. Bouwman, L. Colina, A. Glasse, K. D. Gordon, T. P. Greene, M. Güdel, T. Henning, K. Justtanont, P.-O. Lagage, M. E. Meixner, H.-U. Nørgaard-Nielsen, T. P. Ray, M. E. Ressler, E. F. van Dishoeck, and C. Waelkens. The Mid-Infrared Instrument for the ¡i¿James Webb Space Telescope¡/i¿ , I: Introduction. *Publications of the Astronomical Society of the Pacific*, 127(953):584–594, 7 2015.

[95] I. Rocha-Mendoza, D. R. Yankelevich, M. Wang, K. M. Reiser, C. W. Frank, and A. Knoesen. Sum Frequency Vibrational Spectroscopy: The Molecular Origins of the Optical Second-Order Nonlinearity of Collagen. *Biophysical Journal*, 93(12):4433–4444, 12 2007.

[96] M. B. J. Roeffaers, X. Zhang, C. W. Freudiger, B. G. Saar, M. v. Ruijven, G. v. Dalen, C. Xiao, and X. S. Xie. Label-free imaging of biomolecules in food products using stimulated Raman microscopy. *Journal of Biomedical Optics*, 16(2):021118, 2011.

[97] B. G. Saar, C. W. Freudiger, J. Reichman, C. M. Stanley, G. R. Holtom, and X. S. Xie. Video-rate molecular imaging in vivo with stimulated Raman scattering. *Science (New York, N.Y.)*, 330(6009):1368–70, 12 2010.

[98] H. Segawa, N. Fukutake, P. Leproux, V. Couderc, T. Ozawa, and H. Kano. Electronically resonant third-order sum frequency generation spectroscopy using a nanosecond white-light supercontinuum. *Optics express*, 22(9):10416–29, 5 2014.

[99] H. Segawa, M. Okuno, H. Kano, P. Leproux, V. Couderc, and H.-O. Hamaguchi. Label-free tetra-modal molecular imaging of living cells with CARS, SHG, THG and TSFG (coherent anti-Stokes Raman scattering, second harmonic generation, third harmonic generation and third-order sum frequency generation). *Optics express*, 20(9):9551–7, 4 2012.

[100] Y. R. Shen. Surface properties probed by second-harmonic and sum-frequency generation. *Nature*, 337(6207):519–525, 2 1989.

[101] A. D. Slepkov, A. Ridsdale, A. F. Pegoraro, D. J. Moffatt, and A. Stolow. Multimodal CARS microscopy of structured carbohydrate biopolymers. *Biomedical optics express*, 1(5):1347–1357, 11 2010.

[102] M. N. Slipchenko, H. Chen, D. R. Ely, Y. Jung, M. T. Carvajal, and J.-X. Cheng. Vibrational imaging of tablets by epi-detected stimulated Raman scattering microscopy. *The Analyst*, 135(10):2613, 10 2010.

[103] K. A. Smith and J. C. Conboy. A Simplified Sum-Frequency Vibrational Imaging Setup Used for Imaging Lipid Bilayer Arrays. *Analytical Chemistry*, 84(19):8122–8126, 10 2012.

[104] J. Squier and M. Müller. High resolution nonlinear microscopy: A review of sources and methods for achieving optimal imaging. *Review of Scientific Instruments*, 72(7):2855–2867, 7 2001.

[105] J. A. Squier, M. Müller, G. J. Brakenhoff, and K. R. Wilson. Third harmonic generation microscopy. *Optics Express*, 3(9):315, 10 1998.

[106] C. J. Strachan, M. Windbergs, and H. L. Offerhaus. Pharmaceutical applications of non-linear imaging. *International Journal of Pharmaceutics*, 417(1-2):163–172, 9 2011.

[107] D. Strickland and G. Mourou. COMPRESSION OF AMPLIFIED CHIRPED OPTICAL PULSES *. Technical report, 1985.

[108] P.-J. Su, W.-L. Chen, Y.-F. Chen, and C.-Y. Dong. Determination of collagen nanostructure from second-order susceptibility tensor analysis. *Biophysical journal*, 100(8):2053–62, 4 2011.

[109] J. Suhalim, C.-Y. Chung, M. Lilledahl, R. Lim, M. Levi, B. Tromberg, and E. Potma. Characterization of Cholesterol Crystals in Atherosclerotic Plaques Using Stimulated Raman Scattering and Second-Harmonic Generation Microscopy. *Biophysical Journal*, 102(8):1988–1995, 4 2012.

[110] J. L. Suhalim, G. J. Parfitt, Y. Xie, C. S. De Paiva, C. S. De Pavia, S. C. Pflugfelder, T. N. Shah, E. O. Potma, D. J. Brown, and J. V. Jester. Effect of desiccating stress on mouse meibomian gland function. *The ocular surface*, 12(1):59–68, 1 2014.

[111] J. T. Tabarangao and A. D. Slepkov. Mimicking Multimodal Contrast with Vertex Component Analysis of Hyperspectral CARS Images. *Journal of Spectroscopy*, 2015:1–8, 2 2015.

[112] S. P. Tewari, H. Huang, and R. W. Boyd. Theory of third-harmonic generation using Bessel beams, and self-phase-matching. Technical report, 1996.

[113] A. J. Traverso, B. Hokr, Z. Yi, L. Yuan, S. Yamaguchi, M. O. Scully, and V. V. Yakovlev. Two-Photon Infrared Resonance Can Enhance Coherent Raman Scattering. *Physical Review Letters*, 120(6):063602, 2 2018.

[114] A. E. Tuer, S. Krouglov, N. Prent, R. Cisek, D. Sandkuijl, K. Yasufuku, B. C. Wilson, and V. Barzda. Nonlinear Optical Properties of Type I Collagen Fibers Studied by Polarization Dependent Second Harmonic Generation Microscopy. *The Journal of Physical Chemistry B*, 115(44):12759–12769, 11 2011.

[115] B. von Vacano, L. Meyer, and M. Motzkus. Rapid polymer blend imaging with quantitative broadband multiplex CARS microscopy. *Journal of Raman Spectroscopy*, 38(7):916–926, 7 2007.

[116] H.-F. Wang *, W. Gan , R. Lu §, Y. Rao ¶, and B.-H. Wu . Quantitative spectral and orientational analysis in surface sum frequency generation vibrational spectroscopy (SFG-VS). *International Reviews in Physical Chemistry*, 24(2):191–256, 4 2005.

[117] H. Wang, T. Gao, and W. Xiong. Self-Phase-Stabilized Heterodyne Vibrational Sum Frequency Generation Microscopy. *ACS Photonics*, 4(7):1839–1845, 7 2017.

[118] H.-F. Wang, L. Velarde, W. Gan, and L. Fu. Quantitative Sum-Frequency Generation Vibrational Spectroscopy of Molecular Surfaces and Interfaces: Lineshape, Polarization, and Orientation. *Annual Review of Physical Chemistry*, 66(1):189–216, 4 2015.

[119] H.-W. Wang, T. T. Le, and J.-X. Cheng. Label-free Imaging of Arterial Cells and Extracellular Matrix Using a Multimodal CARS Microscope. *Optics communications*, 281(7):1813–1822, 4 2008.

[120] D. L. Wetzel and S. M. LeVine. Imaging molecular chemistry with infrared microscopy. *Science (New York, N.Y.)*, 285(5431):1224–5, 8 1999.

[121] P. A. Wilks. The Evolution of Commercial IR Spectrometers and the People Who Made It Happen. Technical report.

[122] T. Wilson and C. Sheppard. Theory and practice of scanning optical microscopy. *London: Academic Press, —c1984*, 1984.

[123] M. Windbergs, M. Jurna, H. L. Offerhaus, J. L. Herek, P. Kleinebudde, and C. J. Strachan. Chemical Imaging of Oral Solid Dosage Forms and Changes upon Dissolution Using Coherent Anti-Stokes Raman Scattering Microscopy. *Analytical Chemistry*, 81(6):2085–2091, 3 2009.

[124] T. P. Wrobel and R. Bhargava. Infrared Spectroscopic Imaging Advances as an Analytical Technology for Biomedical Sciences. *Analytical Chemistry*, 90(3):1444–1463, 2 2018.

[125] D. Yelin and Y. Silberberg. Laser scanning third-harmonic-generation microscopy in biology. *Optics Express*, 5(8):169, 10 1999.

[126] D. Zhang, C. Li, C. Zhang, M. N. Slipchenko, G. Eakins, and J.-X. Cheng. Depth-resolved mid-infrared photothermal imaging of living cells and organisms with submicrometer spatial resolution. *Science Advances*, 2(9):e1600521–e1600521, 9 2016.

[127] D. Zhang, P. Wang, M. N. Slipchenko, D. Ben-Amotz, A. M. Weiner, and J.-X. Cheng. Quantitative Vibrational Imaging by Hyperspectral Stimulated Raman Scattering Microscopy and Multivariate Curve Resolution Analysis. *Analytical Chemistry*, 85(1):98–106, 1 2013.

[128] L. Zhang, Z. Lu, L. Velarde, L. Fu, Y. Pu, S.-Y. Ding, A. J. Ragauskas, H.-F. Wang, and B. Yang. Vibrational spectral signatures of crystalline cellulose using high resolution broadband sum frequency generation vibrational spectroscopy (HR-BB-SFG-VS). *Cellulose*, 22(3):1469–1484, 6 2015.

[129] D. Zheng, L. Lu, Y. Li, K. F. Kelly, and S. Baldelli. Compressive Broad-Band Hyperspectral Sum Frequency Generation Microscopy to Study Functionalized Surfaces. *The Journal of Physical Chemistry Letters*, 7(10):1781–1787, 5 2016.

[130] L. D. Ziegler. Hyper-Raman spectroscopy. *Journal of Raman Spectroscopy*, 21(12):769–779, 12 1990.

[131] M. Zimmerley, R. Younger, T. Valenton, D. C. Oertel, J. L. Ward, and E. O. Potma. Molecular orientation in dry and hydrated cellulose fibers: a coherent anti-Stokes Raman scattering microscopy study. *The journal of physical chemistry. B*, 114(31):10200–8, 8 2010.